

DESIGN AND CHARACTERIZATION OF A SMART BIT FOR IN-SITU FORCE MEASUREMENT,  
USING CAPACITIVE LOAD CELLS AND ACOUSTIC SPECTRA ANALYSIS TO DETERMINE  
ROCK TYPE AND TOOL WEAR IN ROCK EXCAVATION PROCESS

by

Austin F. Oltmanns

**© Copyright by Austin F. Oltmanns, 2024**

All Rights Reserved

A thesis submitted to the Faculty and the Board of Trustees of the Colorado School of Mines in partial fulfillment of the requirements for the degree of Doctor of Philosophy (Robotics).

Golden, Colorado

Date \_\_\_\_\_

Signed: \_\_\_\_\_

Austin F. Oltmanns

Signed: \_\_\_\_\_

Dr. Andrew J. Petruska  
Thesis Advisor

Golden, Colorado

Date \_\_\_\_\_

Signed: \_\_\_\_\_

Dr. Carl Frick  
Department Head  
Department of Mechanical Engineering

## ABSTRACT

Underground miners continue to be exposed to hazards on a routine basis. The best way to mitigate this is removing the operator from the hazardous locations while increasing overall productivity. This work investigates methods for determining tool wear and material type with a sensing system, which would enable operators to make decisions using objective feedback from a safer location. Machine operators must determine tool wear and material type during operation, and when they get close to the cutting interface, they place themselves at risk. Vibration frequencies, acoustic emissions, and cutting forces are all shown to vary with the tested cutting conditions. Three different sensor designs were tested and used: a capacitive load cell with non-linear dynamics used to classify material type and tool wear conditions, an acoustic sensor used to classify tool wear, and a capacitive load cell with linear dynamics used to measure the cutting forces. The capacitive load cell with linear dynamics, when used with a small neural network regression and a 2nd order polynomial expansion, is able to measure rock cutting forces with a mean absolute error less than 4 kilonewtons and an  $R^2$  score greater than 0.8 under tested conditions.

Performing material and tool wear classification is done with machine learning classification methods. The Support-Vector machine using fast Fourier spectra magnitude of short samples of signal, around 0.2 seconds, performed the best. Full scale rock cutting tests are performed using a linear cutting machine at the Earth Mechanics Institute at the Colorado School of Mines campus. Analytical models for the capacitive sensors are developed as part of this research, and they can be used to guide future designs. This work discusses the sensitivity to input force of the designed sensors. These models also guide the choice of classification methods used to determine material type and tool wear, which are shown to perform well for the experimental conditions.

## TABLE OF CONTENTS

ABSTRACT . . . . .	iii
LIST OF FIGURES . . . . .	viii
LIST OF TABLES . . . . .	xiii
LIST OF ABBREVIATIONS . . . . .	xiv
ACKNOWLEDGMENTS . . . . .	xvi
DEDICATION . . . . .	xvii
CHAPTER 1 INTRODUCTION . . . . .	1
CHAPTER 2 MINING SAFETY BACKGROUND . . . . .	3
CHAPTER 3 SENSORS TECHNOLOGY LITERATURE REVIEW . . . . .	5
3.1 Hazard Detection . . . . .	5
3.1.1 Photo & Video . . . . .	6
3.1.2 Radio Antenna . . . . .	6
3.1.3 Thermal . . . . .	6
3.2 Vibration Sensors . . . . .	6
3.2.1 IMU . . . . .	6
3.2.2 Custom MEMS . . . . .	7
3.2.3 Piezo . . . . .	7
3.2.4 Acoustic . . . . .	7
3.3 Force Sensors . . . . .	7
3.3.1 Strain gauges . . . . .	7
3.3.2 Capacitive . . . . .	8
CHAPTER 4 SENSOR MODELING AND CLASSIFICATION METHODS . . . . .	9
4.1 Linear Sensor Modeling . . . . .	9
4.2 Classification Methods . . . . .	10
CHAPTER 5 CAPACITIVE LOAD CELLS TO PROMOTE WORKER SAFETY . . . . .	12

5.1	Abstract . . . . .	12
5.2	Introduction . . . . .	12
5.3	Material and Wear Classification . . . . .	15
5.3.1	Classification Methods . . . . .	16
5.3.2	Sensor Design Literature Review . . . . .	20
5.3.3	Sensor Design . . . . .	21
5.3.4	Sensor Characterization . . . . .	23
5.4	Rock Cutting Experiment . . . . .	23
5.5	Classification Results . . . . .	25
5.6	Discussion . . . . .	27
5.7	Conclusion . . . . .	31
5.8	Disclosures . . . . .	31
5.8.1	Conflicts of interests . . . . .	31
CHAPTER 6	TOOL WEAR CLASSIFICATION FOR CONICAL PICKS USING ACOUSTIC FOURIER SPECTRA MAGNITUDE . . . . .	32
6.1	Abstract . . . . .	32
6.2	Introduction . . . . .	32
6.3	Background . . . . .	33
6.4	Materials and Methods . . . . .	35
6.5	Preprocessing . . . . .	36
6.6	Classification . . . . .	38
6.6.1	K-Nearest Neighbors . . . . .	39
6.6.2	Support-Vector Machine . . . . .	39
6.6.3	Multi-layer Perceptron Classifier . . . . .	40
6.7	Results . . . . .	40
6.8	Discussion . . . . .	43
6.9	Conclusion . . . . .	44
6.10	Acknowledgments . . . . .	44

6.11 Declarations . . . . .	44
6.11.1 Funding . . . . .	44
6.11.2 Conflict of interest . . . . .	45
6.11.3 Availability of data and materials . . . . .	45
6.11.4 Code availability . . . . .	45
CHAPTER 7 CAPACITIVE LOAD CELLS FOR UNDERGROUND MINING FORCE SENSING APPLICATIONS . . . . .	46
7.1 Abstract . . . . .	46
7.2 Introduction . . . . .	47
7.3 Materials and Methods . . . . .	50
7.3.1 Analytical Modeling . . . . .	53
7.3.2 Air Gap . . . . .	55
7.3.3 Closed Area . . . . .	56
7.4 Regression Techniques . . . . .	57
7.5 Results . . . . .	59
7.6 Air Gap Load Frame Characterization . . . . .	60
7.6.1 Rock Cutting and Model Fitting . . . . .	60
7.7 Discussion . . . . .	64
7.8 Conclusion . . . . .	64
7.8.1 Acknowledgments . . . . .	65
7.9 Declarations . . . . .	65
7.9.1 Funding . . . . .	65
7.9.2 Conflict of interest . . . . .	65
7.9.3 Availability of data and materials . . . . .	65
7.9.4 Code availability . . . . .	65
CHAPTER 8 LOAD CELL DESIGN COMPARISON . . . . .	66
8.1 Load Frame Testing . . . . .	66
8.2 Rock Cut Testing . . . . .	66

CHAPTER 9 LONGER DOWNSAMPLING RATES FOR ACOUSTIC CLASSIFICATION . . . . .	69
9.1 Alternate Acoustic Preprocessing Methods . . . . .	69
9.2 Comments on Data Size . . . . .	70
CHAPTER 10 SENSOR LINEARITY AND IMPLEMENTATION RECOMMENDATIONS . . . . .	72
REFERENCES . . . . .	74
APPENDIX A LASER WELDING PROCEDURE . . . . .	88
APPENDIX B CAPACITANCE SIMULATION . . . . .	89
APPENDIX C COMPUTER AIDED ANALYTICAL SOLUTIONS . . . . .	90

## LIST OF FIGURES

Figure 1.1	Continous Miner. The machine operator must stand close to the machine and cutting interface to control the machine. The operators use many cues, but ultimately must track if they are cutting the target material and the state of tool wear. Allowing operators to maintain a greater distance while giving them the feedback they require can improve production and safety. . . . .	2
Figure 3.1	The dynamic flexible PCB capacitive load cell. This sensor is used for the first branch of this research. It has a thin film layer between the electrodes made of polyimide that deforms when pressure is applied. The sensor is housed in a steel case for protection and additional stiffness and protection from electro-magnetic interference. . . . .	8
Figure 4.1	A model of the sensor as a system of springs and dampers. The PI can be modeled with a general visco-elastic model with repeating Maxwell elements. Here, it is summarized as $K_p$ . The springs representing the steel case top and bottom, $K_{top}$ and $K_{bottom}$ , are much stiffer than the midsection. Similarly, $K_{walls}$ , of the steel case, is much stiffer than $K_p$ . Thus the total device stiffness is readily approximated by the stiffness of the device walls. . . . .	10
Figure 4.2	The stackup for the FlexPCB sensing membrane. The outer PI layers are 12.5 $\mu\text{m}$ tall while the inner layer is 25 $\mu\text{m}$ . The adhesive layers are 15 $\mu\text{m}$ and the copper layers are 12 $\mu\text{m}$ . The total membrane height is about 100 $\mu\text{m}$ . Due to the very thin thickness of the dielectric film, the deformation characteristics will be dominated by the interaction of the complex molecular chains and are expected to be nonlinear. . . . .	11
Figure 5.1	A prototype of the sensor integrated with the U92 4.0 22NB Conical Pick and K35 Block system, from Kennametal. The device is shown without the measurement collection system and is situated between the sleeve and the block. The FlexPCB interface is exposed, which provides access to the capacitive sensors' electrodes. A steel case protects the FlexPCB sensor and provides the necessary stiffness to transfer the input forces to the sensor. An embedded electronics platform, not shown in this figure, takes measurements suitable for dynamic classification of tool-wear and material. A cutaway of the sensor shows the thin film design for the force sensor. . . . .	14
Figure 5.2	The different pick wear levels. The <i>new</i> , <i>moderate</i> , and <i>worn</i> pick tips have spherical diameters of 3.71 mm, 17.9 mm, and 27.5 mm respectively. This approximates and even wear pattern. The <i>moderate</i> and <i>worn</i> tips were artificially worn using a lathe. . . . 14	
Figure 5.3	A cutaway of the sensor with the geometric parameters shown. The dimensions of the walls may be tuned to give the sensor the appropriate stiffness. The thickness of the top and bottom plates do not significantly influence the overall stiffness of the device. . . 22	
Figure 5.4	The triangular load profiles and the resulting measurements from the sensor. The sensor response is not symmetric and therefore non-linear. Lower load rates cause greater changes in displacement, which is consistent with previous studies for thin film polyimide. . . . .	24

Figure 5.5	The case deformation during the load frame tests. The case deformation is symmetric for the loading and unloading phases, it also has a consistent slope for force over displacement. This means the case has approximately linear deformation for these load profiles.	24
Figure 5.6	The Linear Cutting Machine in action. Hydraulic actuators push the sample into the cutting tool while the custom sensor and the embedded strain gauges record measurements. The tool is normally surrounded by the plastic curtain to aid in capturing dust for a simultaneous study of the effect of tool wear on dust generation.	25
Figure 5.7	Measurements for typical rock cuts with different tool wear levels. The measurements from the linear sensors are shown in the top graph while the measurements from the custom sensor are shown below.	27
Figure 5.8	The frequency signature distributions collected from the custom sensor organized by material. The concrete material shows exponential decay after each primary mode, while the limestone has a more varied response. These differences can be used for classification of the signals by material.	28
Figure 5.9	The frequency signature distributions collected from the custom sensor organized by tool wear. The New tool has a distinct response compared to the Moderate and Worn tools, and the energy in the higher modes generally increases with wear. These differences can be used for classification of the signals by tool wear.	29
Figure 5.10	Bar chart with error bars for F1 score distributions by window size. For tool wear, both sensors were able to provide sufficient data for very accurate classification. For material classification, the capacitive sensor generally performed better than the strain gauge sensor. Some of the differences in performance are significant within the application and sensor combinations, but in general performance was similar across window sizes.	30
Figure 5.11	Performance of different preprocessing methods for each application. In general, normalization after transformation proved most effective for the frequency based techniques. Using the normalized time domain data was most effective for tool wear classification.	30
Figure 6.1	The Linear Cutting Machine at the Earth Mechanics Institute of Colorado School of Mines.	35
Figure 6.2	The tips of the conical picks with different wear levels used for the experiment.	36
Figure 6.3	The natural distribution of frequency spectra magnitude and time domain data of each wear category for collected data.	37
Figure 6.4	The mean frequency spectra magnitude after normalization for each wear category and a comparison between the categories for significant differences.	38
Figure 6.5	The mean F1 score and standard deviation for K-nearest neighbors method.	41
Figure 6.6	The mean F1 score and standard deviation for the tested support-vector machine method.	41
Figure 6.7	The mean F1 score and standard deviation for the tested multi-layer perceptron methods.	42

Figure 7.1	<b>Graphical Abstract</b>	46
Figure 7.2	The network proposed for integrating our sensor with the continuous miner. Individual sensors can be linked to an edge processor on the drum which aggregates the force data via CAN bus, a robust interface for sensor networks. From the edge processor on the drum, labeled "Drum Processor", force data can be sent wirelessly to an edge processor on the machine chassis. There, the data can be parsed into a displayable format for immediate use by the machine operator and also sent up to the surface to be stored in a central server for processing by a mine analyst to gain insight into operator performance. The analyst and the operator can then communicate to increase efficiency and safety.	48
Figure 7.3	Two sensor prototypes. The one on the left has only been used for characterization in a load cell with controlled parameters. The one on the right has been through the same calibration as well as a controlled rock cutting experiment. During the rock cutting experiment, the air gap of the sensor is crushed out, altering the model but still giving a mostly linear sensor. The exposed sensor membrane was inadvertently cut by the edge of the second sample on the last cut. The walls of the sensor have retained much of their thickness, but they have deformed slightly to match the tooling.	50
Figure 7.4	The setup for the load frame characterization of the sensor in the air-gap configuration, shown in the sensor cross section. The load frame applies a controlled loading profile to the sensor, allowing the response of the sensor to be compared against a controlled input. The load frame measures both force and displacement while the sensor's capacitance is measured by the interface circuit. Forces in this test ramp up to 200 kN and back down at a controlled linear rate.	51
Figure 7.5	The setup for the rock cutting experiment. Strain gauges measure the forces on the cutting tool from close proximity while hydraulic actuators drag the rock sample against the cutting tool. The sensor is located between the sleeve and the block of the cutting tool, as shown in the profile view diagram. In this setting, the sensor is in the crushed gap configuration, shown in the sensor cross section. Forces in this test are less than 100 kN, but the rate of change of force is large and variable.	52
Figure 7.6	Cross section models for the two sensor modes. The top model has the air gap intact, resulting in one region which has variable capacitance. The bottom model has a closed air gap area, resulting in a stiffer sensor with two regions of variable capacitance. The top model is valid for sensors which have not undergone significant plastic deformation, while the bottom model is accurate for sensors after they have formed to the cutting tool. The measured stiffness of the case in the air gap configuration, $K_w$ , is around 780 meganewtons/meter. In the closed area configuration, the polyimide contributes additional stiffness, as it occupies more than twice as much area as the steel walls and is very thin in comparison. The soldermask and polyimide are lumped together for the model of $r_1$ since the soldermask is thin in comparison to the polyimide and has similar properties.	54
Figure 7.7	The strain of the physical sensor cases during the tests.	61
Figure 7.8	Force profiles and capacitive measurements during loading for the two test sensors.	61
Figure 7.9	The relationship between measured resonant frequency and applied force for each sensor.	61

Figure 7.10	Measurements from both the system strain gauges and the custom sensor for the new tool.	63
Figure 7.11	Measurements from both the system strain gauges and the custom sensor for a worn tool.	63
Figure 7.12	Mean Absolute Error distributions for different input filter conditions. The markers and dashed lines represent the median, while the dots and shaded area represent the quartile and min/max values respectively. Lower scores are better.	63
Figure 7.13	$R^2$ score distributions for different input filter conditions. The markers and dashed lines represent the median, while the dots and shaded area represent the quartile and min/max values respectively. Higher scores are better.	64
Figure 8.1	Comparison of original design, left, and improved design, right. The original design was noisy, had slightly less initial plastic deformation, and similar sensitivity when compared to the improved “Air Gap Configuration”. The air gap design had much better repeatability and less hysteresis in comparison to the original. The air gap design ultimately became more sensitive when used in the rock cutting tests.	67
Figure 8.2	The individual channel measurements and the resulting force predictions for a few choice cuts, using the “Crushed Gap Configuration” of the second sensor design. The change in resonant frequency from the initial value is plotted versus the target force for each sensing channel in the sensor. The resulting force estimate provided by both the linear regression and the neural network using the 2nd order polynomial expansion are shown. Ideal performance is shown along the magenta line. The neural network method is able to untangle some of the non-linearity in the response. The performance of the neural network is comparable to the strictly linear model. The sensor is not completely linear, but can still provide useful measurements using a linear model.	68
Figure 9.1	Data distributions for the tested wear categories using additional Fourier based preprocessing techniques. The square of the magnitude is an estimate of the power spectral density of the signal. The square root of the magnitude conditions the signal so that the higher frequencies with small magnitudes have magnitudes closer to the lower frequencies with large magnitudes. Neither of these methods gave better classification results than the unmodified Fourier spectra magnitude.	70
Figure 9.2	Tests for significant differences in frequency content between wear categories for the additional Fourier based preprocessing techniques. The square root was able to bring the differences between more high frequencies into significance compared to the square, or power spectral density. Squaring a signal will make outliers larger, while the square root conditions by bringing all numbers closer to unit value. Neither of these methods adds more information or improves the signal basis for classification over the spectra magnitude. However, they do perform much better compared to using time domain data.	71

Figure 10.1	Power spectral density of sensor, target, and transfer function between them. The regression target has been low pass filtered with a cutoff frequency of 10 Hz, which can be seen by the steep drop in magnitude at this point. The individual sensor channels have the same filter applied to limit high frequency input. The cross spectrum, $P_{yx}$ , shows that there is good correlation between the low frequency components of the estimate and the target. The transfer function between the estimate and the target suggests that additional filtering after the regression method could improve results. Post-processing requirements depend on the application, and additional filtering after regression could be a useful technique for tuning performance. . . . .	73
Figure 10.2	The air gap sensor membrane, left, and an assembled prototype, right. The sensor case provides additional protection from the environment. The device is assembled via later welding. Future sensor designs could omit the steel case and integrate the sensor directly within the block or sleeve of the tool. This type of sensor measures cutting forces via the change in capacitance caused by the displacement of the top of the case when force is applied. . . . .	73
Figure B.1	Simulation of electric field to determine capacitance properties of air gap design. The top image shows the relaxed state of the sensor, with low electric field strength in the free space around the electrode. When the air gap compresses, the electric field becomes much stronger and more concentrated, this is measured as an increase in capacitance. Fringing effects appear to be minimal in this simulation of the design. . . .	89
Figure C.1	Result of computation of device frequency and sensitivity over the required input range. . .	90
Figure C.2	Result of computation of device frequency and sensitivity over the required input range. . .	91

## LIST OF TABLES

Table 2.1	Selected statistics from <a href="http://cdc.gov/NIOSH-Mining/MMWC/">cdc.gov/NIOSH-Mining/MMWC/</a> . Accessed April 14th, 2024 . . . . .	3
Table 3.1	Summary of technology review, ‘X’ indicates requirement is met. . . . .	5
Table 5.1	Preprocessing Pipeline Steps, $\ \cdot\ $ , $\cdot^2$ , and $\sqrt{\cdot}$ are element-wise absolute value, square, and square root respectively. . . . .	17
Table 5.2	Scoring metric and test/train ratios for each application . . . . .	27
Table 5.3	Confusion Matrix for Material Classifier; Normalized by prediction New Picks, 0.3 in Penetration, 0.2s Window, 50:50 test and train, PSD w/ post norm. . . . .	31
Table 5.4	Confusion Matrix for Tool Wear Classifier; Normalized by prediction All Materials, All Penetrations, 0.2s Window, 50:50 test and train, Normalized Time Domain Data . . . . .	31
Table 6.1	Confusion Matrix for Acoustic Wear Classifier, Normalized by True Class Size. . . . .	42
Table 7.1	Rock cut conditions tested, coal samples and conical picks . . . . .	52
Table 7.2	Nominal design values for sensor, crushed gap reduces $h$ , $d_{r_1}$ , and $d_{r_2}$ . . . . .	55
Table 7.3	Regression methods and number of inputs and trainable parameters. . . . .	57
Table 7.4	Model values for linear regression coefficients and bias terms. . . . .	60
Table 10.1	Changes to design parameters that would improve certain categories . . . . .	72
Table A.1	Test matrix for laser welding, ‘o’: perform test; ‘x’: test not performed . . . . .	88

## LIST OF ABBREVIATIONS

A-weighted decibel . . . . .	dBA
Capacitive . . . . .	Cap.
Controller Area Netwrok . . . . .	CAN
Feed-Forward Neural Network . . . . .	FFNN
Filter . . . . .	Filt.
Full time equivalent . . . . .	FTE
Hertz . . . . .	Hz
Inertial Measurement Unit . . . . .	IMU
Inter-Intergrated Circuit . . . . .	I2C
K-Nearest Neighbors . . . . .	KNN
Linear . . . . .	Lin.
Magnitude . . . . .	Mag.
Mean Absoulute Error . . . . .	MAE
Micro-Electro-Mechanical Systems . . . . .	MEMS
National Institute of Occupational Safety and Health . . . . .	NIOSH
Polynomial . . . . .	Poly.
Printed Circuit Board . . . . .	PCB
Regression . . . . .	Reg.
Support-Vector Machine . . . . .	SVM
United States Dollar . . . . .	USD
United States of America . . . . .	U.S.A.
Universal Serial Bus . . . . .	USB
centimeters . . . . .	cm
fast Fourier transform . . . . .	FFT
giga-Newtons . . . . .	GN

inches	in.
kilo-Hertz	kHz
kilo-Newtons	kN
mega-Hertz	MHz
mega-Newtons	MN
meters	m
micrometers	$\mu\text{m}$
milli-Watt	mW
multi-layer perceptron	MLP
pico-Farad	pF
radial basis function	RBF
seconds	s

## ACKNOWLEDGMENTS

Thanks Mom(s).

This work is dedicated to my grandfather, Frank Oltmanns, an open pit uranium miner.

## CHAPTER 1

### INTRODUCTION

The use of tools in mining has only accelerated production over time. Eventually, robotic mining systems will determine optimal work patterns and execute the planned operations with precision. Progress towards this horizon is gradual in the mining industry. Improvements to safety in underground coal mining have been sparse recently, and the National Institute of Occupational Safety and Health (NIOSH) has sponsored programs like this thesis to accelerate the next industrial revolution. This work focuses on the development of techniques and sensors to measure rock cutting forces and determine rock type and tool wear.

Machine operators in underground coal mines are routinely exposed to dark, dusty, noisy, and hazardous conditions. When doing their job of operating the continuous mining machine, they must stand close enough to the cutting interface to infer where they are cutting and if their tools are worn and need to be replaced. They must also stand far enough away to avoid the dangerous rock cutting process. A well lit and clean view of a continuous miner is shown in Figure 1.1<sup>1</sup>. The long term exposure to hazardous noise and dust causes occupational health issues for miners which work for more than several years.

The technologies proposed in this dissertation could be used to automate feedback collection during the rock cutting process, allowing operators to perform their duties from a safer location. This work investigates using measured frequency responses to predict material and wear conditions using a non-linear dynamic capacitive load cell. An acoustic tool wear detection method is also developed using this same premise. The capstone of this project is a custom capacitive load cell that is able to measure rock cutting forces using a linear model. Each of these three works are respectively summarized in the included journal articles.

This work was sponsored by NIOSH contract 75D30119C05413. It is a continuation of prior work at Colorado School of Mines [1]. The previous work employed piezo electric sensors to make measurements to estimate rock cutting parameters. Our work focuses on use of a capacitive based load cell. Study of rock fracture mechanics [2] and the effects of tool geometry during rock cutting [3–5] have long been pursued to increase mine efficiency and safety. By providing an *in-situ* force sensor, this work provides a means for direct measurement of rock cutting parameters. In addition to enabling operators to perform their roles from a distance, this device could also be used to optimize tool geometries by providing quick and direct feedback of the cutting forces.

---

<sup>1</sup>Pictured is the ‘Remote Continuous Miner HM21 Joy Used for underground coal mining’, originally uploaded to Wikipedia by user Xlxgoggaxlx under the Creative Commons Attribution-Share Alike 3.0 Unported license Image Source/License: [https://commons.wikimedia.org/wiki/File:Continuous\\_Miner.jpg](https://commons.wikimedia.org/wiki/File:Continuous_Miner.jpg)



Figure 1.1 Continuous Miner. The machine operator must stand close to the machine and cutting interface to control the machine. The operators use many cues, but ultimately must track if they are cutting the target material and the state of tool wear. Allowing operators to maintain a greater distance while giving them the feedback they require can improve production and safety.

Safety in mines is a serious issue, and the next chapter, Ch. 2, discusses its current state. The chapter after that, Ch. 3, covers additional background information regarding sensor choices. Then, Ch. ?? discusses modeling of the chosen sensors and materials. The journal articles that summarize the work are included next. Doing rock material type and tool wear classification with a capacitive sensor and tool wear classification with an acoustic sensor are discussed in Chapter 5 and Chapter 6, respectively. Chapter 7 discusses the development of the sensor with more linear performance. Each article describes the implemented classification or regression methods specific to the topic.

After the articles, 8 compares the different capacitive sensor implementations and discusses the linearity of the final sensor design while providing additional characterization data. An additional chapter, 9, describing extensions of the acoustic processing methods is given after that. The last chapter, 10 highlights the new contributions of this research and gives recommendations for future work and implementation. This dissertation and the constituent articles have been published as Open Access and are released into the public domain. If you have any questions about this work, you can contact me, the author, at: austinfoltmanns at gmail dot com with the subject line containing "THESIS".

## CHAPTER 2

### MINING SAFETY BACKGROUND

In the thesis by Moore [4], the author outlines history of mining tools dating back to the 1600s. This is when blasting was introduced to the mining process. Hand tools dominated until the invention of steam powered machines in the mid 1800s. Around 100 years later, at the time of publication of the thesis, compressed air hammer drills were the most popular implement. These techniques and the mining drill bits that they used evolved with each other over time.

The introduction of the continuous mining machine increased productivity and was generally regarded as safe since the operator was enclosed in a shielded cab. Around the 1980s, the remote control for the continuous mining machine led to further increases in productivity, but with differing results for safety [6]. The remote control provides the operator greater visibility of the operation, but at increased risk of injury from the machine or tunnel collapse. The crush hazards from the machine were not mitigated until the introduction of the personnel proximity detector, around the turn of the millennium. The detector prevents the machine from advancing into workers which are wearing the device [7].

Safety in underground coal mines has not improved over that last decade. Statistics from 2011 to 2022, shown in Table 2.1, show that coal mining has remained a dangerous industry, especially for underground coal mine operators. Mine technology has been the subject of extensive review [8–11]. Different areas of research include process control and hazard detection. Process control improvements can avoid hazardous conditions from being created, making them proactive rather than reactive.

Table 2.1 Selected statistics from [cdc.gov/NIOSH-Mining/MMWC/](https://www.cdc.gov/niosh-mining/MMWC/). Accessed April 14th, 2024

Year	Coal Injury Rate (Per 100 FTE)	All Injury Rate (Per 100 FTE)	Underground Coal Mine Operator Deaths	All Mining Deaths (Coal included)
2011	2.49	1.94	9	37
2012	2.40	1.86	12	35
2013	2.42	1.82	14	41
2014	2.48	1.83	10	43
2015	2.33	1.70	8	26
2016	2.40	1.64	7	24
2017	2.56	1.64	8	27
2018	2.22	1.52	6	27
2019	2.23	1.53	7	27
2020	2.30	1.42	3	29
2021	2.37	1.49	6	37
2022	2.24	1.42	6	29

In the cited reviews, examples of sensors in mining include gas detectors, tunnel mapping, personnel detection, material composition measurement and more. In the work by Ralston [10], goals for autonomous mining systems are outlined in stages from local manual control to full automation. Current remote controls allow operators more mobility during cutting, and addition of more process feedback can allow them to be further from the cutting interface. The sensor developed in this work could allow operators to perform tele-operation or tele-supervision, whereby they are providing higher level commands to the machine using remote sensors for feedback, possibly augmented with feedback collected with their own senses.

Previous efforts to improve safety and efficiency have tried automating the continuous mining process, but fell short on being able to totally take over for human operators [1, 12]. Experienced operators are an invaluable resource. They have expert knowledge gained through years of working in difficult conditions, frequently putting themselves in hazardous locations to collect the feedback they need. Augmenting their expertise with objective feedback and allowing them to stay at a safer distance stands to improve outcomes beyond fully human or fully autonomous control.

When working in an underground coal mine, machine operators must stand close to the cutting interface and the machine to collect feedback to operate the machine. This places them at risk of being crushed by the machine or otherwise injured due to hazardous tunnel conditions. Operators with long term careers are inevitably injured from the loud noises and harmful dust in the environment. As long as this type of operation remains economically viable, it is likely to continue.

Improving both safety and efficiency is the optimal path for new technologies in an underground mine [13]. Mining safety has improved gradually over time and could currently be improved by moving operators further from the cutting interface. Efficiency can be improved by implementing autonomous process control and feedback mechanisms for optimizing tool change scheduling and cutting control. To enable these outcomes, we seek feedback mechanisms which can determine quantities of interest for the process. The next chapter discusses sensor technologies that were considered for determining tool wear, material type, and cutting forces in underground coal mining.

## CHAPTER 3

### SENSORS TECHNOLOGY LITERATURE REVIEW

For this iteration of the smart bit project, many different sensing technologies were considered. Rock cutting tools are consumed quickly during underground mining, and need replaced frequently to maintain cutting efficiency. Sensors at the cutting interface must be low power, low cost, and robust to be successful in the underground mine. A table of different sensing technologies and requirements is shown in Table 3.1. Each sensing technology has different pros and cons, and are discussed in the following subsections.

For Table 3.1, the requirements are interpreted as follows: robustness considers how well a sensor can perform after exposure to conditions outside of its typical operating range as well as how well the sensor is able to reject electrical and other noise sources, low cost for this study is defined as the sensor being a fraction of the cost of the cutting tools and at the time of writing a target of 10 USD or less is chosen, low power for this study means the sensor requires less than 10 mW of power or provides its own. The different sensors that are considered have been used successfully in other domains. The different categories of use are hazard detection, vibration sensing, and force sensing.

Table 3.1 Summary of technology review, ‘X’ indicates requirement is met.

Sensor	Robust	Low Cost	Low Power	Used Here	Application
IMU		X			Vibration
Custom MEMS			X		Force
Photo & Video					Hazard
Piezo		X	X		Vibration
Radio Antenna	X	X	X		Hazard
Thermal	X	X	X		Hazard
Strain Gauge		X		X	Force
Acoustic		X	X	X	Vibration
Capacitive	X	X	X	X	Force

### 3.1 Hazard Detection

These sensors observe tunnel conditions for hazardous situations as they occur. This reactive approach is better than not having any kind of warning system, but fundamentally can only alert miners to problems after the hazardous situation has developed. These types of sensors monitor the mine in different locations and wait for small changes that typically indicate much larger changes are about to happen.

### **3.1.1 Photo & Video**

Photo sensors use precision cameras to monitor the rock face for changing conditions. Sensors today that use this technology monitor the rock face to anticipate fall or fracture [16]. Use of these sensors for autonomous control is inhibited by the dark and dusty conditions in the mine. Cameras generally cannot be dropped or hit repeatedly, and require the most power out of the considered categories, and are the most expensive. For these reasons, photo and video sensors were not used for this study.

### **3.1.2 Radio Antenna**

Did you know that rocks make radio waves when they break apart [17]? The destruction of molecular bonds releases lots of energy and some of this energy is sent to the electromagnetic spectrum. This is a more recent area of study, but presents potential benefits like passive operation and low cost fabrication. Depending on construction, these types of sensors can be made robust. Processing of these types of measurements is a new area of research, so radio antennas are not used for this study, but would be a good topic for future research.

### **3.1.3 Thermal**

Increasing tool tip temperature tends to wear rock cutting tools at a faster rate. There have been efforts to embed thermocouples into cutting tools to monitor hot spots and track bit health via temperature measurements [18]. These hot spots can be sources of ignition if they are not monitored closely. These types of sensors are robust, low cost, and low power, but they are also very low bandwidth. Tracking material type and cutting forces could be difficult using thermal measurements alone. However, thermal measurements augmented with force measurements stands to improve accuracy for tracking tool wear conditions. For these reasons, thermal sensors are not used in this study.

## **3.2 Vibration Sensors**

These sensors monitor vibrations. They have been used in industries other than underground mining for topics like predictive maintenance. It is known that changes in vibrational modes are often the result of changes in tool geometry or changes in material being cut. These changes in vibration can be captured and classified to identify when tools have become too worn or if the material under the tool has changed. Vibration sensors do not directly measure force, but instead measure the oscillations in the overall system.

### **3.2.1 IMU**

The IMU, or inertial measurement unit, is a type of device which uses a deflecting element to determine inertial and gyroscopic measurements. They can be used for material classification via vibrations produced

by impact [14]. They range in price and performance, but in general, they are sensitive and can be easily damaged by excessive forces or vibrations. IMUs also require active power to operate, typically using electromagnetic fields to deduce the position of their test mass. For these reasons, IMUs were not used for this study.

### **3.2.2 Custom MEMS**

Beyond IMUs, custom micro-electro-mechanical sensors (MEMS), are designed to be very low scale sensors which can operate at low power points from their reduced size. Low cost wireless vibration sensor systems have been demonstrated using this technology [15]. The construction of these devices can be labor intensive, and coal mining has very little room for additional cost. Additionally, their delicate elements can easily be damaged by excessive forces. For these reasons, custom MEMS were not used for this study.

### **3.2.3 Piezo**

Piezo sensors use material which produce charge when compressed. These materials are very efficient, producing charge due to their innate composition. Piezo sensors are generally brittle, and too much force can damage them. Generally low in cost, these sensors have been used for previous iterations of the smart bit study [1], but not this study.

### **3.2.4 Acoustic**

Underground coal miners use acoustic cues as part of machine operation. Acoustic sensors are typically piezo based, but separated from the source of vibration by a medium like air. These types of sensors are very low cost and can be given an enclosure to make them robust. Being piezo based, they are also low power. Operators use acoustic cues to determine material type and tool wear. This study investigates the use of acoustic sensors for tool wear classification.

## **3.3 Force Sensors**

These sensors measure forces. In underground mining, and most other situations, worn tools require more force to cut material than tools which are not worn. Also, materials that have different compositions will require different amounts of force to cut. Since force is so strongly correlated with the categories of interest, rock type and tool wear, force sensors are especially relevant to this study.

### **3.3.1 Strain gauges**

Strain gauges are the classic method for measuring forces with precision and accuracy. These sensors are small segments of resistive wire, typically superglued to a metal fixture, which measure the small deflections of the material by changing length and resistance. They have been used recently to measure

conical pick forces [19]. Using a resistive segment of wire is a low cost method, but the accuracy depends on the power input. The sensors can be delicate to being scratched, but must be somewhere the cutting tool is deflecting. The cutting tool is generally very stiff, and so deflection away from the point of contact between the rock and tool is very small, making strain gauge placement difficult. Strain gauges are used as the baseline sensing technology for the load cell and rock cutting laboratory equipment. They are not investigated for use in an underground mine for this study.

### 3.3.2 Capacitive

The capacitive sensor is a technology that has been made more and more practical over the last 20-30 years. These sensors come in many forms, using changes in distance, area, or dielectric permittivity of the sensing element to make measurements. These sensors are robust to changing environmental conditions and noise, while also being low cost and low power. Capacitive sensors are used in this study, and a prototype is shown in Figure 3.1.



Figure 3.1 The dynamic flexible PCB capacitive load cell. This sensor is used for the first branch of this research. It has a thin film layer between the electrodes made of polyimide that deforms when pressure is applied. The sensor is housed in a steel case for protection and additional stiffness and protection from electro-magnetic interference.

## CHAPTER 4

### SENSOR MODELING AND CLASSIFICATION METHODS

For this work, polyimide dielectric based capacitive load cells were chosen as the primary sensing apparatus due to their prescribed robustness, low manufacture cost, and low power requirements.

Motivated by the selection of thin film polyimide, models for thin film deformation were studied for this work. The deformation of polyimide is linear for thick films and small deformations, but for thin films, on the mesoscale of dozens of micrometers, polyimide films have nonlinear deformation. These characteristics are manifested as creep, hysteresis, and temperature dependence.

To avoid problems in modeling caused by these reactions, different approaches are used to determine rock material type and tool wear conditions from the sensor measurements. In the case presented in Ch. 7, the sensor film thickness has been dialed-in, and the measurements are much more linear with respect to the input force. The sensor model for the linear sensor case is discussed in the next subsection, after that, the classification methods used to avoid problems with creep, hysteresis, and temperature dependance are discussed.

#### 4.1 Linear Sensor Modeling

It is axiomatic that a linear and time-invariant sensor is an ideal sensor for measuring physical quantities. Such a sensor would present an easily measured value that is a fixed multiple of another physical quantity that is desired to be measured without any dependence on the measurement history. Such a sensor is difficult to attain, but non-ideal characteristics can still be modeled. Thin film deformation can be modeled using viscous elements, as shown in Figure 4.1. This is only an approximation, and depending on how nonlinear the dielectric deformation response is, this model might not accurately capture the dynamics of the system. The system overall is nonlinear, and with a material this viscous, cycling the film rapidly will result in changes to the vibrational modes.

The stackup for the sensor membrane for the first iteration of the capacitive load cell is shown in Figure 4.2. This model had a very thin inner layer, which resulted in nonlinear dynamics. The next iteration of the sensor used a thicker membrane, which resulted in a more linear sensor. The non-linearity of the first design was not an issue for tool wear or material classification, but did impede using the measurements for force measurements.

When considering the design of the more linear sensor, the model can be simplified to the linear case without a great loss in accuracy. The use of a small feed-forward neural network are able to model the nonlinearity present in the more linear design and further improve the accuracy. The fact that a linear

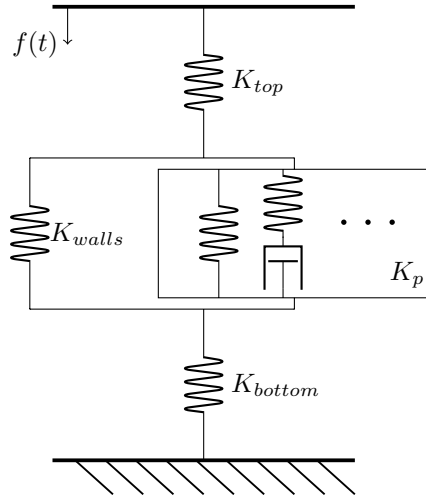


Figure 4.1 A model of the sensor as a system of springs and dampers. The PI can be modeled with a general visco-elastic model with repeating Maxwell elements. Here, it is summarized as  $K_p$ . The springs representing the steel case top and bottom,  $K_{top}$  and  $K_{bottom}$ , are much stiffer than the midsection. Similarly,  $K_{walls}$ , of the steel case, is much stiffer than  $K_p$ . Thus the total device stiffness is readily approximated by the stiffness of the device walls.

model is able to be used with the sensor and provide good accuracy means the sensor is approaching ideal behavior. The fact that a neural netowrk model improves performance reveals that the system still has latent non-linearities.

Increasing the dielectric thickness will make it deform more linearly. Increasing stiffness from the steel walls,  $K_{walls}$ , would also increase the sensor linearity. Other types of capacitive sensor designs, like those which translate the electrodes overlapping areas, are inherently more linear than the compressing plate design used for this research. However, for small deformations, the hyperbolic relationship between capacitance and plate distance is approximately linear.

## 4.2 Classification Methods

Other items which govern the vibrational forces during cutting include the material type and the tool wear. Different rock types have different fracture mechanics, and these differences can be measured and classified. Different tool wear levels require different amounts of cutting force, and will result in changing fracture mechanics dependent of the tool's geometry.

All of these changes in vibrational modes and forces can be tracked in the frequency domain as changes to the emitted spectra. For this research, it is known that energy is moving from certain vibrational modes to other vibrational modes across the categories of material type and tool wear. This shift in energy over the spectra can be measured by using the magnitude of the Fourier transform coefficients for a short duration sample.

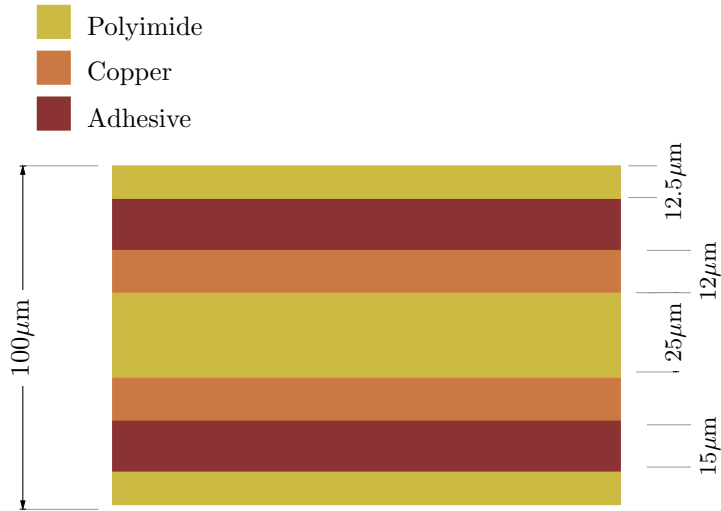


Figure 4.2 The stackup for the FlexPCB sensing membrane. The outer PI layers are  $12.5 \mu\text{m}$  tall while the inner layer is  $25 \mu\text{m}$ . The adhesive layers are  $15 \mu\text{m}$  and the copper layers are  $12 \mu\text{m}$ . The total membrane height is about  $100 \mu\text{m}$ . Due to the very thin thickness of the dielectric film, the deformation characteristics will be dominated by the interaction of the complex molecular chains and are expected to be nonlinear.

As the Fourier spectra magnitude coefficients change, these changes can be used to classify the conditions that caused them. Data-driven classification techniques are used to identify these differences and predict the cutting conditions. The methods are the K-Nearest Neighbors, the support-vector machine, and multilayer perceptron classifier. These methods are able to categorize the different modal excitations present during different rock material and tool wear conditions without needing the force measurement.

For example, worn tools change the rock fracture process to more of a crushing operation, resulting in lower and rumblier vibrations. Likewise, different materials will fracture in different patterns and frequencies due to their constitution. On average, the statistical distribution of a measurement recorded during consistent rock material type and tool wear conditions will differ from the distribution of a measurement recorded during different conditions. This difference is identified by the classification methods and used to make classifications.

## CHAPTER 5

### LOW-PROFILE CAPACITIVE LOAD CELLS FOR UNDERGROUND MINING MATERIAL AND WEAR CLASSIFICATION TO PROMOTE WORKER SAFETY

**License: Creative Commons licence CC BY:** This licence allows readers to copy, distribute and transmit the Article as long as it is attributed back to the author. Readers are permitted to alter, transform or build upon the Article, and to use the Article for commercial purposes. Please read the full licence for further details at -

<http://creativecommons.org/licenses/by/4.0/>

#### 5.1 Abstract

This work proposes a capacitive load cell for conical picks to enable underground continuous mining machine operators to perform their roles away from known hazardous regions near the machine. The load cell is embedded in commercially available flexible printed circuit board, integrates with the target tooling, and demonstrates in-situ force sensing of vibration signatures for continuous mining cutting tools. Changes in material constitution, tool mass, and tool geometry cause modal variations in vibrational response measurable with force sensors at the cutting interface. Time-series measurements are captured during rock cutting tests using a linear cutting machine. These measurements are segmented into small windows, less than 0.25 seconds, and are preprocessed using the fast Fourier transform, which highlights the modal variations. The transformed measurements are then classified into different material and wear categories using support-vector machines with the radial basis function kernel. Different normalization schemes and Fourier transform methods are tested for signal preprocessing. Results show that the power spectral density measurements with normally distributed coefficients give good results for material classification, while the normalized time-domain measurements give better results for wear classification. Under laboratory conditions, this technique is shown to classify material and wear categories with F1 score above 0.85 out of 1.0 for our experiment. This technology could be used to assist operators in assessing material and wear conditions from a safer distance. It has applications in the coal mining industry as well as other applications which use conical picks such as road milling.

#### 5.2 Introduction

Operators monitoring important process feedback in hazardous regions is dangerous [20]. Operators are expected to monitor machine alignment, tool wear, machine condition, and the material being cut [21]. The hazards that the operators are exposed to in underground mining can be difficult to model [22]. To

allow operators to perform their role from a greater distance, we propose a sensor suitable for assisting operators in assessing material type and tool wear that integrates with conical picks on continuous miners used in underground coal mining.

Underground mining is dangerous and safety has not been improved over the last decade, with fatalities per 100,000 full time equivalent employees averaging 21.4 from 2011-2020 [23]. In particular, coal workers are roughly 50% more likely to be injured than workers in other mining sectors and account for roughly 50% of fatalities from 1983 to 2020[23]. Existing technologies for mitigating these hazards monitor the environment with micro-seismic sensors, distributed pressure sensors, or electromagnetic analysis [22]. These technologies only identify hazards after they occur. Elimination of hazardous conditions is the most effective method for reducing risk to workers in any application [24]. The only way to eliminate these hazardous conditions is to allow the operators to perform their role from a greater distance.

Previous efforts to allow operators to perform their role from a greater distance, namely development of remote controls, have allowed operators to collect better visual feedback; however, operators often put themselves in hazardous positions to do so [25]. Technologies also assist operators by automating some tasks. For example, automated hydraulic diagnostic systems can help operators monitor the machine's hydraulic conditions [26]. One of the most effective technologies for reducing worker injury is the personnel proximity detector, which disables certain machine operations if designated zones near the machine are entered by persons tracked with the device [27]. This device was implemented about a decade ago; however, there have not been any major improvements since.

Direct measurements of rock and pick interaction have previously noted significant differences in forces between tool wear levels [28, 29]. Material has been differentiated by vibration signatures using various classification techniques as early as 1993 [30]. Previous efforts for smart bit or intelligent pick tooling to perform these tasks in real-time during operation have taken place over the last few decades, examples include: using neural networks to classify tool wear in potash [31], using acoustic data to classify both material and tool wear in coal cutting [32], using piezo sensors to deduce rock chipping [33], and, most recently, using an instrumented block with integrated strain gauges to measure cutting forces [34]. So far, results using capacitive load cells have not been found for material and tool wear classification in underground mining. Advances in both capacitive sensing and vibration classification have unearthed a variety of applications in other domains. Our sensor, shown in Fig. Figure 5.1, can assist operators in assessing material type and tool wear by measuring differences in vibrational responses between the different conditions.

To test our sensor for material and wear classification, full-scale rock cutting experiments are performed using the linear cutting machine at Colorado School of Mines, a popular type of tool for rock cutting

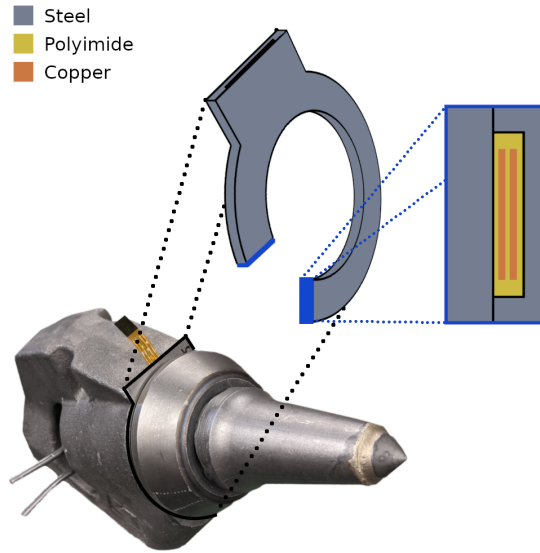


Figure 5.1 A prototype of the sensor integrated with the U92 4.0 22NB Conical Pick and K35 Block system, from Kennametal. The device is shown without the measurement collection system and is situated between the sleeve and the block. The FlexPCB interface is exposed, which provides access to the capacitive sensors' electrodes. A steel case protects the FlexPCB sensor and provides the necessary stiffness to transfer the input forces to the sensor. An embedded electronics platform, not shown in this figure, takes measurements suitable for dynamic classification of tool-wear and material. A cutaway of the sensor shows the thin film design for the force sensor.



Figure 5.2 The different pick wear levels. The *new*, *moderate*, and *worn* pick tips have spherical diameters of 3.71 mm, 17.9 mm, and 27.5 mm respectively. This approximates an even wear pattern. The *moderate* and *worn* tips were artificially worn using a lathe.

mechanics testing [35]. A limestone sample cast in concrete is used to test material classification. Conical picks of three different wear levels at an attack angle of 45 degrees are used for tool wear classification. The wear levels are *new*, *moderate*, and *worn*, where *moderate* represents a pick halfway through its useful life, and *worn* is a tool at the end of its useful life. The tool tips are artificially worn to a spherical diameter using a lathe to approximate an even wear pattern and for reproducibility. A closeup view of the tool tips and the values for their spherical diameters is shown in Fig. Figure 5.2. The low profile sensor sits between the sleeve and block. The sleeve has been machined down to a slip fit in the block to allow force transfer to the sensor. The sleeve and block are both retained by a large pin. Measurements are collected from the sensor using an embedded capacitance to digital converter and sent to a computer over USB.

To highlight the changes in vibrational modes, the data is transformed using short window fast Fourier transform preprocessing before classification. The resulting vectors are classified into material and wear categories using the support-vector machine technique. Data from strain gauges embedded in the linear cutting machine and our custom sensor are both used on their own for classification. Each classification system in our experiment is scored using the F1 score [36, 37]. The best performance for material and wear classification yielded F1 scores around 0.85 out of 1.0 for our experiment. Performance in tool wear classification is shown to be comparable between the custom sensor and the strain gauges embedded on the linear cutting machine. For material classification, the additional sensitivity due to the proximity of the custom sensor to the cutting interface allows it to perform better using the same algorithm.

The rest of this article is organized into sections. First, background information regarding material and wear classification algorithms is given along with a description of the algorithm we use. Then, the sensor design and characterization is described. After, the procedure for the rock cutting experiment is given, followed by the performance results of the classification algorithm. Finally, some discussion points and conclusions regarding the experiment and results are shared.

### 5.3 Material and Wear Classification

Material identification techniques for rock cutting can use metrics based in force and energy measurements, as different rock materials are known to require varying energy to break down [38, 39]. For tool wear classification, force or vibration feedback is commonly used in other domains such as metal milling or oil drilling because changes in tool mass and geometry cause the vibrational modes to shift [40–43]. Both material and tool wear classification can be framed as a vibration classification problems. Vibration classification lends itself towards certain standard signal processing and classification techniques, primarily with frequency domain preprocessing [44].

Preprocessing the input sensor data using different spectral or statistics based methods to improve classification results is popular [42, 43, 45, 46]. For this research, the fast Fourier transform is chosen as the preprocessing technique as it has been shown to give good results in many domains [47]. Depending on the chosen kernel for the support-vector machine, data standardization can range from beneficial to necessary, as the kernel may be built with assumptions on data mean values and range. The effects of the chosen normalization and preprocessing methods, or their absence, on the classification results are explored in this work.

The classification technique used after preprocessing is the support-vector machine (SVM) using the default ‘C-Support Vector Classification’ implementation in the Python library Scikit Learn [48], [49]. SVM has long been known to be able to classify model behaviors [50]. It has also shown useful specifically

in tool monitoring [51]. In general, the SVM works by finding a hyperplane in the data set which separates the data into the prescribed categories then, this hyperplane can be used as a quick decision rule for classification of future inputs [48]. The advantage of the SVM is it first transforms the input data to a higher dimension using a kernel function which helps to separate the data. This method has few hyperparameters and is considered generalizable, only needing relatively little training data to achieve good performance.

The SVM technique has few hyperparameters when compared to other machine learning techniques like feed-forward or convolutional neural networks, which allows it to be implemented quickly and be generalizable. The SVM is also typically better performing than simple techniques like k-nearest neighbors. K-nearest neighbors is another popular and low hyperparameter technique for vibration classification, and it works by selecting the majority class of the ‘ $k$ ’ samples closest to the input in its memorized training data [52]. The SVM solves the classification problem in a similar way, but reduces the training data for computational efficiency and better sensitivity to general trends. More advanced techniques, such as feed-forward or convolutional neural networks, are flexible techniques for vibration classification that work by numerically optimizing a series of weighted vector functions to approximate the statistical likelihood of a given input being from each output class based on the training data [53]. SVM strikes a balance between these techniques as it generally has better performance than k-nearest neighbors but is not as prone to over-fitting as the feed-forward or convolutional neural network.

### 5.3.1 Classification Methods

Time-series measurements are recorded from the four channels of our custom sensor and the four channels of the strain gauges on the linear cutting machine. For either sensor, we denote these measurements as  $CH_x[n]$ , where  $x$  is the channel index ranging from 1 to 4 and  $n$  is the sample index ranging from 1 to  $T$ , the total number of measurements. These time-series measurements from each sensor are then chopped into small segments representing short duration ( $\leq 0.25$  s) windows of signal. These discrete vectors are preprocessed to form the feature vectors to be classified by the support-vector machine. For an individual classification sample, the data from a particular channel can be denoted as

$\overrightarrow{C_{kx}} = [CH_x[k], CH_x[k+1], \dots, CH_x[k+M-1]]^\top$ , where  $k$  is the index corresponding to the start time of the sample window,  $x$  is again the channel index,  $M$  is the number of samples in the window, and  $[\cdot]^\top$  represents the matrix transpose operation.

Both window overlap and window size are varied during our tests to observe their effects on performance. Increasing window overlap generates more data vectors for training and testing, but the resulting samples are more redundant than those generated with less overlap. Increasing window size gives

data with more features which can improve classification accuracy. The classification rate is limited to one classification per window, and windows may overlap to increase the rate. A short window which gives acceptable performance is desired for rapid classification suitable for real-time use.

Each point in time can be assigned a class label for both material and wear. Only windows with contiguous labels are used in the experiment. Samples which are near the beginning or end of a material are discarded, as they do not have a clear ground truth label and are not representative of the steady state cutting dynamics. Separate classification systems are trained to identify material and wear. For an individual classification experiment, the set of paired measurement and class data is split randomly into testing and training sets. The set with the training indices is denoted in this work as  $R$ , while the set of testing indices is  $Q$ . After being windowed and split, the feature vectors for classification via support-vector machine are represented as:

$$\vec{X}_i = \mathcal{P}_\theta \left( \begin{bmatrix} \vec{C}_{k1} \\ \vec{C}_{k2} \\ \vec{C}_{k3} \\ \vec{C}_{k4} \end{bmatrix} \right), \quad (5.1)$$

were  $\mathcal{P}$  is the preprocessing pipeline for the data and  $\theta$  are the parameters fit from the samples in the training set. The subscript,  $i$ , is the sample index and ranges from 1 to  $N$ , the total number of vectors in the data set. The specific mapping between  $i$  and  $k$  depends on the window parameters. The Scikit ‘sklearn’ library [48, 49] provides a convenient data structure, the Pipeline object, which encapsulates these steps for consistent application and ensures that data from the testing set is not used during parameter fitting.

Table 5.1 Preprocessing Pipeline Steps,  $\|\cdot\|$ ,  $\cdot^2$ , and  $\sqrt{\cdot}$  are element-wise absolute value, square, and square root respectively.

Symbol	Values	Description
$\mathcal{N}_\theta^1, \mathcal{N}_\theta^2$	StandardScaler	$\mathcal{N}(\vec{X}_i) = (\vec{X}_i - \text{mean}(\vec{X}_i)) / \text{std}(\vec{X}_i)$
	None/Control	$\mathcal{N}(\vec{X}_i) = \vec{X}_i$
$\mathcal{F}$	FFTMag	$\mathcal{F}(\vec{X}_i) = [\ FFT(\vec{C}_{k1})\ , \dots, \ FFT(\vec{C}_{k4})\ ]^\top$
	FFTSQ	$\mathcal{F}(\vec{X}_i) = [FFTMag(\vec{X}_i)]^2$
	FFTSQRT	$\mathcal{F}(\vec{X}_i) = \sqrt{FFTMag(\vec{X}_i)}$
	None/Control	$\mathcal{F}(\vec{X}_i) = \vec{X}_i$

For our experiment, the pipeline consists of the composition of three optional operations, detailed in Table 5.1, and discussed here:

$$\mathcal{P}_\theta = \mathcal{N}_\theta^2 \circ \mathcal{F} \circ \mathcal{N}_\theta^1 \quad (5.2)$$

where  $\circ$  represents the function composition operator. The steps denoted with  $\mathcal{N}$  are normalization steps which transform the input data to be zero mean and unit variance along each feature using the sample mean and variance from the training set. The  $\mathcal{F}$  operation is the frequency based transform, and different variations of the fast Fourier transform are used. Every combination of processing steps is used, and the results are compared to determine the best methods for this application. Each step is also substituted with the identity function during this process as a control.

In addition to the preprocessing step, the support-vector machine also can apply a transform to the input data during its use. A description of the support-vector machine algorithm, adapted from [54] is given here. Intuitively, the support-vector machine finds a hyperplane between two sets of data. This is done efficiently by representing the hyperplane as a linear combination of a subset of the training data. These vectors from the training data are known as the support vectors. The binary classification support-vector machine works by solving the primal problem:

$$\min_{w,b,\xi} \quad \frac{1}{2} \|w\|^2 + C \sum_{i \in R} \xi_i, \quad (5.3)$$

$$\text{s.t.} \quad y_i [w^\top \phi(\vec{X}_i) + b] \geq 1 - \xi_i, \quad \forall i \in R. \quad (5.4)$$

$$\xi_i \geq 0, \quad \forall i \in R. \quad (5.5)$$

where  $w$  and  $b$  are the vector and offset representing the decision boundary hyperplane,  $\xi_i$  are slack variables which allow for error in classification in case of an infeasible problem. The  $y_i$  are binary class labels with value -1 or 1,  $C$  is a regularization parameter, and  $\phi(\cdot)$  is an implicit function which transforms the feature vectors into a higher dimension before separation with the hyperplane. The function  $\phi(\cdot)$  is implicit because in practice the dual of the primal problem is solved and only the inner product of the transformed input vectors is computed. This is done with the ‘kernel trick’, whereby a kernel function,  $K(x, y) = \langle \phi(x), \phi(y) \rangle$  is used, which is less costly to compute than the full inner product in the higher dimension. After solving the dual problem, the decision function for an unseen sample,  $\mathbf{x}$  is given by:

$$y_{pred}(\mathbf{x}) = \text{sgn} \left( \sum_{i \in S} \alpha_i y_i K(\vec{X}_i, \mathbf{x}) + b \right), \quad (5.6)$$

where the  $\alpha_i$  are the new coefficients given from the dual formulation and  $S$  is the set of support-vector indices. It is noteworthy that the final decision function does not explicitly use the hyperplane as represented by  $w$ , but instead relies the offset variable  $b$  and dot products (through the kernel) with the training data. To use the support-vector machine for multi-class problems, the chosen implementation uses a ‘one-vs-one’ voting scheme where a binary classifier is trained for each pair of class combinations. The class with the lowest index and most votes is chosen as the output.

The radial basis function is a popular kernel choice, as it was one of the first to be developed. It is similar in function and performance to using auto-correlation as the implicit function [55]. Since the radial basis function gave acceptable performance and to limit the number of hyperparameters, only it is used for this study.

To test our classification system, the feature vectors are sorted into testing and training sets using ratios of 25:75, 50:50, 75:25. Each split is done randomly, 100 times, for each combination of preprocessing parameters. Hyperparameters for our method are window duration, window overlap ratio, and window shape. Window duration is set to 0.05, 0.10, 0.15, 0.20 and 0.25 seconds, while overlap ratio is set to 0.25, 0.50, and 0.75. The window shape is left as rectangular for the entire study. Ringing effects from frequency convolution with the  $\text{sinc}(\cdot)$  shape of the window in the frequency domain will be applied consistency across samples. Discovery of the optimal window shape would require it’s own extensive hyperparameter study across the many popular window functions. To limit the scope of the study, and since adequate performance was given with the rectangular window, focus is given to the other hyperparameters.

The effect of the preprocessing steps or their absence is investigated for this classification system across the hyperparameters of window size and overlap. Each classification setup is scored using the F1 score [36, 37] which is the harmonic mean of the classifiers precision and recall:

$$F_1 = 2 \frac{\text{precision} \cdot \text{recall}}{\text{precision} + \text{recall}} \quad (5.7)$$

Precision is the ratio of positive classifications that are correct while recall is the ratio of positive samples which are correctly identified [37]. The F1 score provides a numeric value between zero and one, with one being a perfect score. For our multi-class problem, we train the SVM using the ‘balanced’ strategy where classes are given equal weight, regardless of class samples size, by setting regularization term,  $C$ , inversely proportional to the class frequency in the input data. We score the classifier using ‘macro’ averaging for the F1 score where the final score is the unweighted average of the F1 scores for each class. Using this setup, the classifier is trained to give equal weight to each class type, regardless of population size, and classification performance and is scored with a metric which also gives equal weight classifier performance

for each class. Additionally, confusion matrices and accuracy measurements are used to get a more complete sense of classifier performance.

From this study, the optimal subset of steps may be found in a verifiable way. The training and testing computations are performed on the Isengard supercomputer at Colorado School of Mines. Individual classifiers can be trained on a consumer laptop in less than a minute, but to run the thousands of tests for this study in a batch manner, the supercomputer is more appropriate. For each set of parameters, the mean and standard deviation of the F1 scores are recorded for a population of 100 experiments with different random splits of data. Setups giving scores with large deviations or high dependence on the test and train ratio are suspect for overfitting to non-relevant features in the data set, while a low deviation with a high mean F1 score that is similar across test and train ratios can be considered generalizable and useful for the target application. To meaningfully compare distributions of scores generated for each method, the Welch-Satterthwaite method (Welch's t-test) is used to determine if differences are significant [56]

### 5.3.2 Sensor Design Literature Review

When it comes to designing a sensor for underground mining applications, there are several key constraints: the device must be low power, low cost, and highly durable. Capacitive sensors generally meet these requirements. Sensors that are not considered directly for this study are Inertial Measurement Units (IMUs) or custom microelectromechanical systems (MEMS) devices due to their power consumption, cost, and fragility. The most promising fabrication technology found during our literature review was capacitive load cells embedded in flexible printed circuit boards. The sensor dynamics can be non-linear, so the collected measurements are compared to those of a linear force sensor.

Capacitive pressure sensor designs have used steel enclosures [57], film dielectric [58], and sensors made directly from flexible circuits [59]. Larger film dielectrics can be modeled with a general system of springs and dampers; however, with thin films only a few dozen  $\mu\text{m}$  thick, the molecular dynamics contribute greatly to the response [60] and make it non-linear. Encasing the flexible circuit element in an enclosure provides a rigid structure with more linear deformation, but the dielectric still affects the relationship between the input force and the measured capacitance. These flexible sensors are low in cost, while sensors which provide more linear measurements normally employ careful manufacturing processes, air gap designs, and different signal processing techniques such as those seen in [61–65]. Sensors which use thin films with non-linear deformation must use appropriate models and algorithms to achieve the desired classification results.

Popular flexible dielectric materials like carbon-doped thermoplastic poly-urethane and silicone can exhibit non-linearity through hysteresis, viscoelastic effects, or measurement creep [66–69]. The choice of

dielectric material for a capacitive sensor will influence much of its performance, so it is important that the material have robust properties for the expected range of conditions. Polyimide is a notable flexible dielectric material and sensor substrate for capacitive sensors due to its high temperature range, solvent resistance, and low surface roughness [70]. It is also easily integrated with electronic circuits boards, known as flexible printed circuit boards, where it serves as the substrate for conductive traces. However, when used in a thin film, polyimide has nonlinear deformation dynamics due to the complex molecular interactions of the constituent polymer chains [71]. This viscoelastic-plastic behavior can be difficult to model for a large range of input, with models either incorporating complicated numerical integration techniques [72, 73], only capturing the linear viscoelastic portion for small ranges [74], or ignoring the unloading phase [75]. Thicker films generally have a greater linear range [76] and most models incorporate some mix of viscoelastic and viscoplastic elements like the model seen in [77].

Other works which have used polyimide as the force or pressure sensor dielectric show mixed results for sensor performance. In one study, electrospun polyimide nanofibers were used as the dielectric to achieve measurement repeatability and sensitivity [78]. When the device was cycled from 0 to 10 % change in nominal capacitance for 10,000 cycles, no noticeable measurement creep was observed. In another study, spin coated polyimide was used, and the sensor response was much noisier and subject to some initial transient effects [79]. Another group used a FlexPCB force sensor encased in polymeric materials and it showed good linearity and low hysteresis for 1% changes in capacitance [80]. These studies indicate that polyimide is a good low-cost material choice that can still give good performance.

### 5.3.3 Sensor Design

To design a capacitive force sensor for material and wear classification, suitable choices must be made for materials, geometry, and the balance between sensor accuracy and bandwidth. Based on the sensor design literature review, a steel case with a load cell embedded in a flexible polyimide circuit board is chosen for the design. The steel is 303 series stainless, chosen to reduce potential for corrosion and for its resistance to fatigue. The steel case is made by chemical etching of 0.036 inch steel plates. A channel of 0.018 inch depth is formed on one plate and the two are laser welded together after a steel shim and the sensing membrane have been put in place. As noted in the prior section, polyimide is chosen for the sensing membrane for its wide range of operating conditions and robust properties. The sensor case geometry is largely determined by the target tooling, but must still be tuned to the operational requirements of the sensor. Likewise, the balance between sensor accuracy and bandwidth must be tuned to achieve the desired results.

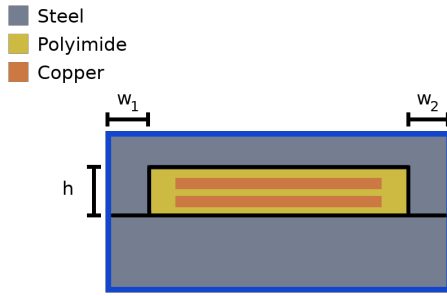


Figure 5.3 A cutaway of the sensor with the geometric parameters shown. The dimensions of the walls may be tuned to give the sensor the appropriate stiffness. The thickness of the top and bottom plates do not significantly influence the overall stiffness of the device.

To tune the case geometry for the desired stiffness, appropriate values must be chosen for the thickness and height of the side walls. These values are shown as  $h$ ,  $w_1$  and  $w_2$  in Fig. Figure 5.3. The donut shaped sensor has a center filled with viscous polyimide. The thickness and height of the side walls chiefly determines the spring constant of the sensor. The polyimide is much more compliant than the surrounding steel, so the overall case deformation is not influenced by its deformation in a significant way. However, the capacitive cells are directly embedded in the polyimide, so the measurement is greatly influenced by its deformation.

The sensor is designed for a maximum expected force of 200 kN. This provides some margin above the expected forces, which can be in excess of 100 kN for hard rocks. The sensor case is tuned to have around 10% strain at maximum load, in this way material fatigue can be mitigated and the measured capacitance should be close to linear with dielectric deformation. The thickness and height of the side walls,  $h$ ,  $w_1$  and  $w_2$  are set to about two and a half millimeters. The deformation of the steel case is expected to be mostly linear within this range of deformation.

The balance between sensor accuracy and bandwidth is determined by the range of deformation of the sensor as well as the capacitance and resonant frequency of the sensing circuit. In general, larger capacitance values will provide greater accuracy at the cost of sensor bandwidth. For the chosen hardware, the effective number of bits for the measurement is proportional to the square of the measurement time. Larger capacitances take longer to settle but can make more accurate measurements.

Given the tool geometry, four cells are placed in the donut: two large and two small. For our parallel plate design, it is important that the electrodes receive even loading, otherwise the parallel plate approximation is no longer valid. The large cells are designed for a nominal capacitance of 541 pF and the

small cells are designed for a nominal capacitance of 412 pF. All four pads occupy about 50° and are spaced evenly around the donut. The larger cells have about 30% greater area.

Since we are focused on high-frequency vibration classification, sensor bandwidth is maximized while still providing sufficient resolution and accuracy for classification. At a rate of 400 samples per channel per second, and using a gain of 4, the embedded system is able to provide 128 levels for up to a 25% change in capacitance. At 10% max expected deformation, the max expected change in capacitance is also about 10%. The true deformation of the polyimide around the electrodes is nonlinear and must be characterized to make informed decisions with the resulting measurements.

#### 5.3.4 Sensor Characterization

The sensor was characterized using load frame testing. Five different load rates were applied to three separate sensors to achieve a max force of 200 kN momentarily before ramping back down at an equal rate. Linear sensors show symmetric behavior for such a test, but the sensor measurements for this test, shown in Fig. Figure 5.4, reveal that our sensor exhibits hysteresis and rate dependence for these loads. These effects can be expected from the previous literature regarding polyimide deformation [70–80], and they obscure the effect of the average force on the measurement. It can be seen that, as the loading rate increases, the traces converge. This implies that the sensor can still be used to detect the changes in the high frequency components of the response that are useful for vibration classification. The overall deformation of the sensor case during these same loads is shown in Fig. Figure 5.5, and the deformation is linear. This confirms that the nonlinear deformation is happening in the polyimide and suggests that this case could be used to house other sensing technologies that can transduce displacement to electrical signals.

### 5.4 Rock Cutting Experiment

To test the sensor for *in-situ* force signature capture, rock cutting experiments were performed using the Linear Cutting Machine in the Earth Mechanics Institute at the Colorado School of Mines. A limestone sample cast in concrete was cut using a conical pick on the instrumented block. Time series measurements were made with the custom sensor as well as strain gauges integrated with the test equipment. The measurements were cut into small intervals and used with the classification algorithms to build separate material and wear classifiers

To capture the capacitive measurements, a capacitance to digital converter made by Texas Instruments is used: the FDC2114. This device interfaces with a generic microcontroller over I2C, a popular circuit to circuit interface. The software used on the microcontroller is available on Github as well as the data-acquisition software which is ran on the host computer to collect the measurements. The software

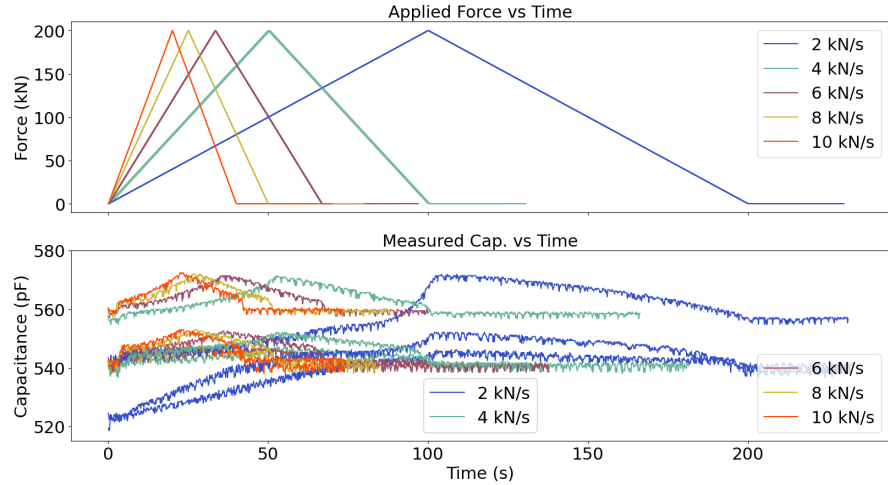


Figure 5.4 The triangular load profiles and the resulting measurements from the sensor. The sensor response is not symmetric and therefore non-linear. Lower load rates cause greater changes in displacement, which is consistent with previous studies for thin film polyimide.

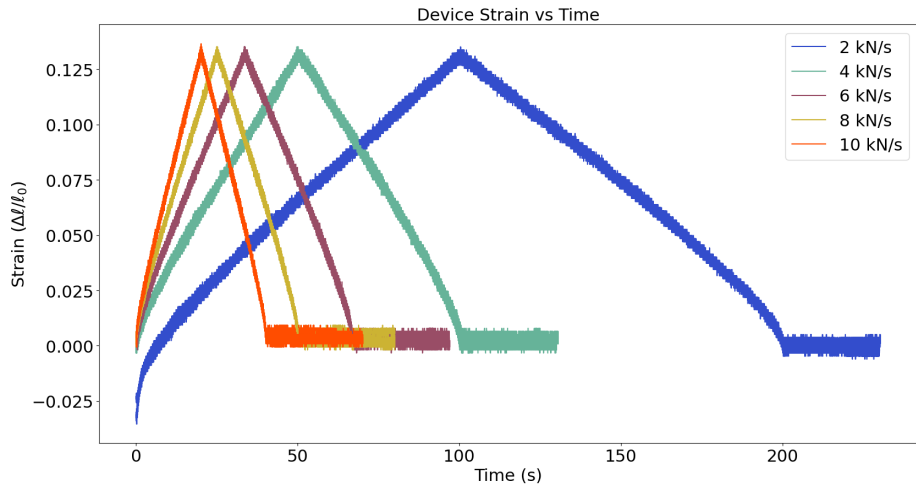


Figure 5.5 The case deformation during the load frame tests. The case deformation is symmetric for the loading and unloading phases, it also has a consistent slope for force over displacement. This means the case has approximately linear deformation for these load profiles.

that performs the classification experiment described in the previous section is also available. The microcontroller code is available here: <https://github.com/Fworg64/DAQQuery>. The data-acquisition code is available here: <https://github.com/Fworg64/reDAQ>. The machine learning and classification code is available here: [https://github.com/Fworg64/limestone\\_experiment](https://github.com/Fworg64/limestone_experiment).

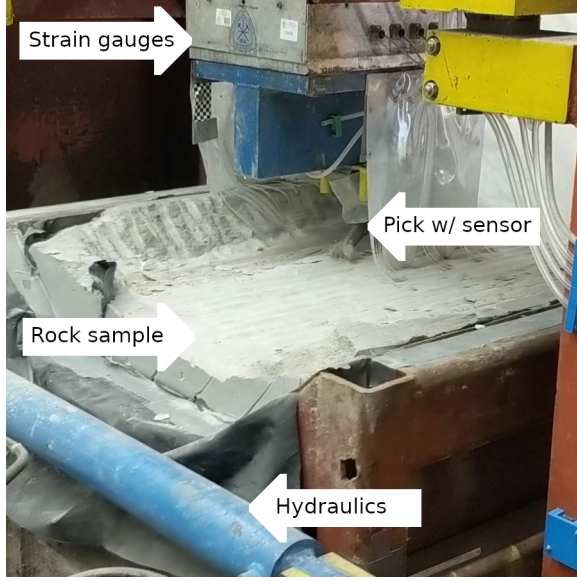


Figure 5.6 The Linear Cutting Machine in action. Hydraulic actuators push the sample into the cutting tool while the custom sensor and the embedded strain gauges record measurements. The tool is normally surrounded by the plastic curtain to aid in capturing dust for a simultaneous study of the effect of tool wear on dust generation.

The Linear Cutting Machine, shown in Fig. Figure 5.6, uses hydraulic actuators to drag the sample against the cutting tool. A cutting speed of 10 inches per second was used, which is relatively slow compared to the cutting speeds used in the field. The integrated strain gauges measure forces at a rate of 537.6 samples per second. The custom load cell makes measurements at a rate of 400 samples per second. The measurements from each sensor were recorded for use in the classification experiments. For applications with greater cutting speed and more materials, consider that rock fracture is largely static and machine vibration is dynamic. The frequency domain features associated with tool wear should scale with cutting speed and depend largely on the machine's natural modes, while those associated with material breakdown occur at much higher frequencies.

## 5.5 Classification Results

Using the method outlined in Section 2, the collected data is used to train and test the classification algorithm. The capacitive sensor data gave results similar to the linear sensor in tool wear classification. For material classification, the capacitive sensor generally performed better. The distribution of feature vectors, before being processed with the support-vector machine kernel, are shown for both sensors by material in Fig. Figure 5.8 and by tool wear in Fig. Figure 5.9. From these distributions, it can be seen that the capacitive sensor is much more sensitive to the higher frequency components of the interaction forces. This is likely a result of its closer proximity to the cutting interface. Typical measurements from

cutting experiments are shown in Fig. Figure 5.7.

For each sensor and application, five window sizes were tested. This gives ten pairs for comparison among each group of five, so we choose  $p < 0.01$  as statistically significant for differences in performance. The distributions of F1 scores for the classifiers with different window sizes are shown in Fig. Figure 5.10. For tool wear classification, performance was similar for all window sizes for both sensors. For material classification, the capacitive sensor gave measurements which could be more reliably classified. The differences in performance across window sizes are significant for material classification with either sensor.

Classification scores broken down by technique for the 0.2 second window size are shown in Fig. Figure 5.11. Trends in relative method performance were the same across window sizes. It was found that normalization after transformation, and not before, gave the best performance for the Fourier based methods. Also, the normalized time-series data with the SVM gave the best performance for tool wear classification in both the strain gauge and capacitive sensor cases. For material classification with the strain gauges, most methods gave similar performance. Normalization improved classification performance in nearly all categories.

Overall, tool wear in our data was classified with greater accuracy than material type. For tool wear, the normalized time domain data gave better classification results than the frequency data. For material type, only the capacitive sensor gave results that would be useful. The strain gauge data was classified with about 50% accuracy by the classifier. With the capacitive sensor classification of material type, performance using the frequency based data gave slightly better accuracy than the time domain data.

When using only 25% of the data for training, the classifier was still able to perform reliably using the capacitive sensor data. This shows that performance was not very dependent on the test and train ratio. F1 scores with standard deviations are given for the best setup for each application at different test and train ratios in Table Table 5.2. The scores do not change by a large magnitude, which indicates that the classifier is general and should perform well for larger data sets.

Individual confusion matrices are given for the 25:75 test and train ratio for material classification in Table Table 5.3 and for tool wear classification in Table Table 5.4. For these confusion matrices, rows represent the true class for the samples and columns represent the predicted class. Diagonal entries represent correct classifications, and each column is normalized to the number of predictions made of that class. The strain gauge material classifier has poor precision for concrete samples, as many of its concrete predictions are actually limestone samples. The F1 score is sensitive to this, and it is reflected in the much lower score. The accuracy of the strain gauge material classifier is around 80%, which is still useful. The accuracy of the capacitive sensor material classifier is higher, above 95%. This highlights the importance of using multiple metrics to accurately assess classifier performance.

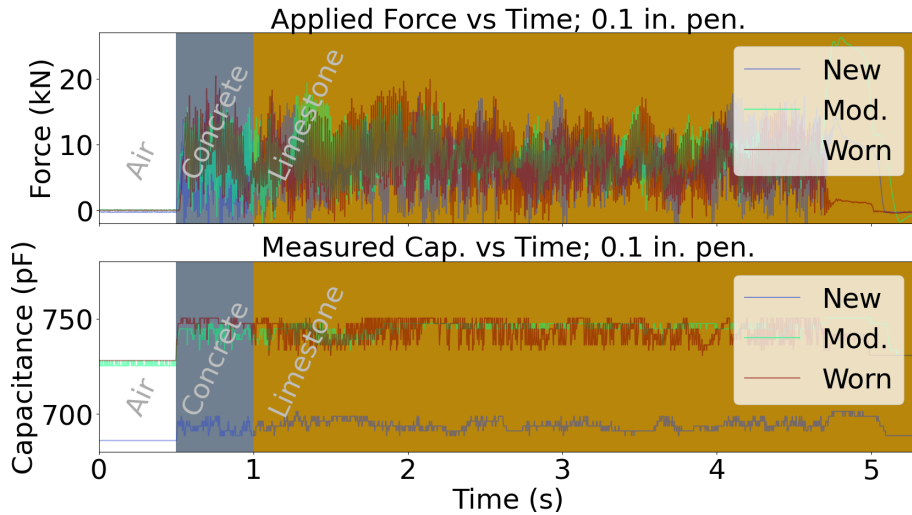


Figure 5.7 Measurements for typical rock cuts with different tool wear levels. The measurements from the linear sensors are shown in the top graph while the measurements from the custom sensor are shown below.

Table 5.2 Scoring metric and test/train ratios for each application

F1 Scores (mean $\pm$ std. dev., 100 trials)			Test and Train Ratio		
Application	Sensor	Best Config.	25:75	50:50	75:25
Tool Wear	Cap.	Time Domain	$0.971 \pm 0.003$	$0.965 \pm 0.003$	$0.950 \pm 0.004$
	SG	Time Domain	$0.955 \pm 0.005$	$0.947 \pm 0.004$	$0.934 \pm 0.004$
Material	Cap.	FFTMagSq	$0.924 \pm 0.053$	$0.902 \pm 0.044$	$0.831 \pm 0.085$
	SG	FFTMagRt	$0.533 \pm 0.045$	$0.536 \pm 0.026$	$0.534 \pm 0.016$

## 5.6 Discussion

Our sensor, as used in our experiment, shows promise as a method to objectively assess material type and tool wear. Under laboratory conditions, the sensor and classification scheme was able to detect differences in mode excitation caused by different materials and tool wears. For our experiment, the materials chosen were limestone and concrete. These materials are both much stronger than coal, but our experiment shows that they excite distinct modes in our cutting equipment. For tool wear, it is known that more worn tools can require several times the force to cut when compared to a new tool. The modes that are excited in the machine also change based on the changing tool geometry. For the target application of coal mining, coal is known to be much weaker than the material in which it is embedded, e.g. limestone. So, if our sensor is able to differentiate between concrete and limestone, it is postulated that it could differentiate between limestone and coal, which is much softer.

Using the Support-Vector Machine, the hyperplane between the measured datasets is found. This means that for a given input of discrete frequency or time samples, each value is multiplied by a coefficient

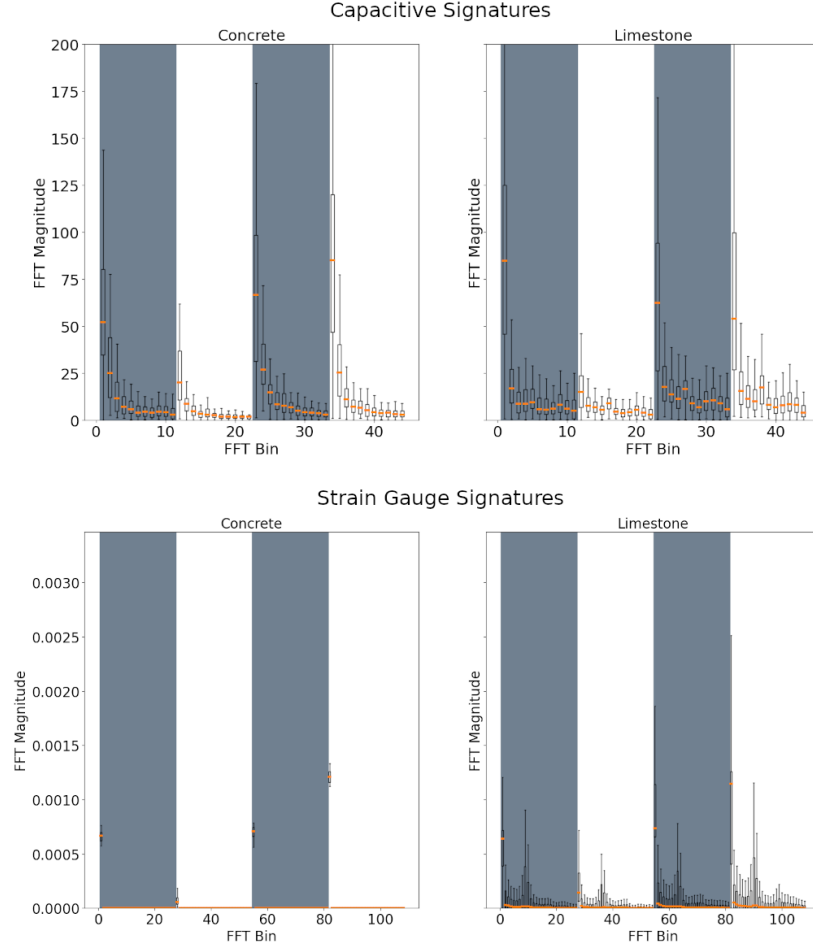


Figure 5.8 The frequency signature distributions collected from the custom sensor organized by material. The concrete material shows exponential decay after each primary mode, while the limestone has a more varied response. These differences can be used for classification of the signals by material.

and then combined to a single value, similar to a digital filter. The Support-Vector Machine has few hyperparameters, and the chosen measurements are shown to contain modal shifts that correspond with the categories of interest. The fundamental change in signal occurs as a mode distribution shift. This is readily detected by the Support-Vector machine.

To adapt our sensor to the target application, the target machine would need to be characterized in terms of dynamic modes. The sampling rate of the sensor system will need to be sufficiently higher than the primary modes of the target tooling, otherwise the measurements could be subject to aliasing. So long as the sampling rate at least satisfies the Nyquist criterion for the tool primary modes, aliasing should be minimized due to the high frequency attenuation caused by massive mechanical systems. Further, the

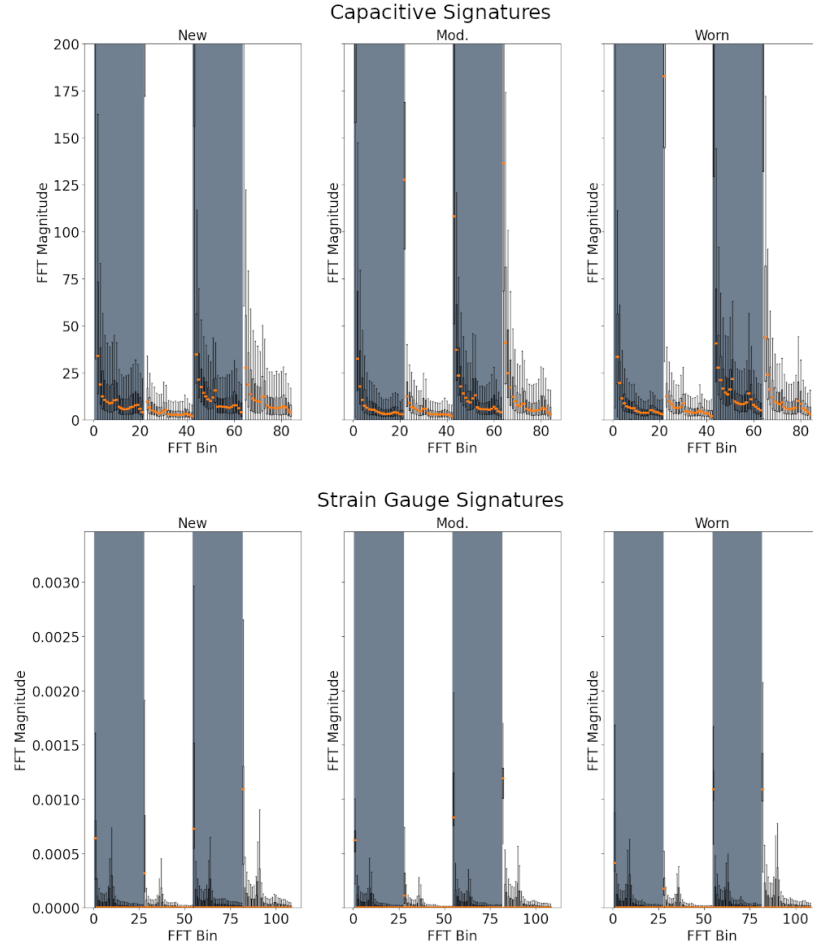


Figure 5.9 The frequency signature distributions collected from the custom sensor organized by tool wear. The New tool has a distinct response compared to the Moderate and Worn tools, and the energy in the higher modes generally increases with wear. These differences can be used for classification of the signals by tool wear.

viscous nature of the polyimide sensor provides even more damping, reducing the possibility for aliasing at the physical level.

Additional sensor designs such as an air-gap capacitive displacement sensor should also be investigated, as they could likely achieve more linear measurements at the cost of sensitivity. Development of a suitable power source and communication system must still be considered for this application. Other technologies such as acoustic sensors also show promise for material and wear classification, as they have been used with success in other domains and acoustic information is one of the primary feedback mechanisms currently employed by operators. A load cell based technology would likely be less susceptible to outside interference

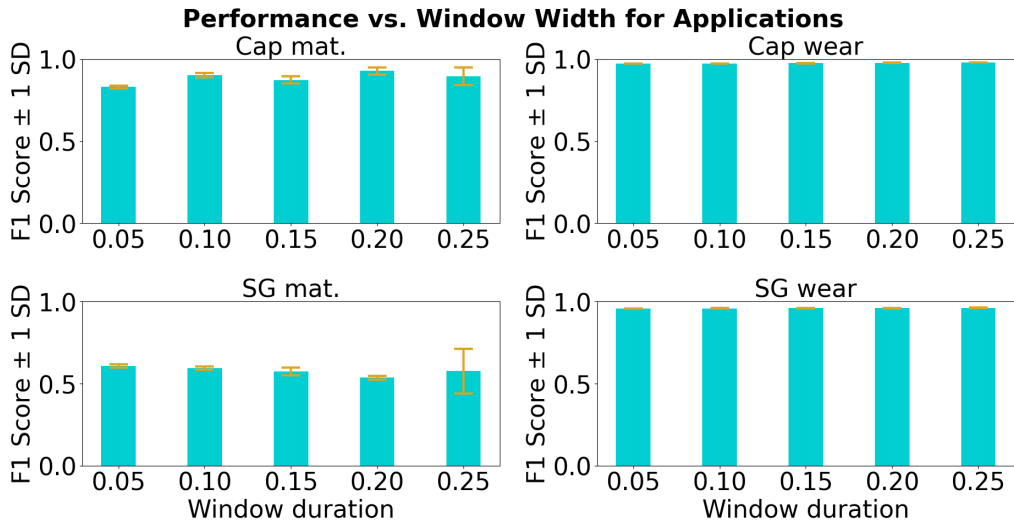


Figure 5.10 Bar chart with error bars for F1 score distributions by window size. For tool wear, both sensors were able to provide sufficient data for very accurate classification. For material classification, the capacitive sensor generally performed better than the strain gauge sensor. Some of the differences in performance are significant within the application and sensor combinations, but in general performance was similar across window sizes.

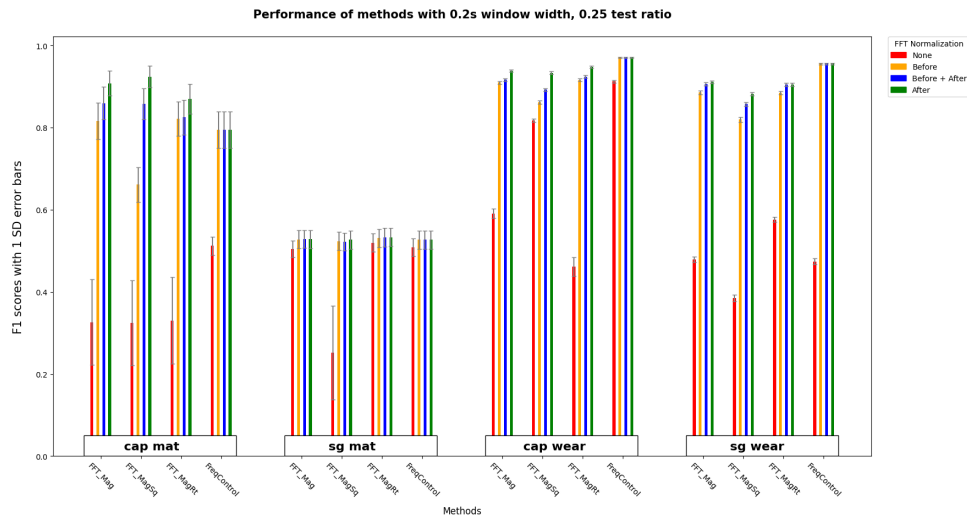


Figure 5.11 Performance of different preprocessing methods for each application. In general, normalization after transformation proved most effective for the frequency based techniques. Using the normalized time domain data was most effective for tool wear classification.

by unrelated signal when compared to an acoustic sensor, as it is closer to the mining interface and collects signal from a more narrow bandwidth.

Table 5.3 Confusion Matrix for Material Classifier; Normalized by prediction  
New Picks, 0.3 in Penetration, 0.2s Window, 50:50 test and train, PSD w/ post norm.

% Pred.	Strain Gauge Prediction		Cap. Prediction	
	Concrete	Limestone	Concrete	Limestone
Concrete	0.117	0.000	0.923	0.013
Limestone	0.883	1.000	0.077	0.987

Table 5.4 Confusion Matrix for Tool Wear Classifier; Normalized by prediction  
All Materials, All Penetrations, 0.2s Window, 50:50 test and train, Normalized Time Domain Data

% Pred.	Strain Gauge Prediction			Cap. Prediction		
	New	Mod.	Worn	New.	Mod.	Worn
New	0.983	0.105	0.000	1.000	0.000	0.000
Mod.	0.016	0.893	0.015	0.000	0.980	0.082
Worn	0.001	0.002	0.985	0.000	0.020	0.918

## 5.7 Conclusion

A sensor suitable for *in-situ* sensing of vibration signatures for material and wear classification was developed and tested for underground mining using conical picks. The classification accuracy achieved in the laboratory tests indicates that this is a promising technology for this application. The capacitive sensing design is low cost and low power due to its flexible circuit design. This technology could assist operators in material and wear classification by providing an objective measurement without requiring the operators to enter known hazardous regions near the machine and mining interface.

The capacitive load cell, to the authors knowledge, has not been used publicly for conical picks in rock cutting applications. This is a relatively new sensor technology that has been enabled by the steady advancement of capacitive sensor research over the last few decades. Existing solutions for hazard monitoring in underground coal mining primarily identify problems after they begin. Existing research in improving operator performance and safety has included acoustic classification systems and algorithms, strain-gauge based solutions, and piezo-electric sensors. By shifting the paradigm to predictive maintenance and more responsive control, operators are enabled to be safer and more efficient.

## 5.8 Disclosures

### 5.8.1 Conflicts of interests

On behalf of all authors, the corresponding author states that there is no conflict of interest. This work was funded by NIOSH Contract 75D30119C05413, “IMPROVING HEALTH AND SAFETY OF MINING OPERATIONS THROUGH DEVELOPMENT OF THE SMART BIT CONCEPT FOR AUTOMATION OF MECHANICAL ROCK EXCAVATION UNITS AND DUST MITIGATION”.

# CHAPTER 6

## TOOL WEAR CLASSIFICATION FOR CONICAL PICKS USING ACOUSTIC FOURIER SPECTRA MAGNITUDE

This article has been published open access and is part of the public domain. The copyright remains property of the author.

### **6.1 Abstract**

Underground coal mine workers who operate continuous mining machines rely on many cues to determine tool wear. This skill is difficult to train and proximity to the mining interface is a hazard to the machine operators. To create safer conditions for machine operators, an acoustic classification method for determining tool wear is proposed. To demonstrate this technique, a concrete sample is cut with conical picks of different wear levels using a linear cutting machine and the acoustic data is recorded for classification experiments. The differences in acoustic frequency spectra are highlighted and classification of short segments of the recorded acoustic data, less than 200 milliseconds in duration, is demonstrated using three popular classification techniques: the K-nearest neighbors classifier, the support-vector machine classifier, and the multi-layer perceptron classifier. The performance of these techniques is compared and the effects of segment size and downsampling are examined. Of the tested methods, the support-vector machine gives good performance with little complexity. This technology could aid operators in performing their roles from a safer distance, alerting them to worn tool conditions in real time.

### **6.2 Introduction**

Underground mining safety has not improved over the last decade, with the average annual rate of fatalities per 100,000 Full Time Equivalent (FTE) workers being roughly 24 from 2011 to 2022 [23]. In the literature review conducted by Sari et. al., it is noted that younger, less experienced miners are at greater risk of suffering a disabling injury [81]. On the other hand, for older and more experienced miners, the high levels and long duration of exposure to the hazards inevitably leads to problems like hearing loss [82], or other diseases such as black lung, a serious lung disease caused by exposure to coal dust, which can be fatal [83].

Some examples of dangers in the underground mine environment include: tunnel collapse, explosive gasses [84], high temperatures [85], exposure to diesel particulate [86], and the crush hazards caused by the machines used for the operation [87]. Machine operators in underground coal mines are particularly at risk, as they must remain near the cutting interface to pick up cues from machine and the environment to

monitor cutting conditions [88]. Workplace accidents caused by these hazards are problematic and they lead to loss of productivity, worker injury, and loss of life [89]. The National Institute for Occupational Safety and Health (NIOSH), recommends removing workers from hazardous locations as the best form of risk reduction in general [24].

Aiding operators with improved sensors for tool wear detection can help them perform their role from a greater distance to the cutting interface and reduce their risk from dust exposure as well as the from the immediate dangers at the cutting interface. Experienced operators are an invaluable resource, as they hold the experience gained after years of dealing with hazardous conditions [88]. Operators are known to rely on many cues, including visual, acoustic, and vibrational. This suggests a sensor can measure these cues.

Acoustic sensors can operate with a quick, less than one second, response time and detect changes in material type and tool wear in many domains [90–93]. When comparing acoustic, visual, and vibrational cues for tool wear, acoustic detection of tool wear has the advantage over visual detection in that it does not require a clear line of sight to the cutting interface, which is often in a hazardous location near the machine [88]. Alternatively, vibrational cues require direct contact with the cutting process, which requires a more robust sensor design compared to an acoustic sensor which is placed further away. For these reasons, using acoustic data for objective tool wear classification from a distance is investigated in this work.

Any technology that is employed in this domain must be well suited for the task it is designed to perform, or else its adoption is unlikely [87]. By providing objective, real-time data to human operators, the proposed technology can help operators make objective decisions regarding shutting down operations for cost-saving maintenance or continuing work. Automating tool wear detection can also allow machine operators to focus on other aspects of machine operation, increasing their productivity. Automation also enables the collection of data that could be analyzed for trends in tool wear during operation.

The rest of this article is outlined as follows. In the Background section, the application background and previous work used to guide this study are discussed. The Methods section follows, and it gives a detailed description of the experimental equipment, classification methods, and metrics for comparing classification performance. After that, the Results section lists the notable results. Then, a Discussion section is given, which states the merits of the tested methods and provides recommendations for implementation. Finally, a Conclusions section summarizes the work and its relevance considering the target application.

### 6.3 Background

In the black lung study by Colinent, the author notes that much effort has been given to dust mitigation. Strategies include: minimizing dust generation, preventing dust from circulating, removing dust from circulation, diluting dust concentration, use of barriers and ventilation direction to reduce worker

exposure, and maintenance of these systems [83]. The idea of removing workers from hazardous zones is supported by the general advice given by NIOSH in their hierarchy of controls [24]. In order to remove workers from the hazardous zones, they must be enabled to perform their roles from more remote locations.

Considering that experienced human operators can detect tool wear using acoustic cues suggests that enough relevant information can be captured within the typical human hearing range. A study on occupational hearing loss in underground mines reported that the type of hearing loss experienced by underground coal miners indicates a noise frequency below 6 kHz and a noise intensity around 90 dBA [82]. This work aims to capture these low-frequency and high-intensity acoustic emissions for classification.

As early as the 1990s, methods that consider the total volume of the acoustic emissions, the count of peaks and valleys in the signal, and the changes in signal spectra have been researched [94, 95]. Proper preprocessing is important. In underground mining, the rock-cutting system can lose mass as tools are worn, resulting in a non-stationary dynamic system. Fast Fourier transform based preprocessing of a small window of signal and subsequent classification with a support-vector machine has shown to be an effective method for robust classification of non-stationary dynamic systems [96].

Other preprocessing techniques for similar problems include wavelet and Empirical Mode Decomposition. Wavelet preprocessing combined with machine learning has been used with success in recent years [97–99]. Empirical Mode Decomposition has demonstrated vibration classification for tool wear in other domains [100–102]. We choose fast Fourier spectra magnitude based preprocessing and normalization for its time-invariant properties, small number of hyperparameters, and known effectiveness across domains [103, 104].

Both wavelets and Empirical Mode Decomposition are time-variant. The wavelet transform is known to be very sensitive to small-time translations [105]. With wavelets, this can be mitigated by measuring the average energy for a continuum of offsets and using those values as the feature vector for classification [106]. Similar processing would be needed for Empirical Mode Decomposition. Another option is to register the signal in the time domain to an event, such as contact with the material.

The choice of preprocessing methods is motivated by the idea that different tool wear levels in a conical pick will produce different acoustic emissions with different Fourier frequency spectra magnitude for a given material. This is verified by analyzing objective differences in statistical distributions of the frequency spectra magnitudes for the tested categories. To leverage these differences, different classification techniques are employed and compared. These methods and how they are compared are described in the next section.



Figure 6.1 The Linear Cutting Machine at the Earth Mechanics Institute of Colorado School of Mines.

#### 6.4 Materials and Methods

A homogeneous concrete sample is cut using the Linear Cutting Machine at the Earth Mechanics Institute at the Colorado School of Mines, shown in Fig. Figure 6.1, and capable of testing with many cutting tools [107]. Hydraulic actuators move the rock box for positioning and cutting. The rock sample in this experiment is a solid block of concrete. This is a homogeneous material that will isolate the changes in tool wear. Additional equipment consisting of a dust shroud and vacuum sample collection system was used for a simultaneous study on dust generation, but not for this study. Forces are recorded using integrated load cells in the coupling between the tool and the frame.

The acoustic signals for this experiment were recorded from the camcorder used to capture Fig. Figure 6.1 at a sample rate of 44.1 kHz. Then, the data is categorized by tool wear condition. The different tool wear levels are shown in Fig. Figure 6.2. The tool tips have been artificially worn with a lathe to a spherical shape to approximate even wear. They vary in diameter and have been chosen to represent *new*, *moderately used*, and *worn* tool tips. The *new* tool is unmodified and has a diameter of 3.71mm, the *moderately used* tool has a diameter of 17.9mm, and the *worn* tool has a diameter of 27.5mm.

The sample is cut by layers, with each layer consisting of several lines spaced roughly three centimeters apart. The cutting speed is set to 10 inches per second and penetrations of 1.5 and 2.0 inches are used. For each wear category, four lines are collected for both penetrations. To reduce the edge effects of the experiment, like the differences in impulse response between the linear cutting machine and the sensor, the recording of each line is trimmed to 6 seconds, starting shortly after the bit hits the material. The data is chopped into small segments of 20, 40, 60, 80, 100, and 200 milliseconds in duration. The segments are

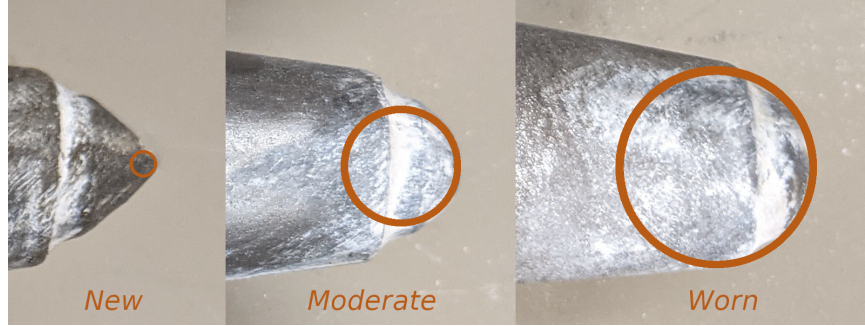


Figure 6.2 The tips of the conical picks with different wear levels used for the experiment.

allowed to overlap by 50%, and this yields roughly 480 samples for the 100-millisecond case and 4800 samples for the 20-millisecond case for each wear category.

The fast sampling rate of our microphone, 44.1 kHz, means that even short segments, dozens of milliseconds in duration, will have thousands of data points. Reducing input dimension via downsampling after low pass filtering will preserve low frequency data while leading to faster processing for the classification algorithms and eliminating additional aliasing. These segments also have a Hamming window applied to enforce periodic assumptions of the Fourier based preprocessing [108]. Longer signal windows will yield more resolution in the frequency domain up to the sampling frequency while higher sampling rates offer slightly increased resolution but over a wider frequency range. This study compares the effect on classification performance from both downsampling and window length.

Method performance is rated using the F1 score, which penalizes false positives and false negatives, by generating a distribution of scores and comparing the distributions [109]. The confusion matrices of the classifiers are also examined to understand how the classifier is performing [110]. Each window size data set is divided randomly in a 70:30 test train split 40 times to collect statistical distributions of the scores for each classification method when using a small sample for training data. The preprocessing and classification methods are described in more detail below.

## 6.5 Preprocessing

After filtering, downsampling, and splitting the data into small segments, the input to each of the classification algorithms is a vector of floating point numbers which represents a small segment of the audio recording from the cutting experiment. Any segment of the data, starting at time  $t$ , is denoted as  $\vec{x}_t$ . This vector has consecutive samples of the time domain signal starting at time  $t$  and ending at the end of the window duration offset by the start time. The first preprocessing step is to multiply this vector element-wise with a Hamming window,  $\vec{h}$ , and the new vector is given as:  $\vec{y}_t = \vec{h} \circ \vec{x}_t$ . The exact choice of

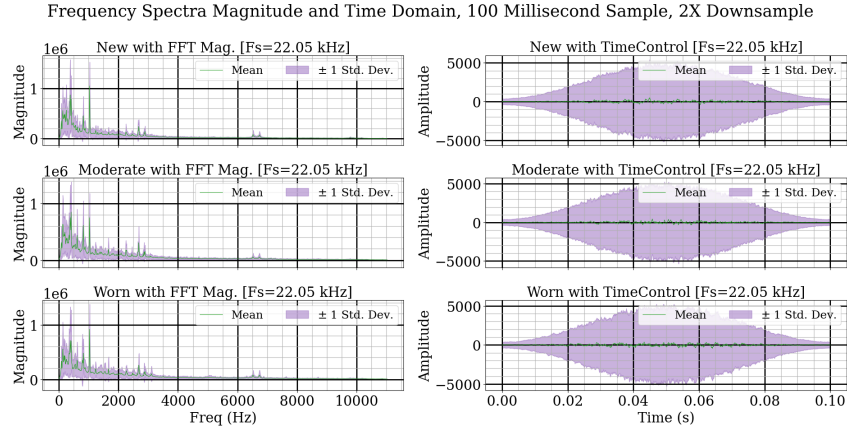


Figure 6.3 The natural distribution of frequency spectra magnitude and time domain data of each wear category for collected data.

window function has subtle effects on the algorithm performance, but in general the window function serves to reduce spectral leakage, or aliasing [111].

After the window is applied, the Fourier based preprocessing begins. The datasets are split 70:30 into the test and train sets. The normalized data is denoted as  $\vec{z}_t$ , and it is calculated as:

$$\vec{z}_t = (\vec{y}_t - \vec{u}) / \vec{s}, \quad (6.1)$$

where both subtraction and division are performed element-wise,  $\vec{u}$  represents the vector of mean values for each dimension in the training set, and  $\vec{s}$  represents the vector of standard deviations for each dimension in the training set. The distributions of frequency spectra magnitudes and time domain waveforms for each wear category are shown in Fig. Figure 6.3. The Fourier transform data has most of its energy below 4 kHz. The higher frequency data has smaller variance compared to the lower frequency data. The time domain data is roughly shaped like the window function. Transforming the time domain data into the frequency domain highlights the changing modes between the categories. These differences in resonant frequencies are made more apparent after normalization. During each classification experiment, the test data is normalized according to the distribution of the training set.

Before invoking any classifiers, objective differences in acoustic spectra across wear categories can be shown by performing a classic two-sided Welch-Satterthwaite t-test on each frequency bin [112]. The results of this test and the normalized frequency spectra magnitude distributions for each wear category are shown in Fig. Figure 6.4. In the left column, the mean value and the standard error of the mean are shown for our collected data. In the right column, the results of a t-test for each bin for each pair of categories are shown. It is known that operators use acoustic signals to determine cutting conditions, and

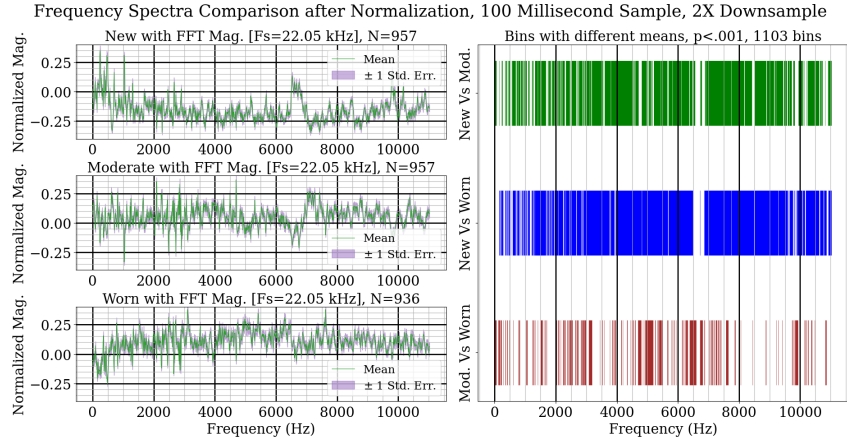


Figure 6.4 The mean frequency spectra magnitude after normalization for each wear category and a comparison between the categories for significant differences.

this figure demonstrates significant,  $p < 0.001$ , differences across tool wear categories for most frequency bins. Even though the higher frequencies have less energy, their differences are still significant due to their low variance. The exact changes will depend on the machine and the entire set of cutting conditions, but for a given environment, these differences can be observed and detected. The classification techniques discussed in the next section use these differences to determine the wear category of a given sample based on the training data.

## 6.6 Classification

These data splitting, preprocessing calculations, and classification techniques are computed using the scikit-learn, a.k.a. sklearn, library [113]. The library supports many classification and regression methods and facilitates rigorous comparison. For this study, the support-vector machine technique is compared with a more simple method and a more sophisticated method to investigate classifier efficiency. The more simple method is the k-nearest neighbors classifier. The k-nearest neighbor technique works by comparing the input sample to its memory of the k closest training samples, and the most popular class is elected as the output. The more sophisticated method, the multi-layer perceptron classifier, works by training a network of artificial neurons to develop a series of vector transformations which results in accurate classification. Meanwhile, the support-vector machine aims to find a separating hyperplane in a transformed version of the data.

To measure the performance of the chosen algorithms, the F1 score is used to evaluate the classification results. There is an inherent trade-off between precision and recall in practical classifiers [114]. The F1 score is the geometric average of precision and recall, and serves to evaluate overall performance. More

detailed descriptions of the individual classification algorithms follow below.

### 6.6.1 K-Nearest Neighbors

The non-parametric K-nearest neighbors approach is used in classification and regression [115]. The K-nearest neighbors classifier aims to predict the class label,  $g_t$  of future data point  $x_0$  on the predetermined  $q$  classes given a set of  $p$  labeled classes  $\{(x_t, g_t), t \in 1 \dots p\}$  [116]. In order to obtain the class label for  $x_0$ , the K-nearest neighbor (KNN) classification algorithm searches for the sample's K closest neighbors and then assigns the class of the majority. The selection of K and the distance measure used are the two factors that have the biggest impact on a KNN classifier's performance [117]. Without prior knowledge, Euclidean distances are typically used by the KNN classifier as the distance measure. These distances are simple to compute and if the data categories are distinct, than this method will work well. The Euclidean distance and  $K = 5$  are used for this study, with larger values of K giving similar results.

### 6.6.2 Support-Vector Machine

The fundamental goal of the support-vector machine (SVM) is to build a separation hyperplane that best divides data examples into two classes while maximizing the minimum distance between points and the separation hyperplane [118]. Support-vector machines employ the structural risk minimization [119] concept and seek to achieve zero misclassification error while reducing the model's complexity. The problem statement and solution of its dual via Karush-Kuhn-Tucker conditions [120] is omitted here for brevity. For discussion, the decision function of the two class support-vector machine is listed here:

$$h(x) = \text{sign} \left( \sum_{s=1}^p \beta_s g_s k(x_s, x) + r \right), \quad (6.2)$$

where sign returns 1 if the input is greater than zero,  $p$  is the number of support-vectors,  $\beta_s$  and  $g_s$  are weights, and  $k(x_s, x)$  is the kernel mapping of the support-vector  $x_s$  and the input,  $x$ , and  $r$  is a bias term. The kernel function is able to compare the input to the chosen support vectors in a space that highlights their differences.

The SVM is a binary classifier by nature, however many of the problems we are interested in tackling are multi-class ( $q$ -class) [121]. Hence a multi-class SVM approach must be adopted in that regard. In this study, a one-against-one approach [122] was employed. This approach trains  $q(q-1)$  binary classifiers to distinguish between two classes. The final output is the class that receives the most votes from the binary classifiers. The coefficients calculated during training are considered optimal for the given data. The SVM requires a roughly similar number of computations as the KNN, but takes extra steps to make the data more separable through the kernel function. The Radial-Basis function is used here for the kernel, as it can

make nonlinear separations.

### 6.6.3 Multi-layer Perceptron Classifier

A specific type of feed-forward artificial neural network is the multi-layer perceptron (MLP) and it is well-known for its stability, usability, and relatively modest structure in tackling some tasks when compared to other structures [123]. An MLP classifier analyzes the relationship between input and output in a set of p-labeled classes. An input layer, several hidden layers, and an output layer make up the network topology of MLP [124]. Processing nodes known as neurons make up each layer, with each neuron connected to all neurons in the previous layer.

Each neuron receives weighted inputs with a bias value, which are then transformed and processed by a nonlinear activation function [125]. The hidden layer's output is shown in the following:

$$s_r = t \left( \sum_{q=1}^p \omega_{qr} x_q + c_r \right), \quad \forall r \in \{1, \dots, k\}, \quad (6.3)$$

where the activation function is represented by  $t(\cdot)$ ; the bias of the  $r$ th hidden units is represented by  $c_r$ ; the inputs and weights between the input and hidden layer are represented by  $x_q$  and  $\omega_{qr}$ , while  $s_r$  is the hidden layer's output. Activation functions come in a variety of forms, including logistic sigmoid, softmax, hyperbolic tangent, and rectified linear unit functions [126]. The output layer consists of one neuron for each class, and the output is the probability that the input belongs to that neurons respective class.

The coefficients for the network are trained in an iterative fashion by examining the gradient of performance with respect to each one. This forward pass and back-propagation process is repeated until the network finds a solution or the necessary number of iterations have been completed [127]. This type of training requires a balance of many factors to be successful; but once trained, the network can classify samples with a roughly similar number of computations as the other techniques depending on the network size. The rectified linear unit activation function and a network of two hidden layers equal in size to the input dimension is used here, with more hidden layers giving similar results.

## 6.7 Results

The mean F1 scores are plotted against the window lengths for each of the tested methods at each of the tested downsampling factors. In the following figures, the F1 score of a method is significantly greater than another method if the median score is above the max score of the other method. This comparison method is slightly more conservative but more visually straightforward than comparing each score in the collected distribution, as recommended in [109]. Classifier performance was greater with longer window lengths and increased sampling rates, or lower downsampling factors.

The K-nearest neighbors classifier performance is shown in Fig. Figure 6.5. Using K=5 gave slightly better performance than other values, but this method performed the worst overall. Increasing window length gave better performance for this method, and downsampling had little effect for larger window lengths. The F1 score only increased a small amount when using the 0.2 second window compared to the 0.1 second window.

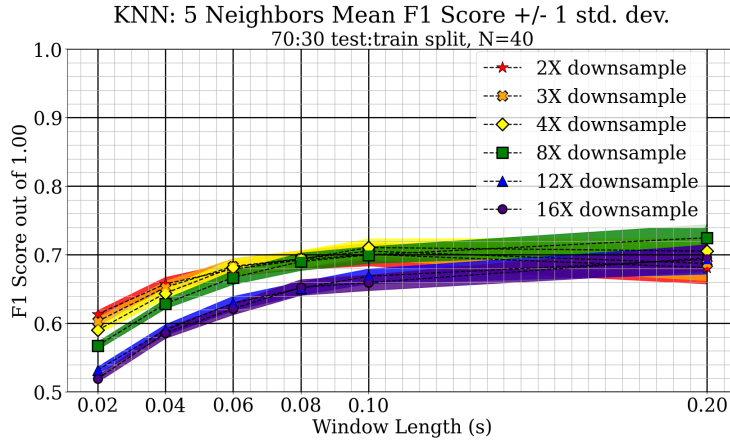


Figure 6.5 The mean F1 score and standard deviation for K-nearest neighbors method.

The support-vector machine classifier performance is shown in Fig. Figure 6.6. This is a low hyperparameter method that performs very well and does so efficiently. With this method, performance trends are better with longer window length and higher sampling rates, or less downsampling, for our experiment. Increasing window length gave a better performance for the number of variables introduced compared to increasing sampling rates. Using a window length of 0.2 seconds gave the best performance of for all downsampling levels, and the performance was similar for samples with less downsampling.

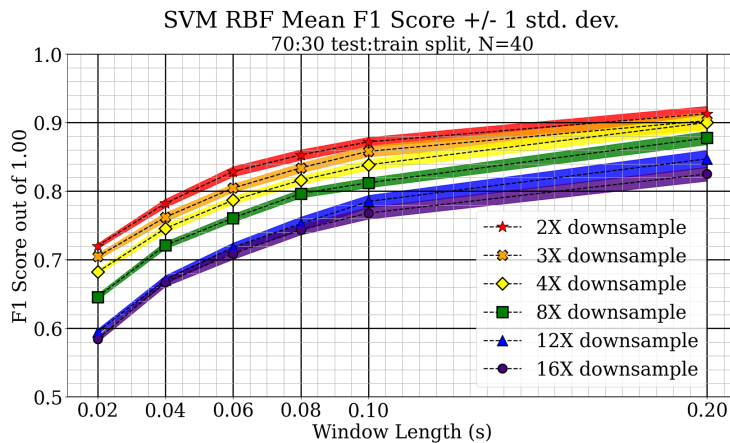


Figure 6.6 The mean F1 score and standard deviation for the tested support-vector machine method.

The multi-layer perceptron classifier performance is shown in Fig. Figure 6.7. This method has the power to classify data very accurately for samples similar to its training data. Different network sizes are tested to achieve maximum performance. This method scores similarly to the support-vector machine, but uses more resources. Both longer window lengths and higher sampling rates, or less downsampling, increased performance. Increasing window length gave better performance for the number of variables introduced compared to increasing sampling rates. Using a window length of 0.2 seconds gave the best performance of all downsampling levels, and the score tapered to about 0.90.

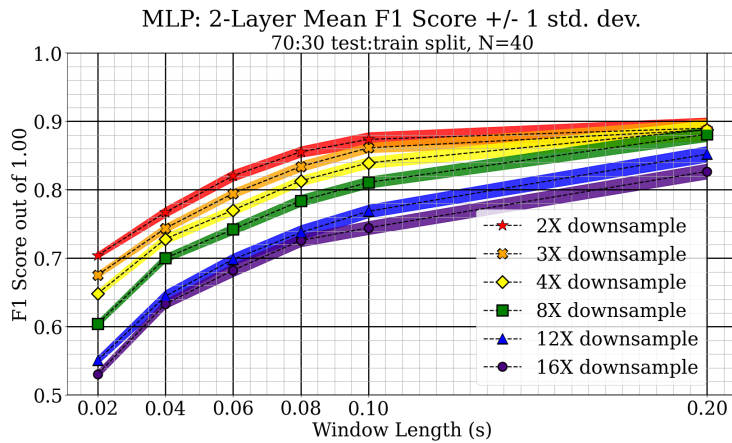


Figure 6.7 The mean F1 score and standard deviation for the tested multi-layer perceptron methods.

Looking at the confusion matrices for the different types of classifiers generally showed that most of the confusion was between the *moderate* and *worn* categories of bits, suggesting that these two categories have responses that are more similar to each other than to the *new* category. A sample confusion matrix for a SVM classifier experiment is shown in Table Table 6.1, it is representative of most of the other classifiers too. The table shows data, normalized by true class size, for the concrete sample using a 70:30 test train split and with fast Fourier transform preprocessing of a 100 millisecond window. The table shows that there is about twice as much confusion between *moderate* and *worn* categories as there is between *new* and the other two wear categories. This indicates that determining wear to a fine degree may be difficult with acoustic emissions alone.

Table 6.1 Confusion Matrix for Acoustic Wear Classifier, Normalized by True Class Size.

True Class	Test result %		
	<i>new</i>	<i>mod.</i>	<i>worn</i>
<i>new</i>	90.15	4.77	5.08
<i>mod.</i>	3.85	87.26	8.89
<i>worn</i>	5.67	9.25	85.07

## 6.8 Discussion

It is well known that changes in tool wear produce changes in vibrational response across many domains. This fact is also true in the case of underground mining. Human operators use sound cues as one of the means of assessing tool wear during operation. The operators have many duties, and this skill can be difficult to train, since the process is subjective. By providing operators a means to perform some of these duties from a safer position, their exposure to risks at the mining interface can be reduced [88]. This work proposes the addition of objective acoustic data collection and analysis to aid in tool wear classification.

When using methods like the ones described in this work, the cutting conditions must be taken into account. For example, cutting different materials can also produce different modal responses as well as cutting at different speeds, penetrations, and with different tool geometries. The operators ability to deduce changes in wear in different materials comes from experience in cutting those materials with tools at different wear levels. Likewise, to successfully apply this technique, data would need to be captured and analyzed for different cutting conditions.

When comparing the methods for implementation in the application, the support-vector machine would be an efficient classifier to use, as it scores as well as the multi-layer perceptron classifier, but has reduced computational complexity. The results also indicate that longer sample times, which give increased resolution for the sampled frequencies, provides better classification performance than using an increased sampling rate for a shorter duration considering the number of variables introduced.

With a window of 0.2 seconds, the tested sampling rates had similar performance. At this sample length, the input dimension is large, especially when little downsampling is used. Use of larger samples was computationally infeasible for the equipment in this study and also would also have reduced the number of samples available in the data set. The good performance of signals with long duration and downsampling implies that lower frequencies are of particular interest for tool wear classification in rock cutting. The code and data used for this work are available at: [https://github.com/Fworg64/concrete\\_tool\\_wear](https://github.com/Fworg64/concrete_tool_wear).

After classification, human operators could be alerted to the anomalous conditions to allow them to make a decision to either stop the operation for further diagnostics or continue cutting if they know from experience what could be causing a false positive or how long to extend the current operation. Also, this technology that can monitor tool wear in an objective manner would provide a mechanism to monitor the performance of human operators. This can help operators and other stakeholders identify areas where they can improve. It can also be used to assist in training and help to identify risky operation. Either way, the feedback could be collected from a greater distance, reducing the operators exposure to dust and other hazards.

To implement this technology, only a simple and low-cost microphone would need to be placed near the cutting interface to detect the mode shifts associated with changing tool wear. These devices are low power, low cost, and very portable, making them well suited for the mining environment. However, since the signal is only collected from one or maybe several points, it is unlikely that this technology could predict which tools are worn on the drum head. Also, interference from nearby operations which are producing noise could also affect the accuracy of this method were it to be deployed to an active mine. Ultimately, this technology could assist operators in performing their role from a greater distance and provide a level of objective feedback that is not currently present.

## 6.9 Conclusion

In this paper, we showed a method for classifying the different acoustic signals generated by conical picks of different wear levels cutting into a controlled concrete sample. The changes in tool mass and geometry lead to excitation of different modes, which can be detected and classified by the tested methods after appropriate preprocessing. Of the tested methods, the support-vector machine using long duration samples that are downsampled to an appropriate dimension, like 200 milliseconds and 4 times downsampling, performs well and is computationally efficient.

Acoustic emissions are currently processed by human operators with many duties. By automatically classifying the acoustic emissions, operators can be enabled to perform their role from a greater distance. This way they can avoid hearing damage, harmful dust, and machine proximity while being able to focus on their many other duties. With sufficient data collection, this classification can be performed with a microphone and an embedded processor.

## 6.10 Acknowledgments

Special thanks to AliseH and Tivali24 for contributions to the python code for running the experiments and displaying the data. Special thanks to Syd Slouka for helping run the experiments and to Carson Malpass for helping design mounts for acoustic sensors.

## 6.11 Declarations

### 6.11.1 Funding

This work was funded by NIOSH Contract 75D30119C05413, IMPROVING HEALTH AND SAFETY OF MINING OPERATIONS THROUGH DEVELOPMENT OF THE SMART BIT CONCEPT FOR AUTOMATION OF MECHANICAL ROCK EXCAVATION UNITS AND DUST MITIGATION.

#### **6.11.2 Conflict of interest**

The authors declare that there is no conflict of interest.

#### **6.11.3 Availability of data and materials**

The data used for this research is available publicly at:

[https://github.com/Fworg64/concrete\\_tool\\_wear](https://github.com/Fworg64/concrete_tool_wear)

#### **6.11.4 Code availability**

The code used for this research is available publicly at:

[https://github.com/Fworg64/concrete\\_tool\\_wear](https://github.com/Fworg64/concrete_tool_wear)

## CHAPTER 7

### CAPACITIVE LOAD CELLS FOR UNDERGROUND MINING FORCE SENSING APPLICATIONS

This article has been published open access and is part of the public domain. The copyright remains property of the author.

#### 7.1 Abstract

In underground coal mining, machine operators put themselves at risk when getting close to the machine or cutting face to observe the process. To improve safety and efficiency of machine operators, a cutting force sensor is proposed. A linear cutting machine is used to cut two separate coal samples cast in concrete with conical pick cutters to simulate mining with a continuous miner. Linear and neural network regression models are fit using 100 random 70:30 test:train splits. The normal force exceeds 60 kN during the rock cutting tests, and it is averaged using a low pass filter with a 10 Hertz cutoff frequency. The sensor is able to track the normal force on the conical picks with a mean absolute error less than 6 kilonewtons and an  $R^2$  score greater than 0.60 using a linear regression. A small neural network with a 2nd order polynomial expansion is able to improve this to a mean absolute error less than 4 kilonewtons and an  $R^2$  score around 0.80. Filtering measurements before regression fitting is explored. This type of sensor could allow operators to assess tool wear and material type using objective force measurements while maintaining a greater distance from the cutting interface. The graphical abstract, shown in Figure 7.1, is a visual aid for this abstract.

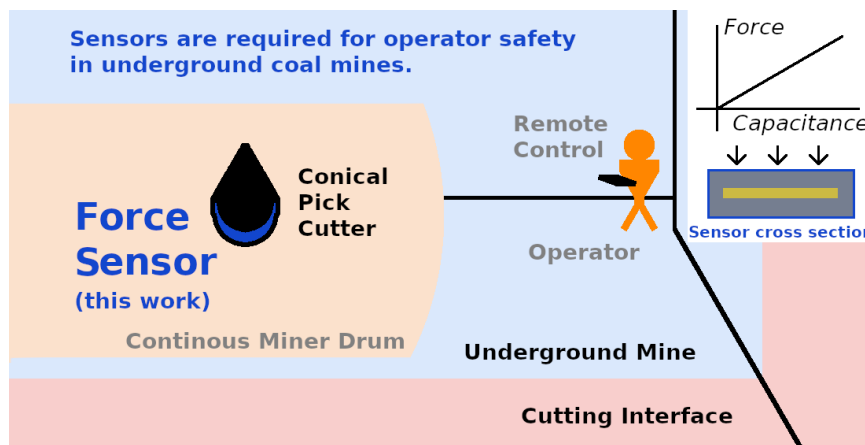


Figure 7.1 Graphical Abstract

## 7.2 Introduction

The health and safety of underground coal miners is affected by nearly every aspect of the operation [128]. The effects of these hazards are mitigated by proper ventilation and extraction planning [129]. Machine operators need feedback from the cutting interface to achieve the planned extraction [88], but the cutting interface is the source of harmful dust, gasses, and tunnel conditions. The proposed sensor can collect force data from individual conical picks at the cutting interface, providing operators more feedback while allowing them to maintain a greater distance.

In the U.S.A., employment in the coal mining sector has generally decreased since the 1970s boom, but experienced a brief renaissance during 2000-2010 [130]. Employment in coal mining in the U.S.A roughly halved over the period between 2010 to 2020 [131]. Allocation of resources that reduce accidents and increase mine output is the optimal trajectory for advancing technology in underground coal mining [13]. If worker supply continues to decline and regulations increase, boosted worker productivity will be needed to meet future demand for coal.

Coal is generally a soft rock and can be broken apart by the average set of human hands in small quantities. The rock in which coal is often deposited is much harder, and is cut by a continuous mining machine with a drum holding an array of conical picks. Specific energy of the cutting process has a strong correlation with material type and tool wear [132]. For this work, a sensor design that measures the forces present on the picks is chosen. These force measurements provide direct and objective feedback from the cutting process.

This work is the follow-up research for a previous sensor design, which used a much thinner membrane,  $25 \mu\text{m}$  thick, with non-linear deformation dynamics, between two electrodes [133]. Here, a design with a much thicker dielectric, with nominal thickness of  $240 \mu\text{m}$ , and a single conductive plate is tested. The force sensor fits under the sleeve of a conical picks, and can provide real time force feedback from the location of the tool. Operators must make decisions regarding tool changes and cutting strategies. This device would assist operators by providing measurements of the rock cutting forces present at each instrumented pick, allowing them to make decisions from more remote locations.

A proposed network topology for efficient use of the sensor in the underground mine, is shown in Fig. Figure 7.2. This figure shows multiple smart picks connected via CAN bus, which has been recognized as meeting the requirements for other underground coal mining applications [134, 135]. The data from the smart picks is aggregated and compressed by an edge processor on the drum, referred to as the drum processor. From the drum processor, data is both sent wirelessly to the operator in real time and to a central storage server, a.k.a. the cloud. The information could be displayed to the operator using a backlit

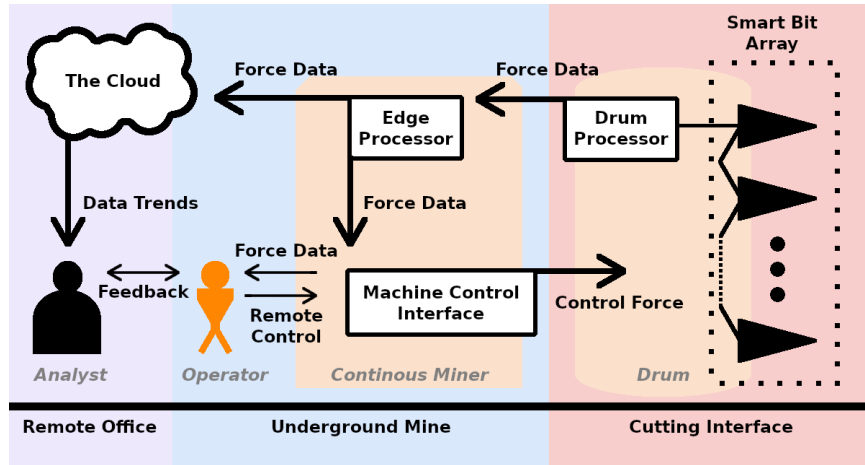


Figure 7.2 The network proposed for integrating our sensor with the continuous miner. Individual sensors can be linked to an edge processor on the drum which aggregates the force data via CAN bus, a robust interface for sensor networks. From the edge processor on the drum, labeled "Drum Processor", force data can be sent wirelessly to an edge processor on the machine chassis. There, the data can be parsed into a displayable format for immediate use by the machine operator and also sent up to the surface to be stored in a central server for processing by a mine analyst to gain insight into operator performance. The analyst and the operator can then communicate to increase efficiency and safety.

display on the remote controls for the machine. The data in the cloud can be analyzed to identify trends in production efficiency and safety.

Instrumenting each pick, or a representative subset, allows capture of cutter-head state, which is necessary for operators to make informed decisions regarding tool change scheduling and machine control. This setup also allows the human operator to make informed decisions using the collected feedback while staying in a safer position. This could aid in identifying if the tool force is much greater than expected, reducing incidences of operators approaching the machine to check tool wear.

This work focuses on the design of the force sensor at the cutting interface. When it comes to designing a force sensor for underground mining applications, several base designs and materials were considered. In general, rock cutting forces depend on the tool geometry and the material properties and they can range from dozens to hundreds of kN at each pick [136–139]. The operation of the mining equipment and the complicated network of jagged tunnels cause the environment to be noisy electromagnetically and acoustically [140–144]. The mining environment is also very harsh, and cutting tools can be consumed quickly, typically being consumed after clearing several cubic meters [145–147]. These conditions require any sensor to be robust and also low cost.

It has long been known in rock cutting that the specific energy of a material being removed is related to its strength when breaking down [132]. Also, when a conical pick wears down to a rounded shape, the specific energy of the cutting process increases, resulting in less cutting efficiency and higher forces [136].

In an underground coal mine, operators directly use many cues from the environment to determine tool wear levels and material types [88]. Objective feedback in the form of force measurements stands to improve operator efficiency.

Other methods, like vibro-acoustic signal processing, are gaining popularity for tool wear and material classification in domains like metal milling [148] and oil drilling [149]. Acoustic techniques can be susceptible to interference from nearby sources, but a force sensor on the pick will have a direct link to the cutting process. Many different technologies exist for detecting roof fall conditions [150–152]. The proposed technology would help mitigate unintentional roof damage by directly measuring cutting tool force and facilitating either operators or machine safety features to rapidly respond.

To measure forces in a tough environment with a low cost sensor, a capacitive sensor enclosed in a steel case with a polyimide dielectric is designed. The simple parallel plate approximation for the capacitive sensor is used:

$$C = \frac{\epsilon A}{d}, \quad (7.1)$$

where  $C$  is the resulting capacitance,  $\epsilon$  is the absolute permittivity of the dielectric,  $A$  is the area of overlap between the plates, and  $d$  is the distance between them [153]. Fringing effects are small compared to the nominal capacitance at the resting displacement [154]. The sensor is designed so force compresses the sensor, altering the  $d$  value in (7.1) [155, 156]. Other sensor designs involve co-planer electrodes [157–159], different dielectrics [160], or motion parallel to the plates [161–163]. This sensor is designed to be compressed normal to the plates for a robust design that can withstand the forces of rock cutting.

The sensor measurements would be collected and forwarded to operators wirelessly so they can make decisions with more information. Such a device would also be able to log measurements for later analysis and process optimization. The design and validation of a single smart bit sensor is the focus of this article. The rest of this article is organized as follows: The next section is the Materials and Methods section, which discusses the experimental setup, the regression techniques used for the empirical models, and the analytical modeling for the sensors. Then, the Results section shows data from the calibration and test procedures, sharing empirical values for sensitivity and comparisons of force predictions using the sensor measurements with measurements from the test equipment. Finally, a Discussion section mentions both benefits and drawback to the implementation while the Conclusion section shares potential impacts from this technology.

### 7.3 Materials and Methods

The sensor requirements for force sensing range, bandwidth, accuracy and resolution are chosen first. A force sensing range of 0 to 200 kN is targeted. For bandwidth, the tracking of average, rather than instantaneous, cutting force is of interest because tool wear and material type are known to change average cutting forces. Tracking high frequency changes in cutting force can be useful for classification of material type and tool wear, as shown in the previous work by the authors [133]. Using lower frequencies for regression de-emphasizes the differences in dynamics between the capacitive sensor and the test equipment sensors caused by their distance and individual designs by focusing on the average forces.

The regression target is chosen to be the drag force after it is filtered with a low pass filter with a 10 Hz cutoff frequency. Making the regression target an average lowers the variance that must be estimated. This relaxes the regression problem, but still gives a sensor with known accuracy and response time. The requirements for accuracy and resolution are not very stringent due to the large differences in forces that can be expected between distinct materials and wear conditions. In terms of mean absolute error, 15 kN or less would enable basic classification of material and wear conditions.



Figure 7.3 Two sensor prototypes. The one on the left has only been used for characterization in a load cell with controlled parameters. The one on the right has been through the same calibration as well as a controlled rock cutting experiment. During the rock cutting experiment, the air gap of the sensor is crushed out, altering the model but still giving a mostly linear sensor. The exposed sensor membrane was inadvertently cut by the edge of the second sample on the last cut. The walls of the sensor have retained much of their thickness, but they have deformed slightly to match the tooling.

Finished samples of the sensor design are shown in Fig. Figure 7.3. Two types of experiments are conducted with the sensor, load frame testing and rock cut testing. Both tests use the FDC2114 from Texas Instruments to record the capacitive data from each of the 4 channels at roughly 400 Hz. The load

frame test measures the sensor response to gentle load profiles in a controlled environment and the rock cut testing demonstrates use of the sensor for the application.

For the load frame testing, load profiles which ramp up to 200 kN then back down at rates of 2, 4, 6, 8 and 10 kN/s are applied. The relationship between the sensor measurements and the force and strain measurements from the load frame are examined. With this test, the sensor linearity can be measured and the noise can be characterized in a controlled environment. The sensitivity to normal force is measured with a linear regression. One of the samples is tested twice to characterize repeatability. The setup is shown in Fig. Figure 7.4.

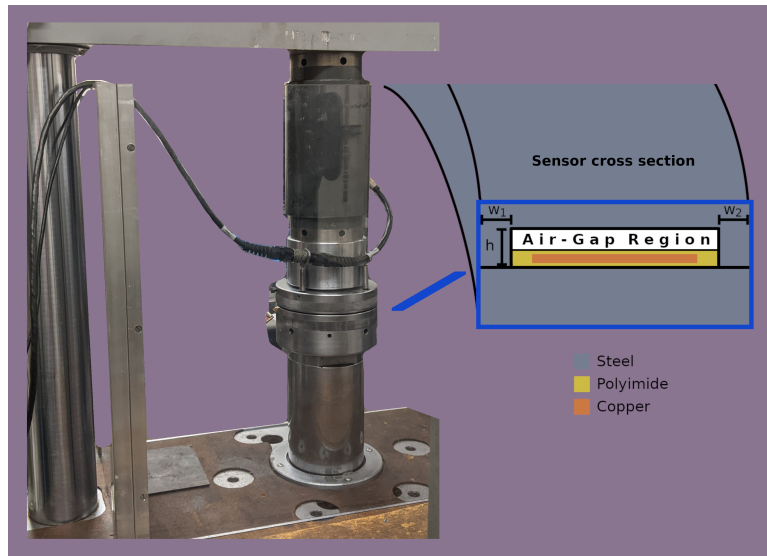


Figure 7.4 The setup for the load frame characterization of the sensor in the air-gap configuration, shown in the sensor cross section. The load frame applies a controlled loading profile to the sensor, allowing the response of the sensor to be compared against a controlled input. The load frame measures both force and displacement while the sensor's capacitance is measured by the interface circuit. Forces in this test ramp up to 200 kN and back down at a controlled linear rate.

For the rock cut testing, the linear cutting machine at Colorado School of Mines Earth Mechanics Institute, shown in Fig. Figure 7.5 is used. Two samples of coal embedded in concrete were cut using conical picks instrumented with one of the sensors. Wear and depth of cut are varied for the tests. The conditions for the test and the number of samples for each condition are shown in Table Table 7.1. The cutting speed was 25.4 cm/s (10 in./s). In this test, the sensor changes configuration, and empirical models are fit to transform the sensor measurements into normal force on the tool.

For this study, different mathematical models are used to describe the two tests performed with the sensor. For the load frame tests, the sensor sensitivity is low, but demonstrates the working principle of the sensor in a controlled environment. For the rock cutting tests, the sensor sensitivity is much greater. This

Table 7.1 Rock cut conditions tested, coal samples and conical picks

Depth of Cut	Wear Condition (Tip Diameter)	Number of Cuts
1.0 in.	New (3.71 mm)	10
1.5 in.	New (3.71 mm)	2
1.5 in.	Mod (17.9 mm)	4
1.5 in.	Worn (27.5 mm)	5
	Total	21

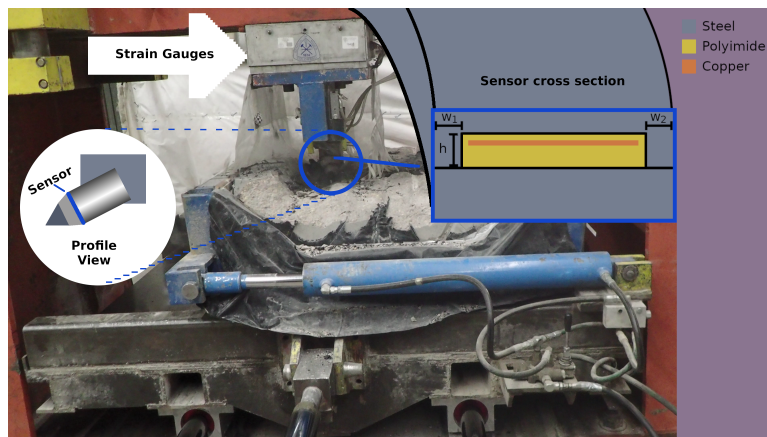


Figure 7.5 The setup for the rock cutting experiment. Strain gauges measure the forces on the cutting tool from close proximity while hydraulic actuators drag the rock sample against the cutting tool. The sensor is located between the sleeve and the block of the cutting tool, as shown in the profile view diagram. In this setting, the sensor is in the crushed gap configuration, shown in the sensor cross section. Forces in this test are less than 100 kN, but the rate of change of force is large and variable.

can be explained by plastic deformation closing the air gap area. The models before and after this event are referred to as the air-gap and closed area models, respectively. The following analytical models describe how this transition can increase sensitivity.

Due to the large number of design parameters, data-driven methods are leveraged to formulate the relationship between measurements and normal force on the tool. The analytical models show that the system is nonlinear, so a 2nd order polynomial expansion is used to allow the regression models to compensate more accurately. The analytical models for both configurations are described in the following subsection. After that, the next subsection discusses the regression techniques used to estimate cutting drag force from the sensor measurements.

### 7.3.1 Analytical Modeling

To model the relationship between input force and measured resonant frequency, the sensing element and the circuit inductance and capacitance is considered. Slight parasitic capacitance and inductance is present when comparing the analytical model to the experimental results. The FDC2114 Capacitance to Digital Converter is used to measure the resonant frequency of all four sensor channels. This setup has a resolution of 2.44 kHz per bit, and uses a reference frequency of 40 MHz and an internal gain setting of 2. With this configuration, the converter can measure resonant frequencies up to 4 MHz.

The resonant frequency of the sensing circuit is that of a parallel inductor and capacitor [164]:

$$f = \frac{1}{2\pi\sqrt{L_b[C_b + C_s]}}, \quad (7.2)$$

where  $L_b$  is the lumped inductance from the board and parasitics,  $C_b$  is the lumped capacitance from the board and parasitics, and  $C_s$  is the capacitance for the sensor element, which is electrically parallel to  $C_b$ . This model is used to explore the trade-offs in performance and changes in sensitivity between the two models. To describe the different design aspects of the sensor performance, the chain of derivatives from resonant frequency to input force:

$$\frac{\partial f}{\partial F_{in}} = \frac{\partial f}{\partial C_s} \frac{\partial C_s}{\partial d_r} \frac{\partial d_r}{\partial F_{in}}, \quad (7.3)$$

is helpful. The significance of each term on the right hand side is explained below.

It was found during calibration and testing that it is necessary to model both the air gap sensor, and a sensor with a closed area. The model with the air gap explains the characterization experiment with good accuracy, while the model with the closed area explains the rock cutting experiment with good accuracy. The closing of the air gap suggests that rock cutting produces large forces on the cutting tools. The character of the sensor deformation can be seen in Fig. Figure 7.3 Model diagrams for both modes of sensor operation are shown in Fig. Figure 7.6. The first term on the right hand side of Eq. 7.3, the sensitivity of

frequency to sensor capacitance, is the same for both of the sensor configurations. The other two terms are unique to each model.

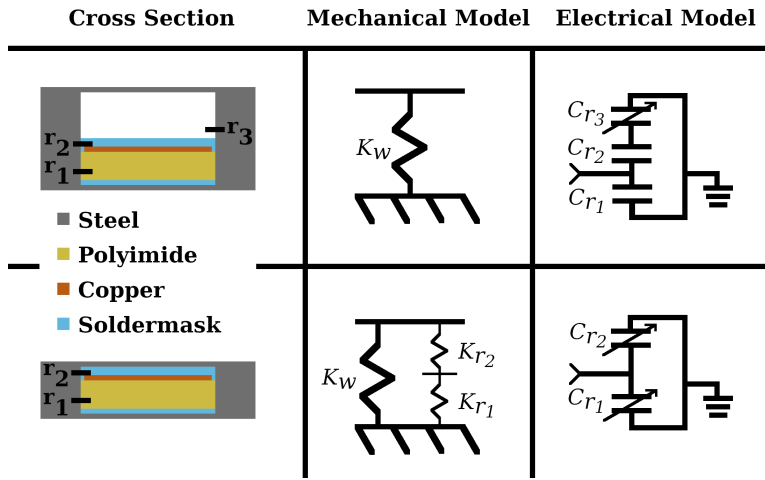


Figure 7.6 Cross section models for the two sensor modes. The top model has the air gap intact, resulting in one region which has variable capacitance. The bottom model has a closed air gap area, resulting in a stiffer sensor with two regions of variable capacitance. The top model is valid for sensors which have not undergone significant plastic deformation, while the bottom model is accurate for sensors after they have formed to the cutting tool. The measured stiffness of the case in the air gap configuration,  $K_w$ , is around 780 meganewtons/meter. In the closed area configuration, the polyimide contributes additional stiffness, as it occupies more than twice as much area as the steel walls and is very thin in comparison. The soldermask and polyimide are lumped together for the model of  $r_1$  since the soldermask is thin in comparison to the polyimide and has similar properties.

The sensitivity of sensor frequency with respect to sensor capacitance is:

$$\frac{\partial f}{\partial C_s} = \frac{-L_b}{4\pi(L_b(C_b + C_s))^{\frac{3}{2}}}. \quad (7.4)$$

If the other sensitivities,  $C_b$ , and  $L_b$  are held constant, larger  $C_s$  values will give less sensitive sensors. The second derivative has a similar shape, indicating that while less sensitive, larger  $C_s$  values will have more linear responses. To understand how the sensor responds to strain, the next term, the sensitivity of capacitance to displacement, is needed.

For the air gap sensor,  $r_3$  is the region where thickness varies with the input force. When considering the closed area sensor, both  $r_1$  and  $r_2$  will deform, with most of the deformation happening in  $r_1$  since it is less stiff in comparison to the much thinner  $r_2$ . The air gap sensor is less stiff than the closed area sensor, as the polyimide is much stiffer than the thin steel walls of the sensor. Nominal values for the design are shown in Table Table 7.2. Analytical models for both configurations are derived below, and empirical values for sensitivity are shown in the Results section.

Table 7.2 Nominal design values for sensor, crushed gap reduces  $h$ ,  $d_{r_1}$ , and  $d_{r_2}$ .

Geometric Parameter	Value	Electrical/Material Property	Value
$d_{r_1}$ , Height of $r_1$	127 $\mu\text{m}$	$\epsilon_{r_1}$ , Relative Permittivity of $r_1$	3.2*
$d_{r_2}$ , Height of $r_2$	25 $\mu\text{m}$	$\epsilon_{r_2}$ , Relative Permittivity of $r_2$	2 to 5†
$d_{r_3}$ , Height of $r_3$	240 $\mu\text{m}$	$\epsilon_{r_3}$ , Relative Permittivity of $r_3$	1.0
$h$ , Gap Height	457 $\mu\text{m}$	$K_w$ , Steel case stiffness	780 MN/m‡
$A$ , Plate Area	3.8 $\text{cm}^2$	Young's Modulus Polyimide	7.1 GPa*
$w_1, w_2$ , Wall Widths	2.4 mm	Young's Modulus Soldermask	2.4 GPa**
Inner Diameter	64.0 mm	$L_b$ , Board Inductance	18 $\mu\text{H}$
Outer Diameter	96.5 mm	$C_b$ , Board Capacitance	32 pF

\*: Panasonic Felios F775 Polyimide Datasheet

†: Not published, typical value range given here

‡: Measured with load frame experiment

\*\*: Taiyo America PSR-9000 FXT Series Datasheet

### 7.3.2 Air Gap

For the isolated sensor with an air gap, the model of input force to capacitance is derived as follows.

Each capacitive cell of the sensor is modeled as having three regions. The first region is between the electrode and the bottom of the steel case, consisting of polyimide and a thin layer of soldermask, roughly 25  $\mu\text{m}$ . The second and third regions are above the electrode and are the soldermask and air regions respectively. The first region is electrically parallel to the second and third regions, which are in series with each other.

When force is applied, the sensor case compresses, decreasing the thickness of  $r_3$ . The overall capacitance of the sensing element,  $C_s$  can then be modeled as:

$$C_s = C_{r_1} + \left[ \frac{1}{C_{r_2}} + \frac{1}{C_{r_3}} \right]^{-1}, \quad (7.5)$$

where each  $C_{r_n}$  is the individual capacitance of the region and  $C_{r_3}$  being the variable air gap region. To calculate the sensitivity capacitance with respect to displacement,  $C_{r_3}$  is expanded with Eq. 7.1 and partially differentiated with respect to  $C_s$ , yielding:

$$\frac{\partial C_s}{\partial d_{r_3}} = \frac{-\epsilon_{r_3} A C_{r_2}^2}{\left[ \epsilon_{r_3} A + C_{r_2} d_{r_3} \right]^2}. \quad (7.6)$$

Then, to find the upper bound of the sensitivity, the limit as the gap size approaches zero is found, simplified, and rearranged:

$$\lim_{d_{r_3} \rightarrow 0} \frac{-\epsilon_{r_3} A C_{r_2}^2}{\left[ \epsilon_{r_3} A + C_{r_2} d_{r_3} \right]^2} = \frac{-\epsilon_{r_3} A C_{r_2}^2}{\left[ -\epsilon_{r_3} A \right]^2} = \frac{-C_{r_2}^2}{\epsilon_{r_3} A} = \frac{-\epsilon_{r_2}}{\epsilon_{r_3}} \frac{C_{r_2}}{d_{r_2}}. \quad (7.7)$$

The sensitivity is upper bounded in magnitude by the product of the ratio of dielectric permittivities and the ratio of capacitance to thickness for  $r_2$ .

The thickness of  $r_3$ , denoted  $d_{r_3}$ , as a function of the input force,  $F_{in}$ , can be modeled as:

$$d_{r_3}(F_{in}) = d_g - F_{in}/K_w, \quad (7.8)$$

where  $d_g$  is the nominal thickness of the air gap region and  $K_w$  is the stiffness of the steel case walls. Sensor stiffness is a direct trade-off for sensitivity. A stiffer sensor will be less sensitive, but likely have more linear performance by limiting the range of displacement and capacitance. A thinner sensor will be more sensitive, as the same distance of displacement will cause much larger changes in capacitance. A very thin and stiff sensor would then have good sensitivity and the linearity can be achieved by tuning the overall stiffness.

### 7.3.3 Closed Area

Considering a closed air gap area means eliminating the third region from the electrical model and adding the stiffness of the flexible dielectric to the sensors physical model. In this mode, both regions should experience some deformation, but the thicker region is likely to be more sensitive since it should be less stiff. The sensor capacitance is given as the sum of the two regions:

$$C_s = C_{r_1} + C_{r_2}. \quad (7.9)$$

The sensitivity to displacement, after substituting in for  $C_{r_1}$  and  $C_{r_2}$  is then:

$$\begin{bmatrix} \frac{\partial C_s}{\partial d_{r_1}} \\ \frac{\partial C_s}{\partial d_{r_2}} \end{bmatrix} = \begin{bmatrix} \frac{-\epsilon_{r_1} A}{d_{r_1}^2} \\ \frac{-\epsilon_{r_2} A}{d_{r_2}^2} \end{bmatrix} \quad (7.10)$$

The deformations for the two regions are modeled as follows:

$$d_{r_1}(F_{in}) = d_{r_{1n}} - \frac{F_{in}}{\mathbf{k}_1} \quad (7.11)$$

$$\mathbf{k}_1 = \left[ K_w + [1/K_{r_1} + 1/K_{r_2}]^{-1} \right] \left[ K_{r_2}/K_{r_1} + 1 \right] \quad (7.12)$$

$$d_{r_2}(F_{in}) = d_{r_{2n}} - \frac{F_{in}}{\mathbf{k}_2} \quad (7.13)$$

$$\mathbf{k}_2 = \left[ K_w + [1/K_{r_2} + 1/K_{r_1}]^{-1} \right] \left[ K_{r_1}/K_{r_2} + 1 \right] \quad (7.14)$$

With the given Young's modulus and height for  $r_1$  and  $r_2$ , The flexible printed circuit can be expected to be have a total stiffness around 80 giganewtons/meter. The soldermask region stiffness,  $K_{r_2}$ , has a calculated value of roughly 275 GN/m, and the polyimide and soldermask region,  $K_{r_1}$ , has a calculated stiffness of roughly 116 GN/m. Increases in stiffness for this sensor configuration result in a more linear

sensor than one that is less stiff. Like the air gap sensor, the closed area sensor sensitivity still varies with the strain of the sensor.

The sensitivities of the two models are compared by rewriting Eq. 7.10 using the capacitances of the regions in the air gap sensor to give:

$$\begin{bmatrix} \frac{\partial C_s}{\partial d_{r_1}} \\ \frac{\partial C_s}{\partial d_{r_2}} \end{bmatrix} = \begin{bmatrix} -\frac{C_{r_1}}{d_{r_1}} \\ -\frac{C_{r_2}}{d_{r_2}} \end{bmatrix}. \quad (7.15)$$

And, depending on the shift in nominal values for  $d_{r_1}$  and  $d_{r_2}$ , the closed area configuration can have much greater sensitivity than the air gap model. The air gap configuration sensitivity is upper bound to a constant times the ratio  $C_{r_2}/d_{r_2}$ , that constant being the ratio of dielectric permittivities between the soldermask and air. In the closed area configuration, if  $d_{r_2}$  is reduced by half, due to plastic deformation in this case, the capacitance will double and result in four times more sensitivity in that term alone. The ratio of permittivities is roughly between two and five, so the additional sensitivity from adding  $r_1$  and compression of the sensor is likely to make the closed area configuration more sensitive compared to the air gap configuration.

#### 7.4 Regression Techniques

The methods used to transform the sensor measurements to drag force estimates in the rock cutting experiment are linear regression [165] and neural networks with rectified linear units for the activation function [166, 167]. For both methods, two sets of coefficients are used: the 4 channels of the sensor and the 2nd order polynomial expansion of the four channels. For each of the four regression methods, it was found that the higher frequency inputs were not correlated to the regression target. So, the effect on performance of low pass filters with different cutoff frequencies used on the input are also tested. A summary of the chosen regression methods and their size is shown in Table Table 7.3.

Each of these models are compared using 100 random 70:30 test and train splits, a technique known as Monte Carlo cross validation [168]. Problems can arise when using this method to validate classification of features that are rare in the data set [169, 170]. A large number of splits are used, with only 30% of data used for training in each split, to try to accurately capture the performance distributions. The input

Table 7.3 Regression methods and number of inputs and trainable parameters.

Regression Technique	# Input Variables	# Parameters
Linear Regression of channel values	4	5
2nd Order Polynomial Regression	13	14
Neural Network with channel values	4	65
Neural Network with 2nd Order Poly.	13	645

dimension is small, either 4 or 13 values, compared to the number of samples, 46,201 data points. A good regression fit would demonstrate linear performance of the sensor for average force estimation, and that the performance in this test would generalize to an expanded dataset.

The regression methods are compared on the basis of mean absolute error and  $R^2$  score [171–173]. The pursuit of a best metric is often debated, and the selection must be applied appropriately [174]. The root mean squared error and the  $R^2$  scores will provide the same overall ordering for the methods. The mean absolute error will give less penalty to outliers than the  $R^2$  score [175]. Since instantaneous readings of the four sensor channels are used, the input dimension is small and the  $R^2$  score does not need adjustment [173]. The  $R^2$  score is a good proxy for force tracking while mean absolute error is a good metric for accuracy. Using a collection of metrics promotes a better qualitative analysis of the regression models' performances.

Each method is framed as trying to solve for the instantaneous normal force on the tool,  $y$ , from a vector of sensor measurements  $x$ . This measurement vector for the instantaneous linear case is written as:  $x = [a, b, c, d]^\top$ , where  $a, b, c$  and  $d$  represent the values from the four sensor channels at that moment. The channel values are the measured change in resonant frequency since right before the current cut. For the polynomial case,  $x$  is expanded with the unique 2nd order pairings as

$$x = [a, b, c, d, a^2, b^2, c^2, d^2, ab, ad, bc, bd, cd].$$

The linear regression method aims to find a set of coefficients  $\{L_1, \dots, L_n\}$ , where  $n$  is the size of the input dimension, and a scalar bias,  $B$ , such that:

$$y = \sum_{i=1}^n L_i x_i + B. \quad (7.16)$$

Given a finite set of input-output pairs, the optimal  $L_i$  and  $B$  values that generate the least error according to different metrics can be calculated in closed form [165]. This regression method is robust in the sense that it has few parameters, can operate of a small number of input variables, and will have predictable output for all inputs.

The neural network regression models take a similar approach to the linear regression. The neural network consists of layers of neurons, where each neuron in each layer applies an activation function to a weighted sum of the outputs from the previous layer. The rectified linear activation function [166] is used, which has the form:

$$\sigma(\cdot) = \begin{cases} 0, & \cdot \leq 0 \\ \cdot, & \text{otherwise} \end{cases}. \quad (7.17)$$

This activation function allows nonlinear relationships to be modeled by the neural network.

The number of neurons in a layer is the width, and the number of layers of neurons is the depth. Consider a network with depth  $D$ , we denote the width of each layer as  $W_d$  for  $d \in \{1..D\}$ . For a single neuron at layer  $d$  and position  $t \in 1..W_d$ , and the previous layer having width  $W_{d-1}$ , the output is:

$$s_{d,t} = \sigma\left(\sum_{i=1}^{W_{d-1}} L_{i,t} s_{d-1,i} + B_{d,t}\right). \quad (7.18)$$

where  $\sigma(\cdot)$  is the activation function, the  $L_{i,t}$  represent the learned coefficients,  $s_{d-1,i}$  are the output from either the neurons in the previous layer or the input data vector entries for the first layer, and  $B_{d,t}$  is the learned bias for the neuron. The output of the neural network is a weighted sum of the outputs of the neurons in the last layer with no activation function:

$$y = \sum_{i=1}^{W_D} L_{i,t} s_{D,i} + B_D \quad (7.19)$$

This means that each neuron has roughly the same number of parameters as the entire linear regression problem. A large enough network such as this can memorize a finite data set [176]. A smaller network is more general, while a larger network will begin to highlight any biases in the collected data. Unlike the linear regression problem, solving for the neural network coefficients is done via an iterative process. To limit the number of parameters from being too large, A network size of 3 hidden layers is chosen, with the width the same size as the input.

The experiments are implemented using scikit-learn, a.k.a. sklearn, [113] and ran on a laptop computer. The regression experiments take a couple hours to run. The code is available at:

[https://github.com/Fworg64/air\\_gap\\_coal\\_sensor\\_model](https://github.com/Fworg64/air_gap_coal_sensor_model). The analytical models reveal that the system is nonlinear and has polynomial terms. This analysis guides the selection of empirical models and preprocessing methods.

## 7.5 Results

The sensitivity of each configuration is compared empirically based on the results. The slope magnitude for the linear regression of the air gap characterization test is 10.164 kN/kHz, and so for each kilonewton of force, the resonant frequency drops by about 98.4 Hz. The sensitivity of the closed area sensor is derived using the average of the coefficients from the linear model trained on the rock cutting data. The average of the crushed gap values is 0.1522 kN/kHz, which means that each kilonewton of force reduces the resonant frequency by roughly 6.57 kHz. The values for both models are shown in Table Table 7.4.

The closed area configuration is over 65 times more sensitive than the air gap sensor. The air gap sensor has about 8 levels over the 200 kN input range. With the closed area sensitivity and the capacitance to digital converter resolution of 2.44 kHz, The crushed gap has roughly 80 levels over the same range,

giving it 10 times the resolution. Using Eq. 7.10, it is inferred that  $d_{r_1}$  and  $d_{r_2}$  have been crushed to a fraction of their original thicknesses.

## 7.6 Air Gap Load Frame Characterization

The results from the load frame characterization of the sensor show that the response is noisy but linear over the tested range. In the repeated test, the sensor had almost identical performance but without the initial plastic deformation in the 2 kN/s test. The strain of the sensor for each test, shown in Fig. Figure 7.7, was nearly identical after the initial plastic deformation. The plot shows significant deformation of one of the test sensors during its first loading cycle. After this first loading cycle, the device strain for each test sensor is similar. The peak force of each test is 200 kN, and the sensor consistently deforms with a strain of 0.14 at this peak. Considering a sensor height of 1.83 mm, the stiffness,  $K_w$ , is roughly 780 MN/m.

The load frame force measurements and the sensor measurements from the test for the air gap sensor are shown in Fig. Figure 7.8. The test suite is repeated for the prototype that is not used in the rock test and the measurements are consistent between the tests. There is some plastic deformation of the steel case during the initial loading of the sensor in the 2 kN/s case. After this, the sensor has a mostly symmetric response to loading and unloading. The two sensors have similar sensitivity, but different offsets after the plastic deformation phase.

An XY plot of the traces is shown in Fig. Figure 7.9, which highlights the linear range and repeatability of this configuration. The 2 kN/s tests are not representative due to their large, one-time swing in values caused by the initial plastic deformation. They are excluded for this graph and the sensitivity calculation. There is some measurement creep, but ramping the input force to 200 kN will increase the digital sensor measurement roughly 5 to 8 levels. The bias for the resonant frequency is reset at the beginning of each test just before force is applied. Compared to the first sensors 4 kN/s test and the second sensors first 10 kN/s test, most of the other tests have similar measurements.

### 7.6.1 Rock Cutting and Model Fitting

The initial sensor design was for the air gap configuration. The sensitivity as measured by the load frame test was deemed sufficient for binary classification of hard or soft rock. The fact that the sensor

Table 7.4 Model values for linear regression coefficients and bias terms.

Linear Reg. Parameter	$a_1$ (N/Hz)	$a_2$ (N/Hz)	$a_3$ (N/Hz)	$a_4$ (N/Hz)	$b$ (N)
Air Gap Value		10.164			19.338
Closed Area Value	0.0406	0.4033	0.0510	0.1139	-1.448

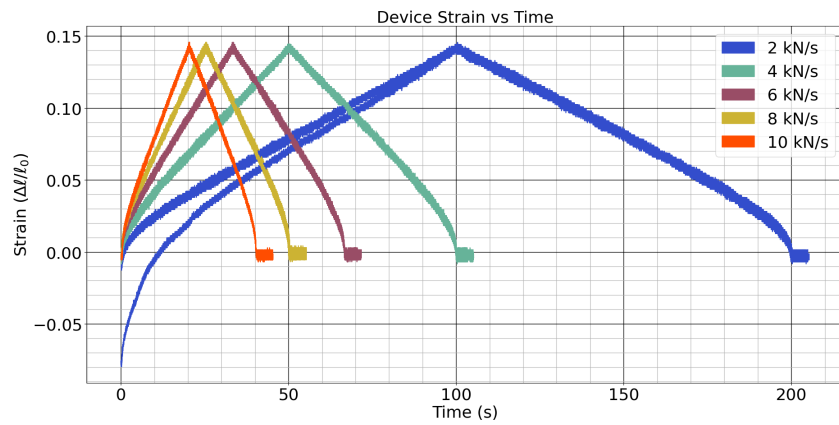


Figure 7.7 The strain of the physical sensor cases during the tests.

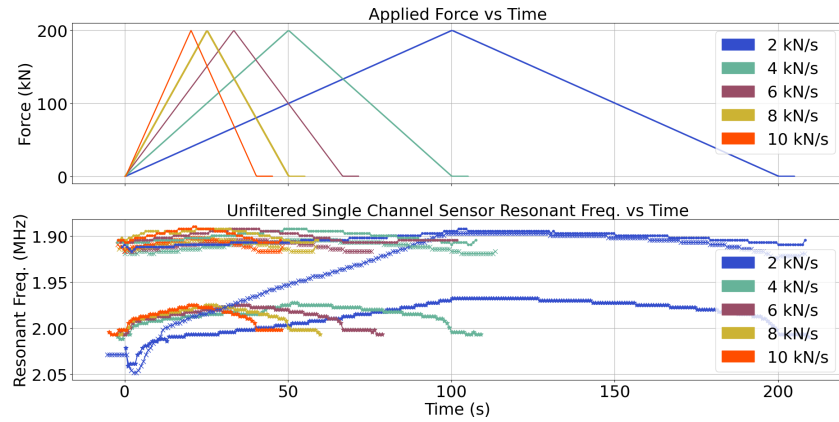


Figure 7.8 Force profiles and capacitive measurements during loading for the two test sensors.

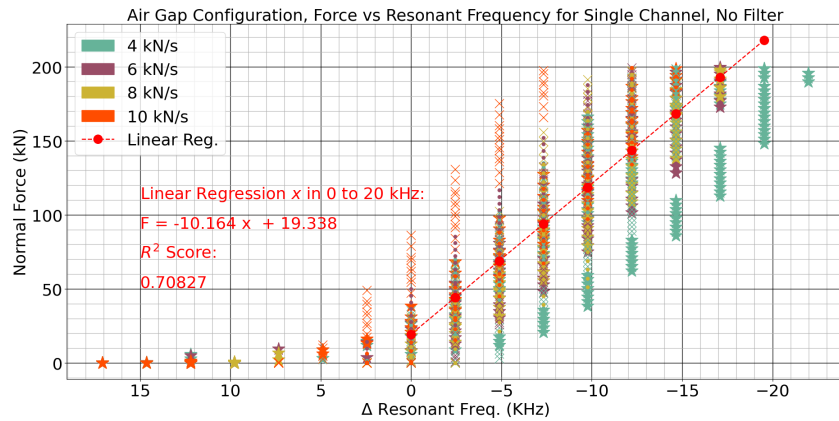


Figure 7.9 The relationship between measured resonant frequency and applied force for each sensor.

compressed into a more sensitive version under the rock cutting forces demonstrates that a sensor must be robust to the large forces in this application. The toughness of the steel and polyimide, and their increased stiffness after compression, resulted in a usable sensor.

For the rock cutting experiments, the linear and neural network models previously discussed in Section 7.4 are fit to the data. The large number of parameters in the physical model make these regression techniques a good fit for estimating the cutting force. Prediction results for a few samples with new picks are shown in Fig. Figure 7.10. More prediction results using the worn tool are shown in Fig. Figure 7.11.

The strain gauge measurements have large variance due to the rock chipping at high frequency. The regression target is highlighted in magenta. The different regression methods track the force as the tool cuts through the sample. The middle of the sample is coal, and generally takes less force to cut than the surrounding concrete. The sensor could be used to identify changes in material based on differences in cutting force. Use of the worn tool causes greater peak force values in the experiment. The sensor is able to track the force with different wear conditions using each of the regression techniques. The sensor could be used to detect changes in tool wear based on increases in cutting force when cutting the same material.

Using a low pass filter on the sensor measurements improves performance. The mean absolute error for each classification method using the different low pass filters is shown in Fig. Figure 7.12. The  $R^2$  scores are shown in Fig. Figure 7.13 Using a cutoff frequency of 10 Hz or 5 Hz gave the best results across methods. The neural network regression method with the 2nd order polynomial expansion performed the best overall.

By filtering the measurements before fitting the regression, the tracking error is reduced. The performance of the 2nd order polynomial feed-forward neural network regression breaks away from the rest due to its greater capacity for nonlinear modeling. Using a cutoff frequency the same or slightly lower than the regression target gave the best results. The filtering was needed to make the best performing method reliable, as the control case gave some regression methods which did not function well for all splits. The regressions without neural networks gave very consistent performance.

The analytical models show that the relationship between resonant frequency and input force is nonlinear, using hyperbolic and inverse square root terms. Use of the 2nd order polynomial expansion improved results for both the linear regression and the neural network regression. Use of more sophisticated methods like the neural network regression method significantly improves performance when used with the 2nd order polynomial expansion. The neural network without the expanded input was less reliable, with some fraction of the trained classifiers always giving bad performance.

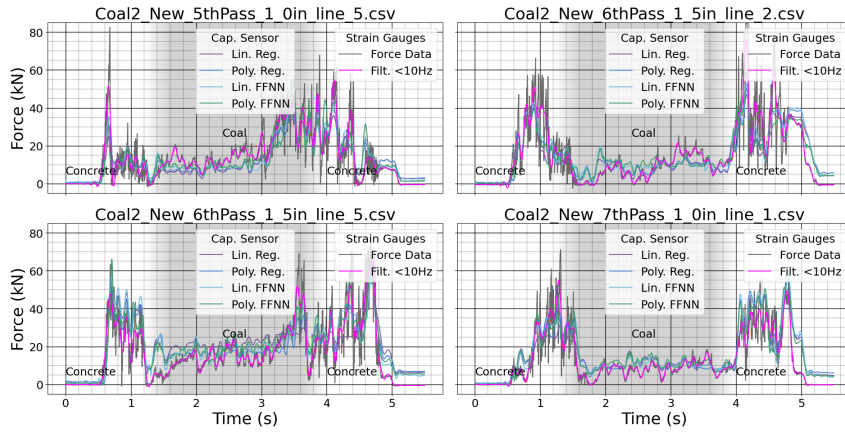


Figure 7.10 Measurements from both the system strain gauges and the custom sensor for the new tool.

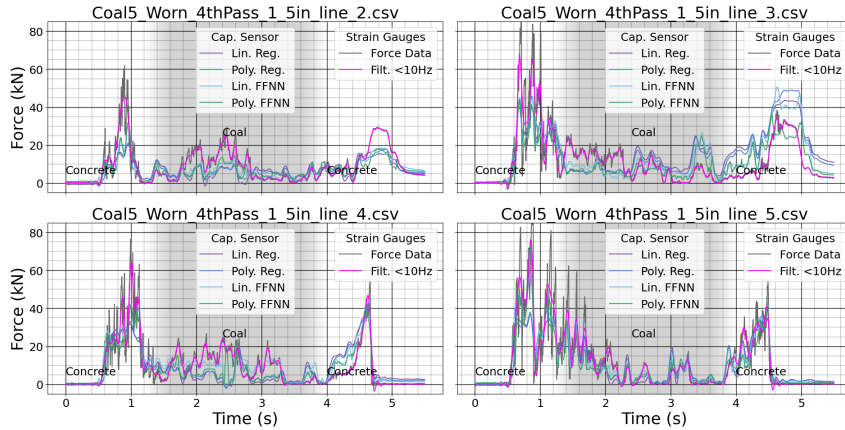


Figure 7.11 Measurements from both the system strain gauges and the custom sensor for a worn tool.

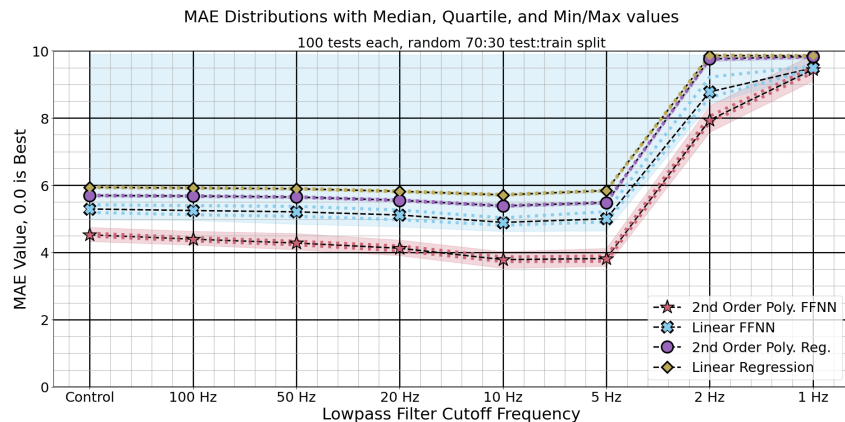


Figure 7.12 Mean Absolute Error distributions for different input filter conditions. The markers and dashed lines represent the median, while the dots and shaded area represent the quartile and min/max values respectively. Lower scores are better.

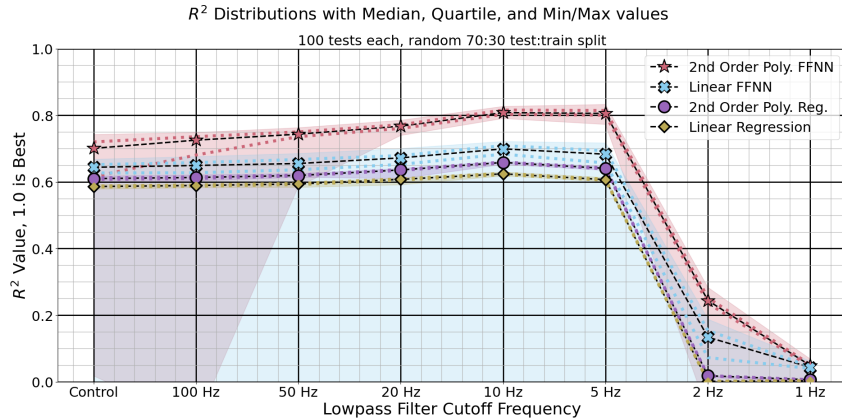


Figure 7.13  $R^2$  score distributions for different input filter conditions. The markers and dashed lines represent the median, while the dots and shaded area represent the quartile and min/max values respectively. Higher scores are better.

## 7.7 Discussion

The average normal force is tracked for this study, as this quantity is known to be correlated with both tool wear and material type. The signal is averaged using a low pass filter with a cutoff frequency of 10 Hz, to allow the higher frequency rock chipping forces to be averaged together while still allowing a quick response for material and wear changes. When restricting the regression target bandwidth, the overall variance of the signal is reduced. The higher frequency components are not needed to track the average.

The sensor sensitivity could be improved by using thinner dielectric regions, but care must be taken to stay within the linear deformation range for the polyimide material. Polyimide has linear characteristics for small deformations, but is known to experience hysteresis and temperature dependence [177–179]. The deformation characteristics of thin film polyimide sheets after compression to a fraction of their original height should be investigated and compared to uncompressed sheets of the same height.

The air gap configuration was useful for gentle load profiles and could have applications outside of underground mining. In the rock cutting experiment, the polyimide likely deformed to be much thinner than it was initially. For the closed area configuration, the sensitivity of capacitance to distance increases to infinity as the layers become thinner. The closed area configuration is more stiff than the air gap configuration, which helps the sensor keep its linear performance.

## 7.8 Conclusion

The sensor performed well for estimating the cutting force, even when using the simple linear regression model. The ability to track cutting force with a sensor can improve operator performance and safety by

giving them objective feedback while they maintain a safe distance. Worker efficiency can be increased via addition of autonomous process control enabled by sensors on the continuous miner cutter-head picks. We have validated our sensor under laboratory conditions and believe this technology is ready for the next stage of integration with the target application.

Capacitive sensors are a promising technology for applications which require low power and low cost. This work has shown design and validation for two different models of capacitive sensor. This design should be easily adaptable to other robotic applications. Our work shows the implementation of a single sensor. Forming a network of these sensors would allow the full cutter-head state to be known without stopping operations or requiring the operator to get close to the cutting interface, improving operator safety and efficiency.

### **7.8.1 Acknowledgments**

Special thanks to the Earth Mechanics Institute at Colorado School of Mines for helping run the experiments.

## **7.9 Declarations**

### **7.9.1 Funding**

This work was funded by NIOSH Contract 75D30119C05413, IMPROVING HEALTH AND SAFETY OF MINING OPERATIONS THROUGH DEVELOPMENT OF THE SMART BIT CONCEPT FOR AUTOMATION OF MECHANICAL ROCK EXCAVATION UNITS AND DUST MITIGATION.

### **7.9.2 Conflict of interest**

The authors declare that there is no conflict of interest.

### **7.9.3 Availability of data and materials**

The data used for this research is available publicly at:

[https://github.com/Fworg64/air\\_gap\\_coal\\_sensor\\_model](https://github.com/Fworg64/air_gap_coal_sensor_model)

### **7.9.4 Code availability**

The code used for this research is available publicly at:

[https://github.com/Fworg64/air\\_gap\\_coal\\_sensor\\_model](https://github.com/Fworg64/air_gap_coal_sensor_model)

## CHAPTER 8

### LOAD CELL DESIGN COMPARISON

Over the course of this program, two primary load cell designs were tested. The first design had two electrodes separated by a thin,  $25 \mu\text{m}$ , layer of polyimide. The second design had a single electrode coated in soldermask and attached to a thicker,  $100 \mu\text{m}$ , layer of polyimide. Both designs were tested in a load frame and in full scale rock cutting tests. The results from both kinds of tests for both sensors are shown below.

#### **8.1 Load Frame Testing**

Comparable XY plots are shown for both the first and second design in Figure 8.1. The first design is the “Dynamic Flex Configuration” and the second is the “Air Gap Configuration”. One thing that was the same for both sensor designs was the steel case. This case is made of stainless steel, and has a measured stiffness of around  $780 \text{ MN/m}$ . The walls of this case provide the stiffness and repeatable deformation characteristics needed for a robust sensor. This case also provides protection to the sensing element by shielding it from debris and electromagnetic interference.

It can be seen in the load frame testing graphs that the air gap design gives a much cleaner measurement, in that it has much less noise and reduced hysteresis. The plastic deformation of the sensor case is about the same magnitude for both designs. The air gap design is also more sensitive in the load frame test than the dynamic flex cell configuration. Both sensors saw their sensitivity increase when used in the rock cutting tests.

#### **8.2 Rock Cut Testing**

The first design was already very thin when it went into the rock cutting test. The nonlinear deformation characteristics of the thin film made it difficult to determine cutting forces, but still allowed frequency analysis for determining material type and tool wear. The second design ultimately altered to the “Crushed Gap Configuration” when used for rock cutting. This final form had even greater sensitivity and linearity, which allowed estimation of cutting forces.

Measurements for individual sensor channels and the measured and estimated forces are shown in Figure 8.2. When attempting to estimate the rock cutting forces to determine material type and tool wear, the problem can be relaxed to estimating average cutting force, as the differences in cutting force between the conditions are great. The cutting force bandwidth was limited to 10 Hz for the study, as this is believed to still provide an adequate response time while providing good averaging.

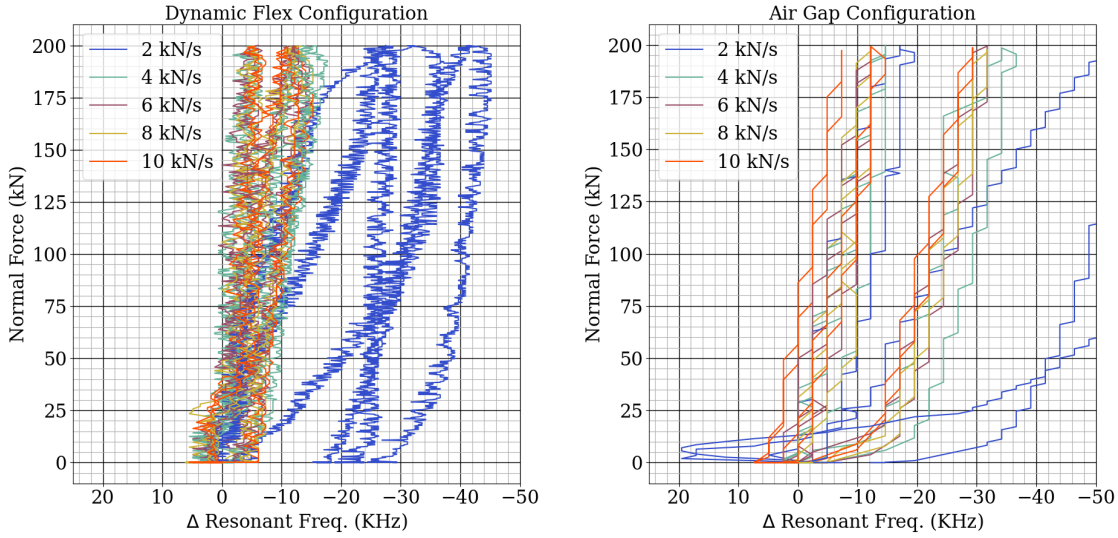


Figure 8.1 Comparison of original design, left, and improved design, right. The original design was noisy, had slightly less initial plastic deformation, and similar sensitivity when compared to the improved “Air Gap Configuration”. The air gap design had much better repeatability and less hysteresis in comparison to the original. The air gap design ultimately became more sensitive when used in the rock cutting tests.

By averaging the cutting force, the individual rock chipping forces are lost. These forces are averaged together to form a measurement which varies less with time. The high frequency rock chipping forces are correlated to rock material type and tool wear by their frequency. The average magnitude of these forces is of interest when attempting to determine specific energy of a particular tool wear and rock material type setup.

Force on the cutting tool is determined by the tool geometry and the material. The force is also influenced by the dynamics of the machine. The physical sensor system also has dynamics, and depending on the model, these dynamics can be non-stationary. The first design that was tested had non-linear, non-stationary dynamics. The second design was more linear and the bias could be tracked and compensated.

The nonlinear dynamics of the first design caused the vibrational modes to shift in ways that could not be captured completely with linear models. The sensor response was not chaotic, and it could still be predicted. In general, the thin film allows low frequencies and also very high frequencies to pass. It is possible that energy from some frequencies is moved into others, and there are other frequencies which are clearly blocked by the membrane.

The follow up air gap design could work for applications with more gentle load profiles, but considering that the gap will be closed when exposed to rock cutting forces means that this aspect of the design is

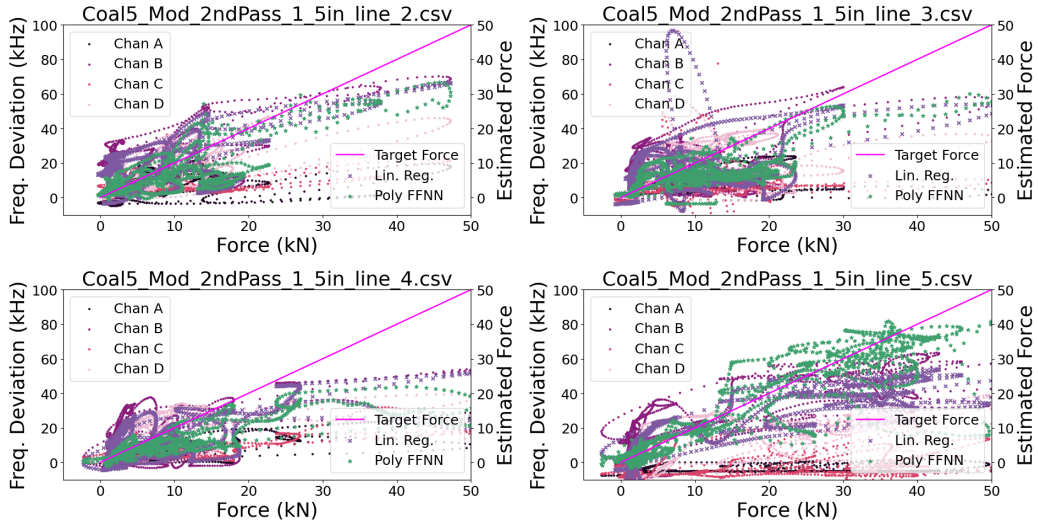


Figure 8.2 The individual channel measurements and the resulting force predictions for a few choice cuts, using the “Crushed Gap Configuration” of the second sensor design. The change in resonant frequency from the initial value is plotted versus the target force for each sensing channel in the sensor. The resulting force estimate provided by both the linear regression and the neural network using the 2nd order polynomial expansion are shown. Ideal performance is shown along the magenta line. The neural network method is able to untangle some of the non-linearity in the response. The performance of the neural network is comparable to the strictly linear model. The sensor is not completely linear, but can still provide useful measurements using a linear model.

unnecessary. The first sensor design has a high bandwidth due to its thin film. High bandwidth sensing is good for frequency analysis methods. More linear and robust sensors are generally bulkier, but at the cost of sensitivity. By starting with a thick polyimide film and allowing it to be compressed during the application, a robust sensor that is stiffer and more sensitive than the original design is achieved.

The first design used in this research was very nonlinear, so determining forces with the measurements did not give useful results. The second design was much more linear in comparison, and was able to be used to give force measurements. The seconds design was still nonlinear, but the nonlinearities were able to be either ignored in the linear model case or measured and compensated in the neural network case. Both capacitive load cell designs were suitable for material and wear classification, although the latter design was only used to show force measurements. Use of these measurements for rock type and tool wear classification would be trivial using the classification methods shown in this work.

## CHAPTER 9

### LONGER DOWNSAMPLING RATES FOR ACOUSTIC CLASSIFICATION

During the study of tool wear classification via acoustic spectra, different preprocessing methods were tested. The fraction of dimensions that showed significant differences across wear categories was used to predict preprocessor performance. For example, the time domain data does not generally have specific time offsets whose sample value correlates to the wear category. In comparison, the frequency domain data at different frequencies is likely to change between wear categories due to the changing tool geometry and increased cutting forces that accompany tool wear.

The results of our study indicated that the unmodified Fourier spectra magnitude values provided the better classification results than attempting to transform the values further. For example, the square of these values, a.k.a. the power spectral density, was tested as well as the square root of the values. Discussion of these different preprocessing methods is given below, followed by a discussion of data size in this experiment.

#### **9.1 Alternate Acoustic Preprocessing Methods**

Plots of data distributions for the wear categories before normalization are shown in Figure 9.1. Plots of the significant differences between wear categories for each type of preprocessing is shown in Figure 9.2. Normalization has no effect on the significance of the differences. In general, the unmodified Fourier spectra gave the best performance.

Other types of preprocessing tricks were applied in an effort to maximize the fraction of dimensions which correlate with tool wear. Filtering in the frequency domain was applied to smooth the frequency response over the frequency domain. This way, bands of irrelevant frequencies can be brought closer to the values of neighboring bands that are significant. Also, boost filters were applied to increase peaks that are relevant to wear category and exaggerate the trends. Ultimately, these techniques did not improve upon the performance given by the unmodified Fourier spectra magnitude.

The result of low pass filtering in the frequency domain is similar to the effect of downsampling followed by up-sampling via zero padding in the time domain. The variance of the frequency response over the frequency domain is reduced by clumping the modes together. Assuming vibrations are caused by a system that is stationary in the short term, the variance of the frequency response measurement is reduced by using a longer sample. This provides increased frequency resolution over the domain, but at the cost of longer response and classification times.

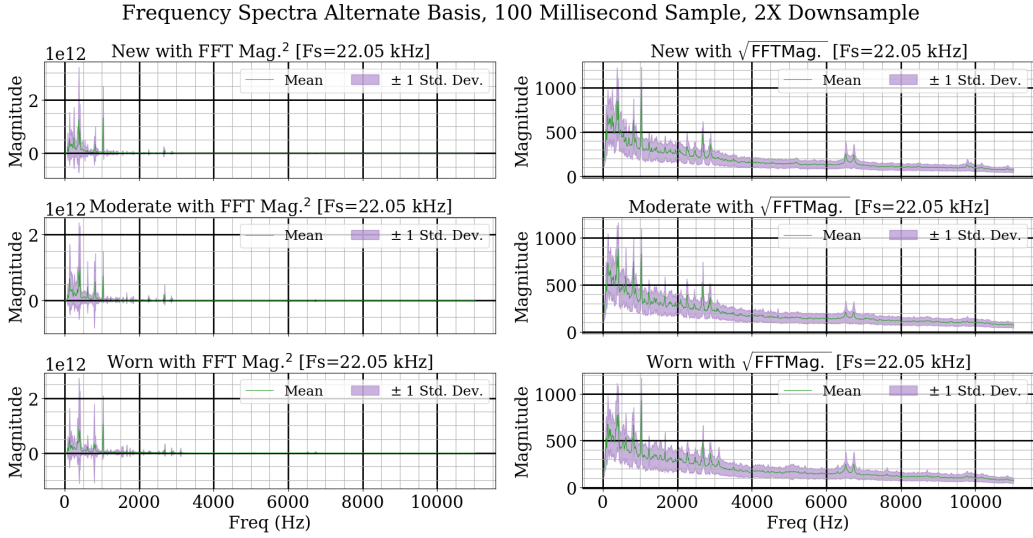


Figure 9.1 Data distributions for the tested wear categories using additional Fourier based preprocessing techniques. The square of the magnitude is an estimate of the power spectral density of the signal. The square root of the magnitude conditions the signal so that the higher frequencies with small magnitudes have magnitudes closer to the lower frequencies with large magnitudes. Neither of these methods gave better classification results than the unmodified Fourier spectra magnitude.

Window shapes can have subtle but important effects on results. For the concrete sample in this work, much of the acoustic energy was below 6 kHz. The higher frequencies still had significant differences, but the environment in an underground mine dampens these frequencies while being fairly permissive to lower frequencies. Our chosen window captures the lower frequencies, but other windows could allow better performance from higher frequencies. Future work should investigate optimal window shapes.

## 9.2 Comments on Data Size

For this experiment, around 90 seconds of acoustic data was used. To ensure sufficient power of the results, small samples had to be used. It was found early in the study that long samples with some downsampling gave good results. The limits of the reliability of this method have not yet been found, but as sample length increases, recorded signals will capture more information for a reliable estimation of cutting parameters.

More data should be collected to investigate using even longer window length for samples. This window length is only limited by the necessary rate of classification and acceptable delay. In general, the classification will be delayed by the length of the window. The classification calculations are much shorter in computation time than the sample length, so this does not add much to the delay. Longer sample lengths stand to increase classification accuracy, and additional demand for computational resources in this case can be mitigated by downsampling the recorded signal.

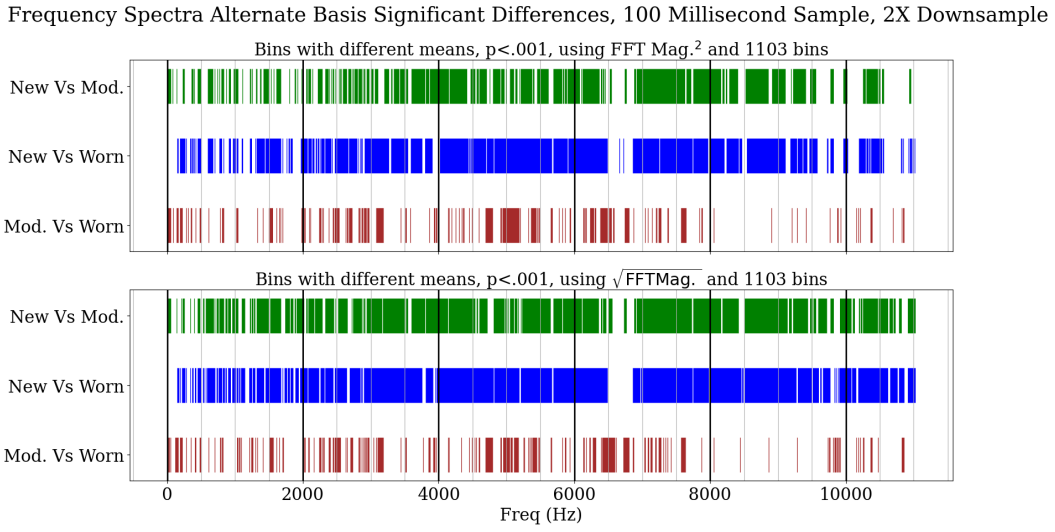


Figure 9.2 Tests for significant differences in frequency content between wear categories for the additional Fourier based preprocessing techniques. The square root was able to bring the differences between more high frequencies into significance compared to the square, or power spectral density. Squaring a signal will make outliers larger, while the square root conditions by bringing all numbers closer to unit value. Neither of these methods adds more information or improves the signal basis for classification over the spectra magnitude. However, they do perform much better compared to using time domain data.

Another thing that large sample windows can help mitigate is undesired performance caused by outside interference on the audio signal. Performance under these conditions would need to be characterized for a wide number of circumstances. One benefit the acoustic sensor has in this regard though is that almost every frequency bin value is correlated to a tool wear condition. This means that even if some frequencies are experiencing interference, there are likely many other frequencies that can still be used to make an accurate classification.

## CHAPTER 10

### SENSOR LINEARITY AND IMPLEMENTATION RECOMMENDATIONS

To map the crushed gap sensor measurements to estimated forces, a regression to the forces as measured by the Linear Cutting Machine's strain gauges was used. This method has a few limitations, the most significant being the distance between the tested sensor and the strain gauges. Because of the distance, the higher frequency force components will be out of phase when compared. In addition to the distance, the viscous nature of the polyimide dielectric distorts the frequency response when the two measurements are compared. The electronics for the sensor also contribute high frequency noise to the measurement. For these reasons, the higher frequency components of the force are not directly correlated between the two systems. A plot of the transfer function between the measurements is shown in Figure 10.1.

The final sensor prototypes are shown in Figure 10.2. When it comes to integrating this sensor with the target application, construction of the sensor contributes to overall linear performance. The steel case is assembled using the laser weld procedure described in Appendix A. Simulation for the capacitance of the air gap is described in Appendix B. Computer aided solving of the analytical model equations for the air gap and closed area sensors is shown in Appendix C.

The capacitive steel donut with viscous polyimide filling is a useful base design for many robotic applications. Robustness, linearity, and sensitivity are important parameters for any sensor design. Ways to improve each of these categories is listed in Table 10.1. To overcome the conflicting directions between sensitivity and the other design goals, use a thicker film and compress it down so that it becomes more thin and stiff. Based on the other results in this work, high frequency classification should also be considered a valid method for determining material type and tool wear. Directly embedding a piezo element within the tool could also serve to measure higher frequency vibrations which vary with cutting parameters. Future works may be able to integrate the sensing membrane with the cutting tool, using the tool to protect the sensor while it measures vibrations or cutting forces.

Table 10.1 Changes to design parameters that would improve certain categories

Parameter	Robustness	Linearity	Sensitivity
Dielectric Thickness	+	+	-
Dielectric Stiffness	+	+	-
Dielectric Permittivity	No effect	+	+
Case Walls Thickness	+	+	-
Sensing Electrode Area	+	+	-

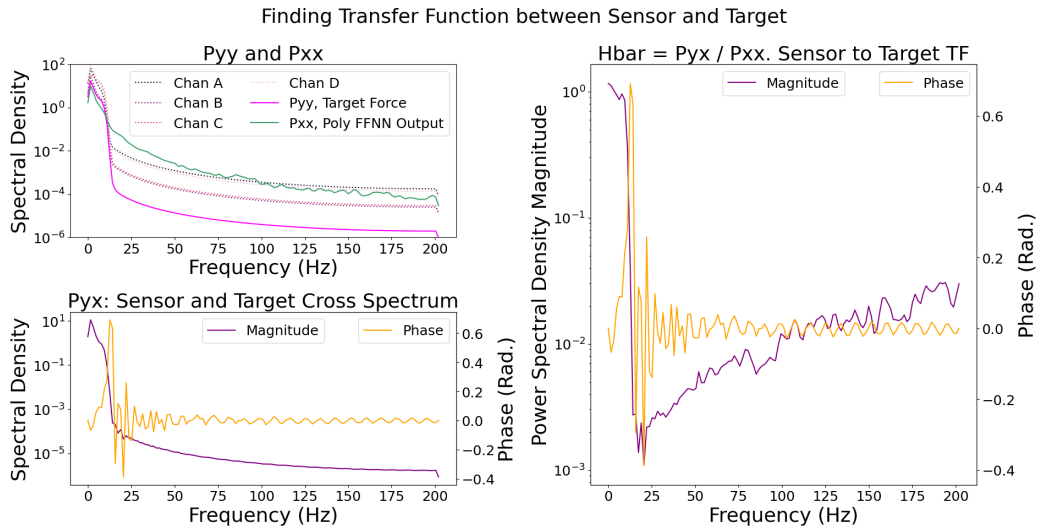


Figure 10.1 Power spectral density of sensor, target, and transfer function between them. The regression target has been low pass filtered with a cutoff frequency of 10 Hz, which can be seen by the steep drop in magnitude at this point. The individual sensor channels have the same filter applied to limit high frequency input. The cross spectrum,  $P_{yx}$ , shows that there is good correlation between the low frequency components of the estimate and the target. The transfer function between the estimate and the target suggests that additional filtering after the regression method could improve results. Post-processing requirements depend on the application, and additional filtering after regression could be a useful technique for tuning performance.



Figure 10.2 The air gap sensor membrane, left, and an assembled prototype, right. The sensor case provides additional protection from the environment. The device is assembled via laser welding. Future sensor designs could omit the steel case and integrate the sensor directly within the block or sleeve of the tool. This type of sensor measures cutting forces via the change in capacitance caused by the displacement of the top of the case when force is applied.

## REFERENCES

- [1] Benjamin Hopkins Miller. Smartbit: in-situ bit/rock interface monitoring device, 2003. URL <http://hdl.handle.net/11124/170545>.
- [2] Sakir Selcuk. Analysis of coefficient of rock strength and measurement of percussive penetration rates and bit wear, 1981. URL <http://hdl.handle.net/11124/14359>.
- [3] Allen D. Gray. New types of drill rounds for development openings, 1952. URL <http://hdl.handle.net/11124/13192>.
- [4] Augustus L. Moore. Investigation of rock drill bits, an, 1946. URL <http://hdl.handle.net/11124/16423>.
- [5] Param Jit Singh. Study of the development of rock drill bits with special reference to the calumet and hecla copper company bits, a, 1948. URL <https://hdl.handle.net/11124/176345>.
- [6] Valery A. Kononov. Telecontrol for mining machinery. *IFAC Proceedings Volumes*, 28(17):21–27, 1995. ISSN 1474-6670. doi: [https://doi.org/10.1016/S1474-6670\(17\)46740-1](https://doi.org/10.1016/S1474-6670(17)46740-1). URL <https://www.sciencedirect.com/science/article/pii/S1474667017467401>. 8th IFAC Symposium on Automation in Mining, Mineral and Metal Processing 1995 (MMM'95), Sun City, South Africa, 29-31 August.
- [7] William H Schiffbauer. An active proximity warning system for surface and underground mining applications. 2001.
- [8] Joana Duarte, Fernanda Rodrigues, and Jacqueline Castelo Branco. Sensing technology applications in the mining industrya systematic review. *International Journal of Environmental Research and Public Health*, 19(4), 2022. ISSN 1660-4601. doi: 10.3390/ijerph19042334. URL <https://www.mdpi.com/1660-4601/19/4/2334>.
- [9] Michail E. Kiziroglou, David E. Boyle, Eric M. Yeatman, and Jan J. Cilliers. Opportunities for sensing systems in mining. *IEEE Transactions on Industrial Informatics*, 13(1):278–286, 2017. doi: 10.1109/TII.2016.2636131.
- [10] Jonathon Ralston, David Reid, Chad Hargrave, and David Hainsworth. Sensing for advancing mining automation capability: A review of underground automation technology development. *International Journal of Mining Science and Technology*, 24(3):305–310, 2014. ISSN 2095-2686. doi: <https://doi.org/10.1016/j.ijmst.2014.03.003>. URL <https://www.sciencedirect.com/science/article/pii/S2095268614000469>. Special Issue on Green Mining.
- [11] Fatemeh Molaei, Elham Rahimi, Hossein Siavoshi, Setareh Ghaychi Afrouz, and Victor Tenorio. A Comprehensive Review on Internet of Things (IoT) and its Implications in the Mining Industry. *American Journal of Engineering and Applied Sciences*, 13(3):499–515, September 2020. doi: 10.3844/ajeassp.2020.499.515. URL <https://hal.science/hal-02940030>.
- [12] William H Schiffbauer. *A testbed for autonomous mining machine experiments*, volume 9198. US Department of the Interior, Bureau of Mines, 1988.

- [13] Hal Sider. Safety and productivity in underground coal mining. *Source: The Review of Economics and Statistics*, 65:225–233, 1983. URL <https://www.jstor.org/stable/1924488>.
- [14] Carlos Magno C. O. Valle, Alexander Kurdas, Edmundo Pozo Fortuni, Saeed Abdolshah, and Sami Haddadin. Real-time imu-based learning: a classification of contact materials. In *2022 IEEE/RSJ International Conference on Intelligent Robots and Systems (IROS)*, pages 1965–1971, 2022. doi: 10.1109/IROS47612.2022.9981139.
- [15] Luciane Agnoletti dos Santos Pedotti, Ricardo Mazza Zago, Mateus Giesbrecht, and Fabiano Fruett. Low-cost mems accelerometer network for rotating machine vibration diagnostics. *IEEE Instrumentation & Measurement Magazine*, 23(7):25–33, 2020. doi: 10.1109/MIM.2020.9234762.
- [16] Joana Duarte, Fernanda Rodrigues, and Jacqueline Castelo Branco. Sensing technology applications in the mining industrya systematic review. *International Journal of Environmental Research and Public Health*, 19(4):2334, 2022.
- [17] Shu-Qing Qian, Ke-Xin Ren, and Zhi Lü. Experimental study of the features of vlf, mf, hf and vhf electromagnetic radiation accompanying rock fracture. *Acta Seismologica Sinica*, 9:447–454, 1996.
- [18] Wen Shao, Xingsheng Li, Yong Sun, Han Huang, and Jinyuan Tang. An experimental study of temperature at the tip of point-attack pick during rock cutting process. *International Journal of Rock Mechanics and Mining Sciences*, 107:39–47, 2018. ISSN 1365-1609. doi: <https://doi.org/10.1016/j.ijrmms.2018.04.044>. URL <https://www.sciencedirect.com/science/article/pii/S1365160917307530>.
- [19] Bing Miao, Yunwang Li, Yinan Guo, Xiusong You, and Shirong Ge. Design and experimental results of a three-dimensional force sensor for shearer cutting pick force monitoring. *Sensors*, 23(23), 2023. ISSN 1424-8220. doi: 10.3390/s23239521. URL <https://www.mdpi.com/1424-8220/23/23/9521>.
- [20] C. Jobes, J. Carr, and J. Ducarme. Evaluation of an advanced proximity detection system for continous mining machines. *International Journal of Applied Engineering Reseach*, 7(6):649–671, 2012.
- [21] J. Bartels, Christopher Jobes, Tim Lutz, and J. Ducarme. Evaluation of work positions used by continuous miner operators in underground coal mines. volume 53, 10 2009. doi: 10.1518/107118109X12524444080792.
- [22] Yaodong Jiang, Yixin Zhao, Hongwei Wang, and Jie Zhu. A review of mechanism and prevention technologies of coal bumps in china. *Journal of rock mechanics and geotechnical engineering (Online)*, 9(1):180–194, 2017. ISSN 1674-7755.
- [23] Mine Safety and Health Administration (MSHA). Niosh mine and mine worker charts. Online, 10 2021. Available: <https://www.cdc.gov/NIOSH-Mining/MMWC>.
- [24] NIOSH. Hierarchy of controls, Jan 2015. URL <https://www.cdc.gov/niosh/topics/hierarchy/default.html>.
- [25] JR Bartels, CC Jobes, JP DuCarme, and TJ Lutz. Evaluation of work positions used by continuous miner operations in underground coal mines. In *Proceedings of the Human Factors and Ergonomics Society*, pages 1622–1626. Human Factors and Ergonomics Society, 2009.
- [26] J. Mitchell. Research into a sensor-based diagnostic maintenance expert system for the hydraulics of a continuous mining machine. In *Conference Record of the 1991 IEEE Industry Applications Society Annual Meeting*, pages 1192–1199 vol.2, 1991. doi: 10.1109/IAS.1991.178014.

- [27] P. T. Bissert, JL Carr, and JP Ducarme. Proximity detection zones: Deisigns to prevent fatalities around continous mining machines. *Professional safety*, 61(6):72–77, 2016.
- [28] Laxman S Sundae. *Measurement of coal-cutting forces underground with the in-seam tester*, volume 9033. US Department of the Interior, Bureau of Mines, Wachington, DC, 1985.
- [29] Donna L. Anderson. Laser tracking and tram control of a continuous mining machine. *Report of investigations (United States. Bureau of Mines)*, 9319, 1990. URL <https://stacks.cdc.gov/view/cdc/10570>.
- [30] M. J. Pazuchanics and Gary L. Mowrey. Recent progress in discriminating between coal cutting and rock cutting with adaptive signal processing techniques. *Report of investigations (United States. Bureau of Mines)*, 9475, 1993. URL <https://stacks.cdc.gov/view/cdc/10218>.
- [31] David Myers. Predicting mining machine cutting tool wear using neural networks, 1999. URL <http://hdl.handle.net/10388/11756>.
- [32] Hou-Lun Warren Shen. *Acoustic emission potential for monitoring cutting and breakage characteristics of coal*. The Pennsylvania State University, 1996.
- [33] Benjamin Hopkins Miller. Smartbit: in-situ bit/rock interface monitoring device, 2003. URL <http://hdl.handle.net/11124/170545>.
- [34] Witold Biay, Jiri Fries, and Greg Galecki. Determination of coal cutting forces using the cutting head of pou-bw/01-wap device. *Multidisciplinary Aspects of Production Engineering*, 4(1):281–289, 2021. doi: doi:10.2478/mape-2021-0025. URL <https://doi.org/10.2478/mape-2021-0025>.
- [35] *Utilizing Linear Cutting Machine Test for Estimating Cutting Force via Intact Rock Properties*, volume All Days of U.S. Rock Mechanics/Geomechanics Symposium, 06 2021. ARMA-2021-1108.
- [36] Yutaka Sasaki et al. The truth of the f-measure. *Teach tutor mater*, 1(5):1–5, 2007.
- [37] David MW Powers. Evaluation: from precision, recall and f-measure to roc, informedness, markedness and correlation. *arXiv preprint arXiv:2010.16061*, 2020.
- [38] Robert Teale. The concept of specific energy in rock drilling. In *International journal of rock mechanics and mining sciences & geomechanics abstracts*, volume 2, pages 57–73. Elsevier, 1965.
- [39] Nikita Klyuchnikov, Alexey Zaytsev, Arseniy Gruzdev, Georgiy Ovchinnikov, Ksenia Antipova, Leyla Ismailova, Ekaterina Muravleva, Evgeny Burnaev, Artyom Semenikhin, Alexey Cherepanov, et al. Data-driven model for the identification of the rock type at a drilling bit. *Journal of Petroleum science and Engineering*, 178:506–516, 2019.
- [40] Miho Klaic, Zrinka Murat, Tomislav Staroveski, and Danko Brezak. Tool wear monitoring in rock drilling applications using vibration signals. *Wear*, 408:222–227, 2018.
- [41] Issam Abu-Mahfouz. Drilling wear detection and classification using vibration signals and artificial neural network. *International Journal of Machine Tools and Manufacture*, 43(7):707–720, 2003.
- [42] Xu Tao and Feng Zhigang. Tool wear identifying based on emd and svm with ae sensor. In *2009 9th International Conference on Electronic Measurement & Instruments*, pages 2–948. IEEE, 2009.
- [43] Xu Tao and Wang Tao. Cutting tool wear identification based on wavelet package and svm. In *2010 8th World Congress on Intelligent Control and Automation*, pages 5953–5957. IEEE, 2010.

- [44] Liping Liu, Feng Wu, Chunliang Qi, Tianshu Liu, and Jing Tian. High frequency vibration analysis in drilling of gfrp laminates using candlestick drills. *Composite Structures*, 184:742–758, 2018.
- [45] Peng Nie, Zhengqiang Li, Yanchun Liu, Xinyu Liu, and Hongyao Xu. Study on identification method of tool wear based on singular spectrum analysis and support vector machine. In *2011 Second International Conference on Digital Manufacturing & Automation*, pages 1164–1167. IEEE, 2011.
- [46] Yiqiu Qian, Jia Tian, Libing Liu, Yu Zhang, and Yingshu Chen. A tool wear predictive model based on svm. In *2010 Chinese control and decision conference*, pages 1213–1217. IEEE, 2010.
- [47] Manel Martínez Ramón, Thomas Atwood, Silvio Barbin, and Christos G Christodoulou. Signal classification with an svm-fft approach for feature extraction in cognitive radio. In *2009 SBMO/IEEE MTT-S International Microwave and Optoelectronics Conference (IMOC)*, pages 286–289. IEEE, 2009.
- [48] Chih-Chung Chang and Chih-Jen Lin. Libsvm: a library for support vector machines. *ACM transactions on intelligent systems and technology (TIST)*, 2(3):1–27, 2011.
- [49] John C. Platt. Probabilistic outputs for support vector machines and comparisons to regularized likelihood methods. In *ADVANCES IN LARGE MARGIN CLASSIFIERS*, pages 61–74. MIT Press, 1999.
- [50] Sayan Mukherjee, Edgar Osuna, and Federico Girosi. Nonlinear prediction of chaotic time series using support vector machines. In *Neural Networks for Signal Processing VII. Proceedings of the 1997 IEEE Signal Processing Society Workshop*, pages 511–520. IEEE, 1997.
- [51] Jie Sun, Geok Soon Hong, Mustafizur Rahman, and YS Wong. The application of nonstandard support vector machine in tool condition monitoring system. In *Proceedings. DELTA 2004. Second IEEE International Workshop on Electronic Design, Test and Applications*, pages 295–300. IEEE, 2004.
- [52] Hongzhi Hu, Chang Qin, Fang Guan, and Haitao Su. A tool wear monitoring method based on woa and knn for small-deep hole drilling. In *2021 International Symposium on Computer Technology and Information Science (ISCTIS)*, pages 284–287, 2021. doi: 10.1109/ISCTIS51085.2021.00065.
- [53] Jeng-Fung Chen, Shih-Kuei Lo, and Quang Hung Do. An approach to the classification of cutting vibration on machine tools. *Information*, 7(1), 2016. ISSN 2078-2489. doi: 10.3390/info7010007. URL <https://www.mdpi.com/2078-2489/7/1/7>.
- [54] Alex J Smola and Bernhard Schölkopf. A tutorial on support vector regression. *Statistics and computing*, 14(3):199–222, 2004.
- [55] Rui Kong and Bing Zhang. Autocorrelation kernel functions for support vector machines. In *Third International Conference on Natural Computation (ICNC 2007)*, volume 1, pages 512–516. IEEE, 2007.
- [56] Ajit Tamhane and Dunlop Dunlop. Statistics and data analysis: from elementary to intermediate. page 280, 2000.
- [57] Dong-Hyuk Lee, Uikyum Kim, Hosang Jung, and Hyouk Ryeol Choi. A capacitive-type novel six-axis force/torque sensor for robotic applications. *IEEE Sensors Journal*, 16(8):2290–2299, 2016. doi: 10.1109/JSEN.2015.2504267.

- [58] Andrea Bodini, Stefano Pandini, Emilio Sardini, and Mauro Serpelloni. Design and fabrication of a flexible capacitive coplanar force sensor for biomedical applications. In *2018 IEEE Sensors Applications Symposium (SAS)*, pages 1–5, 2018. doi: 10.1109/SAS.2018.8336775.
- [59] Hyung-Kew Lee, Jaehoon Chung, Sun-Il Chang, and Euisik Yoon. Normal and shear force measurement using a flexible polymer tactile sensor with embedded multiple capacitors. *Journal of Microelectromechanical Systems*, 17(4):934–942, 2008. doi: 10.1109/JMEMS.2008.921727.
- [60] Kaspar Willam. Constitutive models for engineering materials. *Encyclopedia of physical science and technology*, 3:603–633, 2002.
- [61] Gianluca Barile, Alfiero Leoni, and Giuseppe Fern. A differential capacitive multi-material 3d printed sensor for portable anemometric applications. In *2019 IEEE 8th International Workshop on Advances in Sensors and Interfaces (IWASI)*, pages 234–238, 2019. doi: 10.1109/IWASI.2019.8791283.
- [62] Yunfeng Lu, Yang Bai, Tao Zeng, Zhengkun Li, Zhonghua Zhang, and Jiubin Tan. Coplanar capacitive sensor for measuring horizontal displacement in joule balance. In *2016 Conference on Precision Electromagnetic Measurements (CPEM 2016)*, pages 1–2, 2016. doi: 10.1109/CPEM.2016.7540791.
- [63] Ievgen O. Zaitsev and Anatolii S. Levytskyi. Determination of response characteristic of capacitive coplanar air gap sensor. In *2017 IEEE Microwaves, Radar and Remote Sensing Symposium (MRRS)*, pages 85–88, 2017. doi: 10.1109/MRRS.2017.8075034.
- [64] Gaurav Prit, Prateek Goyal, and Tarikul Islam. A novel design of the parallel plate capacitive sensor for displacement measurement. In *2019 IEEE 16th India Council International Conference (INDICON)*, pages 1–4, 2019. doi: 10.1109/INDICON47234.2019.9029007.
- [65] Xiaokang Liu, Kai Peng, Ziran Chen, Hongji Pu, and Zhicheng Yu. A new capacitive displacement sensor with nanometer accuracy and long range. *IEEE Sensors Journal*, 16(8):2306–2316, 2016. doi: 10.1109/JSEN.2016.2521681.
- [66] Martijn Schouten, Remco Sanders, and Gijs Krijnen. 3d printed flexible capacitive force sensor with a simple micro-controller based readout. In *2017 IEEE SENSORS*, pages 1–3, 2017. doi: 10.1109/ICSENS.2017.8233949.
- [67] Gerjan Wolterink, Remco Sanders, and Gijs Krijnen. Thin, flexible, capacitive force sensors based on anisotropy in 3d-printed structures. In *2018 IEEE SENSORS*, pages 1–4, 2018. doi: 10.1109/ICSENS.2018.8589584.
- [68] Ryan van Dommelen, Julien Berger, Rubaiyet I. Haque, Marco R. Binelli, Gilberto de Freitas Siqueira, Andr R. Studart, and Danick Briand. Fully 3d printed mechanical pressure sensors: A comparison of sensing mechanisms. In *2020 IEEE SENSORS*, pages 1–4, 2020. doi: 10.1109/SENSORS47125.2020.9278862.
- [69] Milica Kisi, Nelu Bla, Ljiljana ivanov, and Mirjana Damnjanovi. Capacitive force sensor fabricated in additive technology. In *2019 42nd International Spring Seminar on Electronics Technology (ISSE)*, pages 1–5, 2019. doi: 10.1109/ISSE.2019.8810154.
- [70] Saleem Khan, Leandro Lorenzelli, and Ravinder S. Dahiya. Technologies for printing sensors and electronics over large flexible substrates: A review. *IEEE Sensors Journal*, 15(6):3164–3185, 2015. doi: 10.1109/JSEN.2014.2375203.

- [71] P.K. Valavala, T.C. Clancy, G.M. Odegard, and T.S. Gates. Nonlinear multiscale modeling of polymer materials. *International Journal of Solids and Structures*, 44(3):1161–1179, 2007. ISSN 0020-7683. doi: <https://doi.org/10.1016/j.ijsolstr.2006.06.011>. URL <https://www.sciencedirect.com/science/article/pii/S0020768306002198>.
- [72] Buwaneth Y. Dharmadasa, Matthew McCallum, and Francisco Lopez Jimenez. *Characterizing and modeling the viscoplastic behavior of creases in Kapton polyimide films*. doi: 10.2514/6.2020-2165. URL <https://arc.aiaa.org/doi/abs/10.2514/6.2020-2165>.
- [73] Hongzhou Li, Jialian Chen, Qinghua Chen, and Ming Liu. Determining the constitutive behavior of nonlinear visco-elastic-plastic pmma thin films using nanoindentation and finite element simulation. *Materials & Design*, 197:109239, 2021.
- [74] Wei He, Philippe Goudeau, Eric Le Bourhis, Pierre-Olivier Renault, Jean Christophe Dupré, Pascal Doumalin, and Shibin Wang. Study on young's modulus of thin films on kapton by microtensile testing combined with dual dic system. *Surface and Coatings Technology*, 308:273–279, 2016.
- [75] Yuemin Wang, Lei Shang, Panpan Zhang, Xiangqiao Yan, Ke Zhang, Shuliang Dou, Jiupeng Zhao, and Yao Li. Measurement of viscoelastic properties for polymers by nanoindentation. *Polymer Testing*, 83:106353, 2020.
- [76] Wen-Yang Chang, Te-Hua Fang, and Yu-Cheng Lin. Physical characteristics of polyimide films for flexible sensors. *Applied Physics A*, 92(3):693–701, 2008.
- [77] Pal Jen Wei, Wei Xin Shen, and Jen Fin Lin. Analysis and modeling for time-dependent behavior of polymers exhibited in nanoindentation tests. *Journal of non-crystalline solids*, 354(33):3911–3918, 2008.
- [78] Yuchao Zhu, Yigen Wu, Guangshun Wang, Zhongbao Wang, Qiulin Tan, Libo Zhao, and Dezhi Wu. A flexible capacitive pressure sensor based on an electrospun polyimide nanofiber membrane. *Organic Electronics*, 84:105759, 2020. ISSN 1566-1199. doi: <https://doi.org/10.1016/j.orgel.2020.105759>. URL <https://www.sciencedirect.com/science/article/pii/S1566119920301452>.
- [79] Jagoda A Dobrzynska and Martin AM Gijs. Flexible polyimide-based force sensor. *Sensors and Actuators A: Physical*, 173(1):127–135, 2012.
- [80] Andrea Bodini, Stefano Pandini, Emilio Sardini, and Mauro Serpelloni. Design and fabrication of a flexible capacitive coplanar force sensor for biomedical applications. In *2018 IEEE Sensors Applications Symposium (SAS)*, pages 1–5, 2018. doi: 10.1109/SAS.2018.8336775.
- [81] M. Sari, H. S.B. Duzgun, C. Karpuz, and A. S. Selcuk. Accident analysis of two turkish underground coal mines. *Safety Science*, 42:675–690, 2004. ISSN 09257535. doi: 10.1016/j.ssci.2003.11.002.
- [82] Iknur Erol. Investigation of occupational noise-induced hearing loss of underground coal mines. *Mining, Metallurgy and Exploration*, 39:1045–1060, 6 2022. ISSN 25243470. doi: 10.1007/s42461-022-00585-1.
- [83] Jay F Colinet. The impact of black lung and a methodology for controlling respirable dust. doi: 10.1007/s42461-020-00278-7/Published. URL <https://doi.org/10.1007/s42461-020-00278-7>.
- [84] A. Juganda, H. Pinheiro, F. Wilson, N. Sandoval, G. E. Bogin, and J. F. Brune. Investigation of explosion hazard in longwall coal mines by combining cfd with a 1/40th-scale physical model. *Mining, Metallurgy and Exploration*, 39:2273–2290, 10 2022. ISSN 25243470. doi: 10.1007/s42461-022-00629-6.

- [85] Ibrahim Cinar and Hakan Ozsen. Investigation of climatic conditions in underground coal mining. *Mining, Metallurgy and Exploration*, 37:753–760, 4 2020. ISSN 25243470. doi: 10.1007/s42461-019-00141-4.
- [86] Aleksandar D. Bugarski, Shawn Vanderslice, Jon A. Hummer, Teresa Barone, Steven E. Mischler, Shad Peters, Steve Cochrane, and Jared Winkler. Diesel aerosols in an underground coal mine. *Mining, Metallurgy and Exploration*, 39:937–945, 6 2022. ISSN 25243470. doi: 10.1007/s42461-022-00588-y.
- [87] La Tasha R. Swanson and Jennica L. Bellanca. If the technology fits: an evaluation of mobile proximity detection systems in underground coal mines. *Mining, Metallurgy and Exploration*, 36: 633–645, 8 2019. ISSN 25243470. doi: 10.1007/s42461-019-0056-8.
- [88] J. R. Bartels, C. C. Jobes, J. P. Ducarme, and T. J. Lutz. Evaluation of work positions used by continuous miner operators in underground coal mines. *Proceedings of the Human Factors and Ergonomics Society*, 3:1622–1626, 2009. ISSN 10711813. doi: 10.1518/107118109x12524444080792.
- [89] Cem Sensogut, Yaar Kasap, and Ozer Oren. Investigation of work accidents in underground and surface coal mining activities of western lignite corporation by data envelopment analysis (dea). *Mining Metallurgy and Exploration*, 38:1973–1983, 2021. doi: 10.1007/s42461-021-00448-1/Published. URL <http://www.gli.gov.tr>.
- [90] V. Zakeri and A. J. Hodgson. Classifying hard and soft bone tissues using drilling sounds. In *Proceedings of the Annual International Conference of the IEEE Engineering in Medicine and Biology Society, EMBS*, pages 2855–2858, 9 2017. doi: 10.1109/EMBC.2017.8037452.
- [91] Z. W. Zhong, J. H. Zhou, and Ye Nyi Win. Correlation analysis of cutting force and acoustic emission signals for tool condition monitoring. In *2013 9th Asian Control Conference, ASCC 2013*, 2013. ISBN 9781467357692. doi: 10.1109/ASCC.2013.6606333.
- [92] Javad Soltani Rad, Youmin Zhang, Fatemeh Aghazadeh, and Zezhong Chevy Chen. A study on tool wear monitoring using time-frequency transformation techniques. In *Proceedings of the 2014 International Conference on Innovative Design and Manufacturing, ICIDM 2014*, pages 342–347, 9 2014. ISBN 9781479962709. doi: 10.1109/IDAM.2014.6912718.
- [93] Vahid Zakeri, Siamak Arzanpour, and Babak Chehroudi. Discrimination of tooth layers and dental restorative materials using cutting sounds. *IEEE Journal of Biomedical and Health Informatics*, 19: 571–580, 3 2015. ISSN 21682208. doi: 10.1109/JBHI.2014.2317503.
- [94] C. C. Tan. Monitoring of tool wear using acoustic emission. In *Singapore International Conference on Intelligent Control and Instrumentation - Proceedings*, volume 2, pages 1063–1067, 1992. ISBN 0780306325. doi: 10.1109/SICICI.1992.637686.
- [95] Sunilkumar Kakade, L. Vijayaraghavan, and R. Krishnamurthy. Monitoring of tool status using intelligent acoustic emission sensing and decision based neural network. In *IEEE/IAS International Conference on Industrial Automation and Control, Proceedings*, pages 25–29, 1995. doi: 10.1109/iacc.1995.465873.
- [96] Liyu Xu and Yuanjun Zhou. Fault diagnosis for bldcm system used fft algorithm and support vector machines. In *2016 IEEE International Conference on Aircraft Utility Systems (AUS)*, pages 384–387, 2016. doi: 10.1109/AUS.2016.7748079.
- [97] Qingbo He. Vibration signal classification by wavelet packet energy flow manifold learning. *Journal of Sound and Vibration*, 332(7):1881–1894, 2013.

- [98] Hosseini Sadegh, Ahmadi Najafabadi Mehdi, and Akhlaghi Mehdi. Classification of acoustic emission signals generated from journal bearing at different lubrication conditions based on wavelet analysis in combination with artificial neural network and genetic algorithm. *Tribology International*, 95: 426–434, 2016.
- [99] Abhilash Skariah, R Pradeep, R Rejith, and CR Bijudas. Health monitoring of rolling element bearings using improved wavelet cross spectrum technique and support vector machines. *Tribology International*, 154:106650, 2021.
- [100] Tao Xu and Zhigang Feng. Tool wear identifying based on emd and svm with ae sensor. In *ICEMI 2009 - Proceedings of 9th International Conference on Electronic Measurement and Instruments*, pages 2948–2952, 2009. ISBN 9781424438624. doi: 10.1109/ICEMI.2009.5274425.
- [101] Peng Nie, Hongyao Xu, Yanchun Liu, Xinyu Liu, and Zhengqiang Li. Aviation tool wear states identifying based on emd and svm. In *Proceedings of the 2011 2nd International Conference on Digital Manufacturing and Automation, ICDMA 2011*, pages 246–249, 2011. ISBN 9780769544557. doi: 10.1109/ICDMA.2011.67.
- [102] Shuai Shao Zhan, Huang Min, and Yan Le. Using emd to extract characteristic values of the tool vibration signals. In *Proceedings - 2014 6th International Conference on Measuring Technology and Mechatronics Automation, ICMTMA 2014*, pages 799–802, 2014. doi: 10.1109/ICMTMA.2014.197.
- [103] Liyu Xu and Yuanjun Zhou. Fault diagnosis for bldem system used fft algorithm and support vector machines. In *IEEE/CSAA AUS 2016 : 2016 IEEE/CSAA International Conference on Aircraft Utility Systems*, 10 2016. ISBN 9781509010875. doi: 10.1109/AUS.2016.7748079.
- [104] Pramudyana Agus Harlianto, Noor Akhmad Setiawan, and Teguh Bharata Adji. Combining support vector machine - fast fourier transform (svm - fft) for improving accuracy on broken bearing diagnosis. In *2022 5th International Seminar on Research of Information Technology and Intelligent Systems, ISRITI 2022*, pages 576–581, 2022. ISBN 9781665455121. doi: 10.1109/ISRITI56927.2022.10052801.
- [105] G.Y. Yen and Kuo-Chung Lin. Wavelet packet feature extraction for vibration monitoring. In *Proceedings of the 1999 IEEE International Conference on Control Applications (Cat. No.99CH36328)*, volume 2, pages 1573–1578, 1999. ISBN 0-7803-5446-X. doi: 10.1109/CCA.1999.801206. URL <http://ieeexplore.ieee.org/document/801206/>.
- [106] D. Baccar and D. Sffker. Wear detection by means of wavelet-based acoustic emission analysis. *Mechanical Systems and Signal Processing*, 60:198–207, 8 2015. ISSN 10961216. doi: 10.1016/j.ymssp.2015.02.012.
- [107] Muthu Vinayak Thyagarajan and Jamal Rostami. Study of cutting forces acting on a disc cutter and impact of variable penetration measured by full scale linear cutting tests. *International Journal of Rock Mechanics and Mining Sciences*, 175:105675, 2024. ISSN 1365-1609. doi: <https://doi.org/10.1016/j.ijrmms.2024.105675>. URL <https://www.sciencedirect.com/science/article/pii/S1365160924000406>.
- [108] KM Muraleedhara Prabhu. *Window functions and their applications in signal processing*. Taylor & Francis, 6000 Broken Sound Parkway NW, Suite 300, Boca Raton, FL 33487-2742, 2014. doi: 10.1201/9781315216386. URL <https://library.oapen.org/handle/20.500.12657/41686>.

- [109] Cyril Goutte and Eric Gaussier. A probabilistic interpretation of precision, recall and f-score, with implication for evaluation. In David E. Losada and Juan M. Fernández-Luna, editors, *Advances in Information Retrieval*, pages 345–359, Berlin, Heidelberg, 2005. Springer Berlin Heidelberg. ISBN 978-3-540-31865-1. doi: 10.1007/978-3-540-31865-1\_25.
- [110] Max Bramer. chapter Measuring the Performance of a Classifier, pages 173–185. Springer London, London, 2007. ISBN 978-1-84628-766-4. doi: 10.1007/978-1-84628-766-4\_11. URL [https://doi.org/10.1007/978-1-84628-766-4\\_11](https://doi.org/10.1007/978-1-84628-766-4_11).
- [111] Fredric J. Harris. On the use of windows for harmonic analysis with the discrete fourier transform. *Proceedings of the IEEE*, 66:51–83, 1978. ISSN 15582256. doi: 10.1109/PROC.1978.10837.
- [112] Ajit C. Tamhane and Dorothy D. Dunlop. *Statistics and Data Analysis from Elementary to Intermediate*. Prentice-Hall Inc., Upper Saddle River, NJ 07458, 2000.
- [113] Fabian Pedregosa, Gaël Varoquaux, Alexandre Gramfort, Vincent Michel, Bertrand Thirion, Olivier Grisel, Mathieu Blondel, Peter Prettenhofer, Ron Weiss, Vincent Dubourg, Jake Vanderplas, Alexandre Passos, David Cournapeau, Matthieu Brucher, Matthieu Perrot, and Édouard Duchesnay. Scikit-learn: Machine learning in python. *Journal of Machine Learning Research*, 12(85):2825–2830, 2011. URL <http://jmlr.org/papers/v12/pedregosa11a.html>.
- [114] Michael Buckland and Fredric Gey. The relationship between recall and precision. *Journal of the American Society for Information Science*, 45(1):12–19, 1994. doi: [https://doi.org/10.1002/\(SICI\)1097-4571\(199401\)45:1<12::AID-ASI2>3.0.CO;2-L](https://doi.org/10.1002/(SICI)1097-4571(199401)45:1<12::AID-ASI2>3.0.CO;2-L).
- [115] M.P. Vaishnnave, K. Suganya Devi, P. Srinivasan, and G. Arut Perum Jothi. Detection and classification of groundnut leaf diseases using knn classifier. In *2019 IEEE International Conference on System, Computation, Automation and Networking (ICSCAN)*, pages 1–5, 2019. doi: 10.1109/ICSCAN.2019.8878733.
- [116] Yang Song, Jian Huang, Ding Zhou, Hongyuan Zha, and C. Lee Giles. Iknna: Informative k-nearest neighbor pattern classification. In *Knowledge Discovery in Databases: PKDD 2007*, pages 248–264, Berlin, Heidelberg, 2007. Springer Berlin Heidelberg. ISBN 978-3-540-74976-9.
- [117] Haneen Arafat Abu Alfeilat, Ahmad B.A. Hassanat, Omar Lasassmeh, Ahmad S. Tarawneh, Mahmoud Bashir Alhasanat, Hamzeh S. Eyal Salman, and V.B. Surya Prasath. Effects of distance measure choice on k-nearest neighbor classifier performance: A review. *Big Data*, 7(4):221–248, 2019. doi: 10.1089/big.2018.0175. PMID: 31411491.
- [118] Aleksandar Lazarevic, Dragoljub Pokrajac, Aristides Marcano, and Noureddine Melikechi. Support vector machine based classification of fast Fourier transform spectroscopy of proteins. In Anita Mahadevan-Jansen, Tuan Vo-Dinh, and Warren S. Grundfest M.D., editors, *Advanced Biomedical and Clinical Diagnostic Systems VII*, volume 7169, page 71690C, San Jose, California, 2009. International Society for Optics and Photonics, SPIE. doi: 10.1117/12.809964.
- [119] Martin Sewell. Structural risk minimization. In *Unpublished Ph. D. dissertation, University College London, Department of Computer Science*, 2008. URL <https://api.semanticscholar.org/CorpusID:2425385>.
- [120] Kenneth Lange. *Karush-Kuhn-Tucker Theory*, pages 107–135. Springer New York, New York, NY, 2013. ISBN 978-1-4614-5838-8. doi: 10.1007/978-1-4614-5838-8\_5.

- [121] Mohammadreza Asghari Oskoei and Huosheng Hu. Support vector machine-based classification scheme for myoelectric control applied to upper limb. *IEEE Transactions on Biomedical Engineering*, 55(8):1956–1965, 2008. doi: 10.1109/TBME.2008.919734.
- [122] Rameswar Debnath, N. Takahide, and Haruhisa Takahashi. A decision based one-against-one method for multi-class support vector machine. *Pattern Anal. Appl.*, 7:164–175, 07 2004. doi: 10.1007/s10044-004-0213-6.
- [123] Intan Nurma Yulita, Rudi Rosadi, Sri Purwani, and Mira Suryani. Multi-layer perceptron for sleep stage classification. *Journal of Physics: Conference Series*, 1028(1):012212, jun 2018. doi: 10.1088/1742-6596/1028/1/012212. URL <https://dx.doi.org/10.1088/1742-6596/1028/1/012212>.
- [124] Diego Molina Estren, Alexis De la Hoz Manotas, and Fabio Mendoza. Classification and features selection method for obesity level prediction. *Journal of Theoretical and Applied Information Technology*, 99:2525, 06 2021.
- [125] Osval Antonio Montesinos López, Abelardo Montesinos López, and Jose Crossa. *Fundamentals of Artificial Neural Networks and Deep Learning*, pages 379–425. Springer International Publishing, Cham, 2022. ISBN 978-3-030-89010-0. doi: 10.1007/978-3-030-89010-0\_10.
- [126] Siddharth Sharma, Simone Sharma, and Anidhya Athaiya. Activation functions in neural networks. *International Journal of Engineering Applied Sciences and Technology*, 04:310–316, 05 2020. doi: 10.33564/IJEAST.2020.v04i12.054.
- [127] Andrew Maxwell, Runzhi Li, Bei Yang, Heng Weng, Aihua Ou, Huixiao Hong, Zhaoxian Zhou, Ping Gong, and Chaoyang Zhang. Deep learning architectures for multi-label classification of intelligent health risk prediction. *BMC bioinformatics*, 18 (Suppl 14):121–131, 12 2017. doi: <https://doi.org/10.1186/s12859-017-1898-z>.
- [128] Vivek V. Khanzode, J. Maiti, and P. K. Ray. A methodology for evaluation and monitoring of recurring hazards in underground coal mining. *Safety Science*, 49:1172–1179, 10 2011. ISSN 09257535. doi: 10.1016/j.ssci.2011.03.009.
- [129] Joseph H. Saleh and Amy M. Cummings. Safety in the mining industry and the unfinished legacy of mining accidents: Safety levers and defense-in-depth for addressing mining hazards. *Safety Science*, 49:764–777, 7 2011. ISSN 09257535. doi: 10.1016/j.ssci.2011.02.017.
- [130] Michael R. Betz, Mark D. Partridge, Michael Farren, and Linda Lobao. Coal mining, economic development, and the natural resources curse. *Energy Economics*, 50:105–116, 7 2015. ISSN 01409883. doi: 10.1016/j.eneco.2015.04.005.
- [131] FRED Federal Reserve Bank of St. Louis. U.s. bureau of labor statistics, all employees, coal mining [ceu1021210001]. <https://fred.stlouisfed.org/series/CEU1021210001>, 2023.
- [132] R. Teale. The concept of specific energy in rock drilling. *International Journal of Rock Mechanics and Mining Sciences and Geomechanics Abstracts*, 2(1):57–73, 1965. ISSN 0148-9062. doi: [https://doi.org/10.1016/0148-9062\(65\)90022-7](https://doi.org/10.1016/0148-9062(65)90022-7). URL <https://www.sciencedirect.com/science/article/pii/0148906265900227>.
- [133] Austin F Oltmanns and Andrew J Petruska. Low-profile capacitive load cells for underground mining material and wear classification to promote worker safety. *Mining, Metallurgy & Exploration*, 40(3):757–771, 2023.

- [134] Tian Shu, Jiyang Qiao, and Fan Ping. Study on preventing override trip system under coal mine electric network based on can bus. *Proceedings - 2010 International Conference on Intelligent System Design and Engineering Application, ISDEA 2010*, 2:467–470, 2010. doi: 10.1109/ISDEA.2010.200.
- [135] Yunlong Ma. Design of coal mine power grid parameter monitoring system based on can bus. *IOP Conference Series: Earth and Environmental Science*, 651, 2 2021. ISSN 17551315. doi: 10.1088/1755-1315/651/3/032009.
- [136] Qingliang Zeng, Zhiwen Wang, Zhenguo Lu, Lirong Wan, Zhihai Liu, and Xin Zhang. Research on cutting performance and fatigue life of conical pick in cutting rock process. *Science Progress*, 104, 10 2021. ISSN 20477163. doi: 10.1177/00368504211050293.
- [137] Qiuxia Fan, Chongxue Chen, Qianqian Zhang, and Guirong Liu. A dynamic analysis of a conical pick during rock-cutting process based on the smooth finite element method. *Wear*, 512-513, 1 2023. ISSN 00431648. doi: 10.1016/j.wear.2022.204523.
- [138] F F Roxborough, F I E Min, M I M ” Aus, P Kingt, C Eng, and E J Pedroncelli. Tests on the cutting performance of a continuous miner. *Journal of the South African Institute of Mining and Metallurgy*, pages 9–25, 1 1981.
- [139] N. Bilgin, M. A. Demircin, H. Copur, C. Balci, H. Tuncdemir, and N. Akcin. Dominant rock properties affecting the performance of conical picks and the comparison of some experimental and theoretical results. *International Journal of Rock Mechanics and Mining Sciences*, 43:139–156, 2006. ISSN 13651609. doi: 10.1016/j.ijrmms.2005.04.009.
- [140] Hajime Ikeda, Oluwafemi Kolade, Muhammad Ahsan Mahboob, Frederick Thomas Cawood, and Youhei Kawamura. Communication of sensor data in underground mining environments: An evaluation of wireless signal quality over distance. *Mining*, 1:211–223, 9 2021. doi: 10.3390/mining1020014.
- [141] Fabian Seguel, Pablo Palacios-Jativa, Cesar A. Azurdia-Meza, Nicolas Krommenacker, Patrick Charpentier, and Ismael Soto. Underground mine positioning: A review. *IEEE Sensors Journal*, 22: 4755–4771, 3 2022. ISSN 15581748. doi: 10.1109/JSEN.2021.3112547.
- [142] Serhan Yarkan, Sabih Gzelgz, Hseyin Arslan, and Robin Murphy. Underground mine communications: A survey. *IEEE Communications Surveys and Tutorials*, 11:125–142, 2009. ISSN 1553877X. doi: 10.1109/SURV.2009.090309.
- [143] Linus Thrybom, Jonas Neander, Ewa Hansen, and Krister Landerns. Future challenges of positioning in underground mines. In *IFAC-PapersOnLine*, volume 48, pages 222–226, 7 2015. doi: 10.1016/j.ifacol.2015.08.135.
- [144] Alok Ranjan and H B Sahu. Communication challenges in underground mines. *Search and Research*, V:23–29, 2014.
- [145] K G Hurt and K M Macandrew. Cutting efficiency and life of rock-cutting picks. *Mining Science and Technology*, 2:139–151, 1985.
- [146] Okan Su and Muhammet Akka. Assessment of pick wear based on the field performance of two transverse type roadheaders: a case study from amasra coalfield. *Bulletin of Engineering Geology and the Environment*, 79:2499–2512, 7 2020. ISSN 14359537. doi: 10.1007/s10064-019-01712-x.

- [147] Jamal I Rostami, Jamal Rostami, Levent Ozdemir, and David M Neil. Application of heavy duty roadheaders for underground development of the yucca mountain exploratory study facility. *Coal International Mining and Quarry World*, 1 2003. URL <https://www.researchgate.net/publication/268395388>.
- [148] Clayton Cooper, Jianjing Zhang, Robert X. Gao, Peng Wang, and Ihab Ragai. Anomaly detection in milling tools using acoustic signals and generative adversarial networks. *Procedia Manufacturing*, 48: 372–378, 2020. ISSN 2351-9789. doi: <https://doi.org/10.1016/j.promfg.2020.05.059>. URL <https://www.sciencedirect.com/science/article/pii/S2351978920315110>. 48th SME North American Manufacturing Research Conference, NAMRC 48.
- [149] Qing Wang, Chenguang Bi, Jiawei Zhang, Haige Wang, and Zhichuan Guan. Experimental study on downhole acoustic wave propagation characteristics in curved drill string. *Processes*, 11, 5 2023. ISSN 22279717. doi: 10.3390/pr11051525.
- [150] Krzysztof Fuawka, Lech Stolecki, Marcin Szumny, Witold Pytel, Izabela Jakiewicz-Pro, Michel Jaki, Michael Nger, and Philipp Hartlieb. Roof fall hazard monitoring and evaluation state-of-the-art review. *Energies*, 15(21), 2022. ISSN 1996-1073. doi: 10.3390/en15218312. URL <https://www.mdpi.com/1996-1073/15/21/8312>.
- [151] Brent A. Slaker and Khaled M. Mohamed. A practical application of photogrammetry to performing rib characterization measurements in an underground coal mine using a dslr camera. *International Journal of Mining Science and Technology*, 27(1):83–90, 2017. ISSN 2095-2686. doi: <https://doi.org/10.1016/j.ijmst.2016.09.032>. URL <https://www.sciencedirect.com/science/article/pii/S2095268616302105>. SI: Special Issue on Ground Control in Mining in 2016.
- [152] Ali Abdullah M Alzahrani. *Detection of mine roof failure using inexpensive LiDAR technology*. Missouri University of Science and Technology, Missouri, 2017.
- [153] Carl Rod Nave. *HyperPhysics*. Georgia State University, <http://hyperphysics.phy-astr.gsu.edu/hbase/electric/pplate.html>, 2024.
- [154] Benjamin Reichert and Zoran Ristivojevic. Analytical results for the capacitance of a circular plate capacitor. *Physical Review Research*, 2, 3 2020. ISSN 26431564. doi: 10.1103/PhysRevResearch.2.013289.
- [155] Jagoda A. Dobrzynska and Martin A.M. Gijs. Flexible polyimide-based force sensor. *Sensors and Actuators, A: Physical*, 173:127–135, 1 2012. ISSN 09244247. doi: 10.1016/j.sna.2011.11.006.
- [156] Yuchao Zhu, Yigen Wu, Guangshun Wang, Zhongbao Wang, Qiulin Tan, Libo Zhao, and Dezhi Wu. A flexible capacitive pressure sensor based on an electrospun polyimide nanofiber membrane. *Organic Electronics*, 84, 9 2020. ISSN 15661199. doi: 10.1016/j.orgel.2020.105759.
- [157] Yunfeng Lu, Yang Bai, Tao Zeng, Zhengkun Li, Zhonghua Zhang, and Jiubin Tan. Coplanar capacitive sensor for measuring horizontal displacement in joule balance. *CPEM 2016 - Conference on Precision Electromagnetic Measurements, Conference Digest*, 8 2016. doi: 10.1109/CPEM.2016.7540791.
- [158] Ievgen O. Zaitsev and Anatolii S. Levytskyi. Determination rf response characteristic rf capacitive coplanar air gap sensor. *Radar and Remote Sensing Symposium, IEEE Microwaves*, 8 2017.

- [159] Gianluca Barile, Altiero Leoni, and Giuseppe Ferri. A differential capacitive multi-material 3d printed sensor for portable anemometric applications. *IEEE 8th International Workshop on Advances in Sensors and Interfaces (IWASI)*., 2019.
- [160] Nelu Bla, Milica Kisi, Ljiljana ivanov, and Mirjana Damnjanovi. Capacitive sensor with stretchable membrane fabricated by 3d printing for displacement application. In *IEEE EUROCON 2019 -18th International Conference on Smart Technologies*, pages 1–5, 2019. doi: 10.1109/EUROCON.2019.8861960.
- [161] Moojin Kim, Wonkyu Moon, Euisung Yoon, and Kwang ryeol Lee. A new capacitive displacement sensor with high accuracy and long range. In *The 13th International Conference on Solid-State Sensors, Actuators and Microsystems, 2005. Digest of Technical Papers. TRANSDUCERS '05*, volume 1, pages 559–562 Vol. 1, 2005. doi: 10.1109/SENSOR.2005.1496478.
- [162] Xiaokang Liu, Kai Peng, Ziran Chen, Hongji Pu, and Zhicheng Yu. A new capacitive displacement sensor with nanometer accuracy and long range. *IEEE Sensors Journal*, 16:2306–2316, 4 2016. ISSN 1530437X. doi: 10.1109/JSEN.2016.2521681.
- [163] Gaurav Prit, Prateek Goyal, and Tarikul Islam. A novel design of the parallel plate capacitive sensor for displacement measurement. *IEEE 16th India Council International Conference (INDICON)*., 2019.
- [164] James W. Nilsson and Susan A. Riedel. *Electric Circuits*. Pearson Education, Inc, Upper Saddle River, New Jersey, 10 edition, 2015. ISBN 978-0-13-376003-3.
- [165] Dastan Maulud and Adnan M. Abdulazeez. A review on linear regression comprehensive in machine learning. *Journal of Applied Science and Technology Trends*, 1:140–147, 12 2020. doi: 10.38094/jasstt1457.
- [166] Xiaobin Hu, Peifeng Niu, Jianmei Wang, and Xinxin Zhang. A dynamic rectified linear activation units. *IEEE Access*, 7:180409–180416, 2019. ISSN 21693536. doi: 10.1109/ACCESS.2019.2959036.
- [167] Kazuyuki Hara, Daisuke Saito, and Hayaru Shouno. Analysis of function of rectified linear unit used in deep learning. In *2015 International Joint Conference on Neural Networks (IJCNN)*, pages 1–8, 2015. doi: 10.1109/IJCNN.2015.7280578.
- [168] Didier A Girard. A fast 'monte-carlo cross-validation' procedure for large least squares problems with noisy data. *Numer. Math*, 56:1–23, 1989.
- [169] Carlos Catania, Jorge Guerra, Juan Romero, Gabriel Caffaratti, and Martn Marchetta. Beyond random split for assessing statistical model performance. Universidad Nacional de Cuyo. Facultad de Ingenieria. LABSIN. Mendoza. Argentina, 09 2022.
- [170] Christian Janze. Shedding light on the role of sample sizes and splitting proportions in out-of-sample tests: A monte carlo cross-validation approach. *Atas da Conferencia da Associacao Portuguesa de Sistemas de Informacao*, 17:245–259, 2017. ISSN 2183489X. doi: 10.18803/capsi.v17.245-259.
- [171] Joseph F Lucke and Susan Embretson. The biases and mean squared errors of estimators of multinormal squared multiple correlation. *Journal of Educational Statistics Fall*, 9:183–192, 1984.
- [172] Davide Chicco, Matthijs J. Warrens, and Giuseppe Jurman. The coefficient of determination r-squared is more informative than smape, mae, mape, mse and rmse in regression analysis evaluation. *PeerJ Computer Science*, 7:1–24, 2021. ISSN 23765992. doi: 10.7717/PEERJ-CS.623.

- [173] Lesley F Leach and Robin K Henson. The use and impact of adjusted r<sup>2</sup> effects in published regression research. *Multiple Linear Regression Viewpoints*, 33, 2007.
- [174] Joel Tellinghuisen and Carl H. Bolster. Using r<sup>2</sup> to compare least-squares fit models: When it must fail. *Chemometrics and Intelligent Laboratory Systems*, 105:220–222, 2 2011. ISSN 01697439. doi: 10.1016/j.chemolab.2011.01.004.
- [175] William W Rozeboom. Estimation of cross-validated multiple correlation: A clarification. *Psychological Bulletin*, 85(6):1348, 1978.
- [176] Raman Arora, Amitabh Basu, Poorya Mianjy, and Anirbit Mukherjee. Understanding deep neural networks with rectified linear units. *CoRR*, abs/1611.01491, 2016. URL <http://arxiv.org/abs/1611.01491>.
- [177] Shengde ZHANG, Syuhei MORI, Masao SAKANE, Tadashi NAGASAWA, and Kaoru KOBAYASHI. Tensile properties and viscoelastic model of a polyimide film. *Journal of Solid Mechanics and Materials Engineering*, 6(6):668–677, 2012. doi: 10.1299/jmmp.6.668.
- [178] Kilwon Cho, Daeho Lee, Min Soo Lee, and Chan Eon Park. Fracture behaviour of thin polyimide films. *Polymer*, 38(7):1615–1623, 1997. ISSN 0032-3861. doi: [https://doi.org/10.1016/S0032-3861\(96\)00597-6](https://doi.org/10.1016/S0032-3861(96)00597-6). URL <https://www.sciencedirect.com/science/article/pii/S0032386196005976>.
- [179] Yu-Chen Chang, Tz-Cheng Chiu, Yu-Ting Yang, Yi-Hsiu Tseng, Xi-Hong Chen, and Pu-Shan Huang. Fatigue response of polyimide thin film under cyclic loading. In *2015 10th International Microsystems, Packaging, Assembly and Circuits Technology Conference (IMPACT)*, pages 233–236, 2015. doi: 10.1109/IMPACT.2015.7365229.

## APPENDIX A

### LASER WELDING PROCEDURE

To assemble the steel case, a laser welding procedure was used. To determine optimal laser welding properties, a small study was performed. The following test matrix is shown in Table A.1. 12 tests fit on 2 samples, using 6 45 deg arc tests per sample. There is about 90 deg of the sample taken up by the tabs. The OD of the ring is 3.8", giving about 1.5" per test. This is allocated as 1" of test and two 0.25" buffers on either end. The best result was with 400 W and 60 in/min. (1 in./s) lasing. The exact laser welding procedure is listed below. A fixture was constructed to provide the right angles. The case was mounted in a fourth axis via a magnetic holder.

Table A.1 Test matrix for laser welding, 'o': perform test; 'x': test not performed

Power/Speed	40	50	60	70	80 in/.min.
600 W	x	x	o	o	o
500 W	x	o	o	o	o
400 W	o	o	o	x	x
300 W	x	o	o	x	x

Listing A.1: G-Code Programs for laser welder

#### CORNER/OD PROGRAM

```
## Start with laser focused on top corner

G20 G90 # Start , config
M7      # Gas on
<M8> LASER COMMAND, BE CAREFUL
G01 x0.3245 y-0.20 z0 f60  # GOTO B @ 60 in/min
G01 x1.1789 y0 z0          # GOTO C
A270 f1800                  # Rotate 270 @ 1800 deg/min
G01 x2.0333 y-0.20 z0 f60  # GOTO D @ 60 in/min
G01 x2.3578 y0 z0          # GOTO E

M9      # Laser Off
M30      # End
```

#### ID PROGRAM

```
## Place 4th axis fixture and focus on ID
```

```
G20 G90 # Start , config
M7      # Gas on
<M8> LASER COMMAND, BE CAREFUL
A360 f1800 # Do a 360 @ 1800 deg/min
M9
M30
```

## APPENDIX B

### CAPACITANCE SIMULATION

Here we have simulation data for the air gap design. The electric field over a cross section of the electrode floating in space in the steel case is shown in Figure B.1. The static field strength is calculated for the two positions of the case top at no load and max load conditions. The relaxed gap is  $457 \mu\text{m}$ . The inner electrode is  $30 \mu\text{m}$ , and sits  $125 \mu\text{m}$  above the case. The difference in dielectric strength above and below the electrode is ignored for this simulation. For the max load conditions, the total gap is  $200 \mu\text{m}$ .

The simulation points are chosen from the previous load frame characterization data of the sensor case. The simulation covers a 0.1 degree chunk of the entire ring sensor. The results of the simulation indicate that the uncompressed sensor should have a capacitance of  $0.7 \text{ pf}$  per degree of electrode and the fully compressed electrode should have a capacitance of  $1.8 \text{ pf}$  per degree of electrode. This suggests the capacitance could change by at least 2.5 times its initial value over the travel of the sensor.

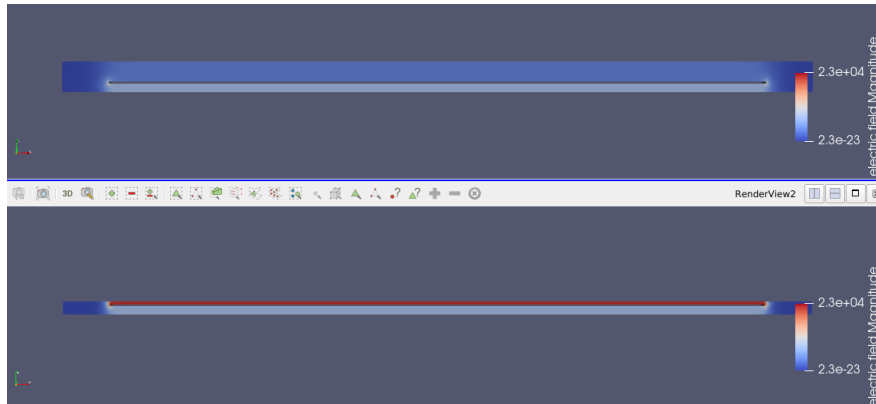


Figure B.1 Simulation of electric field to determine capacitance properties of air gap design. The top image shows the relaxed state of the sensor, with low electric field strength in the free space around the electrode. When the air gap compresses, the electric field becomes much stronger and more concentrated, this is measured as an increase in capacitance. Fringing effects appear to be minimal in this simulation of the design.

## APPENDIX C

### COMPUTER AIDED ANALYTICAL SOLUTIONS

MATLAB was used to solve analytical models for the air gap sensor during the sensor's design. The resulting performance graphs are shown in Figure C.1. The graphs shows performance near the empirically measured value of 10 Newton per Hertz. The model has many parameters, so the uncertainty is collected in the parasitic capacitance and inductance. The overall device stiffness is also adjusted for this model, to a value of 6 GN/m. This limits the strain in the model to the feasible region of the air gap. The equation for Hertz per Newton is found by the script, and is given in C.1. The script and output are given in Listing C.2 and Listing C.3, respectively.

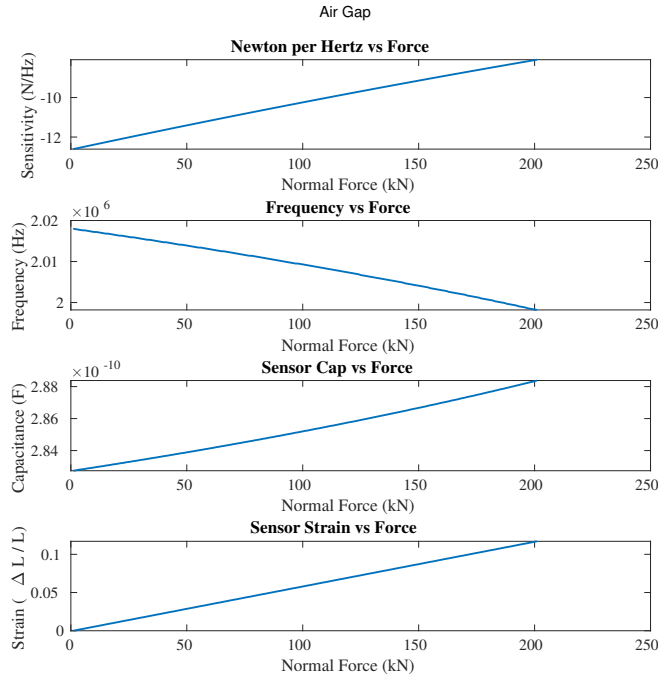


Figure C.1 Result of computation of device frequency and sensitivity over the required input range.

$$\frac{df}{dF} = -\frac{0.0796 A L e_1 e_2^2}{k_s \left( 2.5000e-05 e_1 + e_2 \left( d1n - \frac{F}{k_s} \right) \right)^2 \left( L \left( cb + \frac{A e_2}{d2n} + \frac{A e_1 e_2}{2.5000e-05 e_1 + e_2 \left( d1n - \frac{F}{k_s} \right)} \right) \right)^{1.5000}} \quad (C.1)$$

A model was also used to explore the closed area sensor configuration. The resulting performance graphs are shown in Figure C.2. The sensitivity is much greater for this model, requiring less Newtons to alter the resonant frequency in Hertz when compared to the air gap model. For these calculations, the sensitivity can approach infinity as the region size approaches zero. In reality, the device will continue to get stiffer as it compresses considerably, limiting the compression. The equation for the sensitivity to input force is shown in C.2. The true sensor does not have completely linear characteristics, but the sensitivity increases with greater force. Also, the sensitivity is approximately linear with input force, so the response is roughly proportional to the square of the input force for this configuration. This model does not entirely capture the performance of the sensor during the rock cutting experiment, but agrees with the trend that a more compressed sensor is more sensitive, and it shows sensitivity of similar magnitude. The script and output are given in Listing C.4 and Listing C.5, respectively.

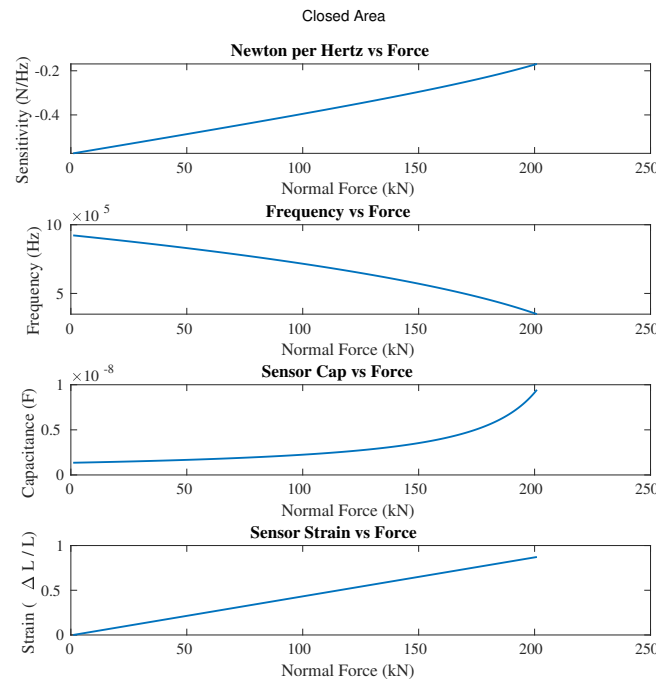


Figure C.2 Result of computation of device frequency and sensitivity over the required input range.

$$\frac{df_{r1}}{dF} = -\frac{0.0796 L \left( \frac{A_e}{k_1 \left( d1n - \frac{F}{k_1} \right)^2} + \frac{A_e}{k_2 \left( d2n - \frac{F}{k_2} \right)^2} \right)}{\left( L \left( cb + \frac{A_e}{d1n - \frac{F}{k_1}} + \frac{A_e}{d2n - \frac{F}{k_2}} \right) \right)^{1.5000}} \quad (C.2)$$

Listing C.2: Script for modelling air gap

```
% This script models the "Air Gap" sensor, while the air gap is present.

syms F f h d d1 d2 d1n d2n kt ks e1 e2 A L cb ce1 ce2 cm
%   F: input force
%   f: resonant frequency
%   h: nominal total sensor height
%   d: total sensor displacement from nominal
%   d1: element 1 (top) displacement from nominal
%   d2: element 2 (bottom) displacement from nominal
%   d1n: nominal distance for top element between electrode and case
%   d2n: nominal distance for bottom element b/w electrode and case
%   kt: total stiffness of sensor
%   ks: stiffness of steel walls
%   kpi1: stiffness of element 1 (top)
%   kp12: stiffness of element 2 (bottom)
%   e1: dielectric permittivity of polyimide+ air gap
%   e2: dielectric permittivity of polyimide (bottom)
%   A: Area of sensing element electrode
%   L: Inductance in sensing circuit
%   cb: base capacitance of sensing circuit
%   ce1: capacitance of element 1 (top)
%   ce2: capacitance of element 2 (bottom)
%   cm: capacitance as measured by circuit

% Total stiffness model, just the steel case and air (k=0)
kt = ks

% Sensor height
h = d1n + d2n

% Sensor deformation model, total displacement from total stiffness
d = F / kt

% Sensor element 1 displacement (same as total)
d1 = d

% Sensor element 2 displacement (static)
d2 = 0

% Sensor capacitance model, between electrode and case, top side
% https://phys.libretexts.org/Bookshelves/Electricity_and_Magnetism/
% Electricity_and_Magnetism_(Tatum)/05%3A_Capacitors/5.14%3A--Mixed-Dielectrics
ce1 = e1 * e2 * A / (e2 * (d1n - d1) + e1 * 0.25e-4)

% Other element, between electrode and case, bottom side
ce2 = e2 * A / (d2n - d2)

% Measured capacitance relation to cap network with parallel env cap
cm = cb + ce1 + ce2

% Sensor resonant frequency model
f = 1 / (2*pi*sqrt(L*cm))

df_dF = simplify(diff(f, F))
display(latex(df_dF))
```

```

A = 3.75e-4
e1 = 8.854e-12 * 1.0 % Air
e2 = 8.854e-12 * 3.2 % PI
d1n = 1.5e-4
d2n = 1.35e-4 % 100um of PI and 25um of soldermask and 10um of super glue
ks = 6.0e9
L = 18e-6 + 4e-6 % Board + estimated parasitic values
cb = 33e-12 + 1.5e-10 % Board + estimated parasitic values
F = [0:1e3:200e3];

cap_values = subs(cm);
freq_values = subs(f);
sensitivity_values = subs(df_dF);
strain_values = subs(d/h);
newtons_per_hertz_sensitivity_values = 1.0 ./ sensitivity_values;

figure();
subplot(4,1,1);
plot(newtons_per_hertz_sensitivity_values);
title("Newton per Hertz vs Force")

subplot(4,1,2);
plot(freq_values);
title("Frequency vs Force")

subplot(4,1,3);
plot(cap_values);
title("Sensor Cap vs Force")

subplot(4,1,4);
plot(strain_values);
title("Sensor Strain vs Force")

sgtitle("Air Gap")

```

Listing C.3: Output from air gap script

```

kt =
ks

h =
d1n + d2n

d =
F/ks

d1 =
F/ks

d2 =
0

ce1 =
(A*e1*e2)/(2.5000e-05*e1 + e2*(d1n - F/ks))

ce2 =
(A*e2)/d2n

cm =
cb + (A*e2)/d2n + (A*e1*e2)/(2.5000e-05*e1 + e2*(d1n - F/ks))

f =
0.1592/(L*(cb + (A*e2)/d2n + (A*e1*e2)/(2.5000e-05*e1 + e2*(d1n - F/ks))))^0.5000

df_dF =
-(0.0796*A*L*e1*e2^2)/(ks*(2.5000e-05*e1 + e2*(d1n - F/ks))^2*(L*(cb + (A*e2)/d2n +
(A*e1*e2)/(2.5000e-05*e1 + e2*(d1n - F/ks))))^1.5000)

A =
3.7500e-04

e1 =
8.8540e-12

e2 =
2.8333e-11

d1n =
1.5000e-04

d2n =
1.3500e-04

ks =
6.0000e+09

L =
2.2000e-05

cb =
1.8300e-10

```

Listing C.4: Script for modelling closed area

```
% This script models the "Air Gap" sensor, after the air gap has been
% crushed out, and both the flexPCB and case deform from the input force.

syms F f h d d1 d2 d1n d2n kt ks kpi1 kpi2 e A L cb ce1 ce2 cm
%   F: input force
%   f: resonant frequency
%   h: nominal total sensor height
%   d: total sensor displacement from nominal
%   d1: element 1 (top) displacement from nominal
%   d2: element 2 (bottom) displacement from nominal
%   d1n: nominal distance for top element between electrode and case
%   d2n: nominal distance for bottom element b/w electrode and case
%   kt: total stiffness of sensor
%   ks: stiffness of steel walls
%   kpi1: stiffness of element 1 (top)
%   kpi2: stiffness of element 2 (bottom)
%   e: dielectric permittivity of polyimide
%   A: Area of sensing element electrode
%   L: Inductance in sensing circuit
%   cb: base capacitance of sensing circuit
%   ce1: capacitance of element 1 (top)
%   ce2: capacitance of element 2 (bottom)
%   cm: capacitance as measured by circuit

% Total stiffness model, sensor case parallel to series polyimide elements
kt = ks + (1/kpi1 + 1/kpi2)^(-1)

% Sensor height
h = d1n + d2n

% Sensor deformation model, total displacement from total stiffness
d = F / kt

% Sensor element 1 displacement
d1 = d / (1 + kpi2/kpi1)

% Sensor element 2 displacement
d2 = d / (1 + kpi1/kpi2)

% Sensor capacitance model, between electrode and case, top side
ce1 = e * A / (d1n - d1)

% Other element, between electrode and case, bottom side
ce2 = e * A / (d2n - d2)

% Measured capacitance relation to cap network with parallel env cap
cm = cb + ce1 + ce2

% Sensor resonant frequency model
f = 1 / (2*pi*sqrt(L*cm))

% Make derivative managable for printing, glob spring constants
% k1 = kt (1 + kpi2/kpi1)
% k2 = kt (1 + kpi1/kpi2)
syms f2 k1 k2
f2 = subs(f, d1, F/k1);
```

```

f2 = subs(f2, d2, F/k2)
df2_dF = simplify(diff(f2, F))
display(latex(df2_dF))

df_dF = simplify(diff(f, F))
display(latex(df_dF))

A = 3.75e-4
e = 8.854e-12 * 3.2
d1n = 0.15e-4
d2n = 0.23e-4 % 100um of PI and 25um of soldermask and 10um of super glue
ks = 6.0e9
kpi1 = 3.0e5 * 2.9e-3 / d1n
kpi2 = 7.0e5 * 2.9e-3 / d2n
L = 18e-6 + 4e-6
cb = 33e-12 + 1.5e-10
F = [0.0:1.0e3:200.0e3];

cap_values = subs(cm);
freq_values = subs(f);
sensitivity_values = subs(df_dF);
strain_values = subs(d/h);
newtons_per_hertz_sensitivity_values = 1.0 ./ sensitivity_values;

figure();
subplot(4,1,1);
plot(newtons_per_hertz_sensitivity_values);
title("Newton per Hertz vs Force")

subplot(4,1,2);
plot(freq_values);
title("Frequency vs Force")

sgtitle("Closed Area")

subplot(4,1,3);
plot(cap_values);
title("Sensor Cap vs Force")

subplot(4,1,4);
plot(strain_values);
title("Sensor Strain vs Force")

```

Listing C.5: Output from closed area script

```

kt =
ks + 1/(1/kpi1 + 1/kpi2)

h =
d1n + d2n

d =
F/(ks + 1/(1/kpi1 + 1/kpi2))

d1 =
F/((ks + 1/(1/kpi1 + 1/kpi2))*(kpi2/kpi1 + 1))

d2 =
F/((ks + 1/(1/kpi1 + 1/kpi2))*(kpi1/kpi2 + 1))

ce1 =
(A*e)/(d1n - F/((ks + 1/(1/kpi1 + 1/kpi2))*(kpi2/kpi1 + 1)))

ce2 =
(A*e)/(d2n - F/((ks + 1/(1/kpi1 + 1/kpi2))*(kpi1/kpi2 + 1)))

cm =
cb + (A*e)/(d1n - F/((ks + 1/(1/kpi1 + 1/kpi2))*(kpi2/kpi1 + 1))) + (A*e)/(d2n - F
/((ks + 1/(1/kpi1 + 1/kpi2))*(kpi1/kpi2 + 1)))

f =
0.1592/(L*(cb + (A*e)/(d1n - F/((ks + 1/(1/kpi1 + 1/kpi2))*(kpi2/kpi1 + 1))) + (A*e)
/(d2n - F/((ks + 1/(1/kpi1 + 1/kpi2))*(kpi1/kpi2 + 1)))))^0.5000

f2 =
0.1592/(L*(cb + (A*e)/(d1n - F/k1) + (A*e)/(d2n - F/k2)))^0.5000

df2_dF =
-(0.0796*L*((A*e)/(k1*(d1n - F/k1)^2) + (A*e)/(k2*(d2n - F/k2)^2)))/(L*(cb + (A*e)/(
d1n - F/k1) + (A*e)/(d2n - F/k2)))^1.5000

A =
3.7500e-04
e =
2.8333e-11
d1n =
1.5000e-05
d2n =
2.3000e-05
ks =
6.0000e+09
kpi1 =
5.8000e+07
kpi2 =
8.8261e+07
L =
2.2000e-05
cb =
1.8300e-10

```